

**CLAY NANOTUBE COMPOSITES FOR ANTIBACTERIAL
NANOSTRUCTURED COATINGS**

by

Christen J. Boyer, B.S.

A Dissertation Presented in Partial Fulfillment
of the Requirements of the Degree
Doctor of Philosophy

COLLEGE OF APPLIED AND NATURAL SCIENCES
LOUISIANA TECH UNIVERSITY

May 2016

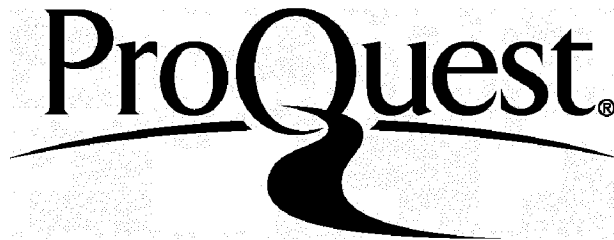
ProQuest Number: 10300720

All rights reserved

INFORMATION TO ALL USERS

The quality of this reproduction is dependent upon the quality of the copy submitted.

In the unlikely event that the author did not send a complete manuscript and there are missing pages, these will be noted. Also, if material had to be removed, a note will indicate the deletion.



ProQuest 10300720

Published by ProQuest LLC(2017). Copyright of the Dissertation is held by the Author.

All rights reserved.

This work is protected against unauthorized copying under Title 17, United States Code.
Microform Edition © ProQuest LLC.

ProQuest LLC
789 East Eisenhower Parkway
P.O. Box 1346
Ann Arbor, MI 48106-1346

LOUISIANA TECH UNIVERSITY

THE GRADUATE SCHOOL

February 19, 2016

Date

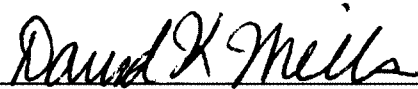
We hereby recommend that the dissertation prepared under our supervision by

Christen J. Boyer, B.S.

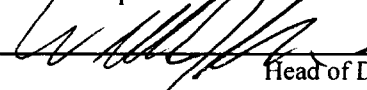
entitled **Clay Nanotube Composites For Antibacterial Nanostructured Coatings**

be accepted in partial fulfillment of the requirements for the Degree of

Doctor of Philosophy in Molecular Sciences and Nanotechnology



Supervisor of Dissertation Research

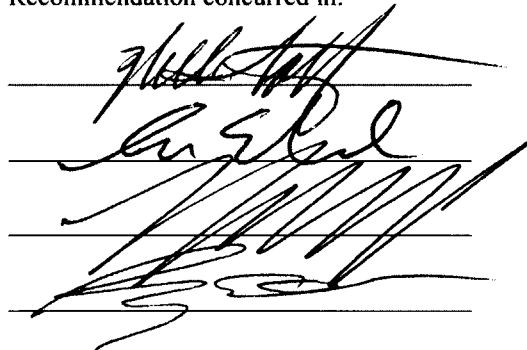


Head of Department

School of Biological Sciences

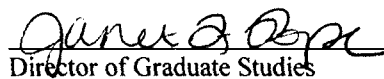
Department

Recommendation concurred in:

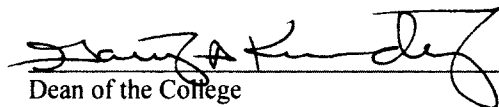


Advisory Committee

Approved:

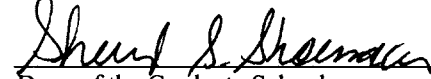


Director of Graduate Studies



Dean of the College

Approved:



Dean of the Graduate School

ABSTRACT

A surging demand for the development of new antimicrobial nanomaterials exists due to the frequency of medical device-associated infections and the transfer of pathogens from highly touched objects. Naturally occurring halloysite clay nanotubes (HNTs) have shown to be ideal particles for polymer reinforcement, time-release drug delivery, nano-reactor synthesis, and as substrate material for nanostructured coatings.

This research demonstrates the feasibility of a novel method for coating HNTs with metals for antibacterial applications. The first ever ability to coat HNTs through electrolysis was developed for customizable and multi-functional antibacterial nanoparticle platforms. HNTs were investigated as substrate for the deposition of copper (Cu) and silver (Ag) metal nanoparticles through electrochemical syntheses, and as a platform for nano-structured antibacterial polymer composites. Characterization of interfacial and material properties demonstrated the feasibility of electrolysis as a new efficient and replicable nano-scale surface modification route. Methods of encapsulating HNTs in nanofibers, three-dimensional printer filaments, and multifunctional polymer rubbers were also realized. The nanofabrication methods, nanoparticles, and polymer composites created in this work were novel, scalable, easy-to-replicate, and displayed antibacterial features with tunable properties.

APPROVAL FOR SCHOLARLY DISSEMINATION

The author grants to the Prescott Memorial Library of Louisiana Tech University the right to reproduce, by appropriate methods, upon request, any or all portions of this Dissertation. It is understood that "proper request" consists of the agreement, on the part of the requesting party, that said reproduction is for his personal use and that subsequent reproduction will not occur without written approval of the author of this Dissertation. Further, any portions of the Dissertation used in books, papers, and other works must be appropriately referenced to this Dissertation.

Finally, the author of this Dissertation reserves the right to publish freely, in the literature, at any time, any or all portions of this Dissertation.

Author Christin Boyer

Date May 21, 2016

DEDICATION

To my parents, Kenneth Boyer and Charlotte Doucet, grandparents, Henry Boyer, Rose Boyer, Gerald Doucet, and Rose Doucet.

TABLE OF CONTENTS

ABSTRACT.....	iii
DEDICATION.....	v
LIST OF TABLES.....	ix
LIST OF FIGURES	x
ACKNOWLEDGMENTS	xv
CHAPTER 1 INTRODUCTION	1
1.1 Goal.....	1
1.2 Rationale	1
1.3 Significance	3
1.4 Hypothesis	3
CHAPTER 2 BACKGROUND	5
2.1 Halloysite Nanotubes.....	5
2.1.1 Routes to a Metallized HNT.....	6
2.2 Antibacterial Metal Surfaces and Particles.....	7
2.3 Bacterial Biofilms.....	9
2.4 Layer-by-Layer Self-Assembly	11
2.5 Three Dimensional Printing.....	12
2.6 Nanofiber Production.....	12
CHAPTER 3 METHODS.....	14
3.1 Design and Objectives	14
3.2 Materials and Methods.....	14

3.2.1	<i>Instrumentation</i>	15
3.3	Methods	18
3.3.1	<i>Silver-HNT Synthesis</i>	18
3.3.2	<i>Copper-HNT Synthesis</i>	19
3.3.3	<i>Metal-HNT Drug Loading</i>	20
3.3.4	<i>Fabrication of Polymer-HNT Composites</i>	20
3.3.5	<i>Antibacterial Assays</i>	22
CHAPTER 4 RESULTS		24
4.1	Metal-HNT Characterization	24
4.1.1	<i>EDAX, SEM, and TEM</i>	25
4.1.2	<i>XRD and FTIR</i>	35
4.2	Metal-HNT Antibacterial Assays	39
4.3	Polymer-HNT Composites	51
4.3.1	<i>PLGA-HNT Nanofibers</i>	51
4.3.2	<i>ABS-HNT and PDMS-HNT</i>	55
4.3.3	<i>PDMS-HNT-PEO-N</i>	58
CHAPTER 5 DISCUSSION.....		62
5.1	Metal-HNT Electrolysis Fabrication	62
5.1.1	<i>Metal-HNTs as Antibacterial Agents</i>	64
5.2	Polymer Metal-HNT Nanocomposites	65
5.2.1	<i>ABS and PDMS Loaded with Metal-HNTs</i>	66
CHAPTER 6 CONCLUSIONS AND FUTURE WORK.....		68
6.1	Conclusions.....	68
6.2	Future Work.....	68
APPENDIX A EFFECT OF VOLTAGE ON CU-HNT PRODUCTION.....		70

A.1	Effect of Voltage on Cu-HNT Color and Morphology.....	71
APPENDIX B	PDMS-HNT-PEO SURFACE ANALYSES.....	73
B.1	SEM and Protein Adsorption Assays.....	74
APPENDIX C	CYTOCOMPATIBILITY OF HNT-NANOFIBERS	80
C.1	PLGA-HNT Cytocompatilby Assays	81
BIBLIOGRAPHY.....		88

LIST OF TABLES

Table 4-1: Table showing Mueller-Hinton Agar Zone of Inhibition Results for Commercial Catheters and PDMS-HNT.	60
Table 4-2: Table Showing Mueller-Hinton Broth Absorbance Results for Commercial Catheters and PDMS-HNT.	61

LIST OF FIGURES

Figure 3-1: FEI Tecnai G2 F30 TEM at Tulane University.....	16
Figure 3-2: HITACHI S 4800 FE-SEM/EDAX at Louisiana Tech University.	17
Figure 3-3: Bruker D8 XRD at Louisiana Tech University.	17
Figure 3-4: Genesys™ 20 Visible Spectrophotometer at Louisiana Tech University.	18
Figure 4-1: Image of the Ag-HNT Electrolysis Process.	25
Figure 4-2: Image of HNTs, A) HNT, B) Cu-HNT, and C) Ag-HNT.	25
Figure 4-3: EDAX of HNT.	26
Figure 4-4: EDAX of Ag-HNT.	27
Figure 4-5: EDAX of Scaled Ag-HNT.	27
Figure 4-6: EDAX of Cu-HNT.	28
Figure 4-7: EDAX of Scaled Cu-HNT.	28
Figure 4-8: SEM Image of HNT.	30
Figure 4-9: SEM Image of HNT.	30
Figure 4-10: TEM Image of HNT.	31
Figure 4-11: SEM Image of Ag-HNT.	31
Figure 4-12: SEM Image of Ag-HNT.	32
Figure 4-13: TEM Image of Ag-HNT.	32
Figure 4-14: TEM Image of Ag-HNT-N-S.	33
Figure 4-15: SEM Image of Cu-HNT.	33

Figure 4-16: SEM Image of Cu-HNT.	34
Figure 4-17: TEM Image of Cu-HNT.	34
Figure 4-18: TEM Image of Cu-HNT.	35
Figure 4-19: XRD Pattern of HNT.	36
Figure 4-20: XRD Pattern of Ag-HNT.	36
Figure 4-21: XRD Pattern of Ag-Oxide.	37
Figure 4-22: XRD Pattern of Cu-HNT.	37
Figure 4-23: FTIR Spectrum of HNT.	38
Figure 4-24: FTIR Spectrum of Ag-HNT.	38
Figure 4-25: FTIR Spectrum of Cu-HNT.	39
Figure 4-26: Effect of HNT on Absorbance of <i>S. aureus</i>.	40
Figure 4-27: Effect of HNT on Absorbance of <i>E. coli</i>.	40
Figure 4-28: Effect of Ag-HNT on Absorbance of <i>S. aureus</i>.	41
Figure 4-29: Effect of Ag-HNT on Absorbance of <i>E. coli</i>.	41
Figure 4-30: Effect of Cu-HNT on Absorbance of <i>S. aureus</i>.	42
Figure 4-31: Effect of Cu-HNT on Absorbance of <i>E. coli</i>.	42
Figure 4-32: Effect of Ag-HNT-N on Absorbance of <i>S. aureus</i>.	43
Figure 4-33: Effect of Ag-HNT-N on Absorbance of <i>E. coli</i>.	44
Figure 4-34: Effect of Cu-HNT-N on Absorbance of <i>S. aureus</i>.	44
Figure 4-35: Effect of Cu-HNT-N on Absorbance of <i>E. coli</i>.	45
Figure 4-36: Effect of Ag-HNT-N-S on Absorbance of <i>S. aureus</i>.	46
Figure 4-37: Effect of Ag-HNT-N-S on Absorbance of <i>E. coli</i>.	46
Figure 4-38: Effect of Cu-HNT-N-S on Absorbance of <i>S. aureus</i>.	47

Figure 4-39: Effect of Cu-HNT-N-S on Absorbance of <i>E. coli</i> .	47
Figure 4-40: Effect of Concentration of HNTs on Absorbance of <i>E. coli</i> . Sample: 1) Ag-HNT, 2) Ag-HNT-N, 3) Ag-HNT-N-S, 4) Cu-HNT, 5) Cu-HNT-N, 6) Cu-HNT-N-S, and 7) HNT.	48
Figure 4-41: Effect of Concentration of HNTs on Absorbance of <i>S. aureus</i> . Sample: 1) Ag-HNT, 2) Ag-HNT-N, 3) Ag-HNT-N-S, 4) Cu-HNT, 5) Cu-HNT-N, 6) Cu-HNT-N-S, and 7) HNT.	49
Figure 4-42: Effect of Concentration of HNTs on Absorbance of <i>E. coli</i> and <i>S. aureus</i> with Correlation and Exponential Comparison.	49
Figure 4-43: Effect of HNTs on <i>E. coli</i> in Agar Diffusion Assays. Sample: A) HNT, B) Ag-HNT, C) Cu-HNT, D) Nitrofurantoin Disc, E) Ag-Oxide, F) Ag- HNT-N-S.	50
Figure 4-44: SEM Images PLGA Nanofibers.	52
Figure 4-45: SEM Images of PLGA-HNT Nanofibers.	52
Figure 4-46: TEM Images of PLGA Nanofibers.	53
Figure 4-47: TEM Images of PLGA-HNT Nanofibers.	53
Figure 4-48: Effect of HNT-Nanofibers on Absorbance of <i>E. coli</i> . Sample: 1) Control <i>E. coli</i> , 2) PLGA, 3) PLGA-HNT, 4) PLGA-Ag-HNT, 5) PLGA-Cu- HNT, 6) PLGA-Ag-HNT-N, 7) PLGA-Cu-HNT-N, 8) PLGA-Ag-HNT- N-S, and 9) PLGA-Cu-HNT-N-S.	54
Figure 4-49: Effect of HNT-Nanofibers on Absorbance of <i>S. aureus</i> . Sample: 1) Control <i>S. aureus</i> , 2) PLGA, 3) PLGA-HNT, 4) PLGA-Ag-HNT, 5) PLGA-Cu-HNT, 6) PLGA-Ag-HNT-N, 7) PLGA-Cu-HNT-N, 8) PLGA-Ag- HNT-N-S, and 9) PLGA-Cu-HNT-N-S.	55
Figure 4-50: SEM Images of A) ABS, B) ABS, C) ABS-Ag-HNT, and D) ABS-Cu HNT.	56
Figure 4-51: Effect of HNT-Filaments on Absorbance of <i>S. aureus</i> . Sample: 1) Control <i>S. aureus</i> , 2) ABS, 3) ABS-HNT, 4) ABS-Ag-HNT, 5) ABS- Cu-HNT.	57
Figure 4-52: Effect of HNT-Filaments on Absorbance of <i>E. coli</i> . Sample: 1) Control <i>E. coli</i> , 2) ABS, 3) ABS-HNT, 4) ABS-Ag-HNT, 5) ABS-Cu-HNT.	57

Figure 4-53: Effect of PDMS-HNT Samples on Absorbance of <i>E. coli</i> . Sample: 1) Control <i>E. coli</i> , 2) PDMS, PDMS-HNT (3-7), PDMS-Ag-HNT (8-12), and PDMS-Cu-HNT (13-17).	58
Figure 4-54: Effect of PDMS-HNT Samples on Absorbance of <i>S. aureus</i> . Sample: 1) Control <i>S. aureus</i> , 2) PDMS, PDMS-HNT (3-7), PDMS-Ag-HNT (8-12), and PDMS-Cu-HNT (13-17).	58
Figure 4-55: Images of PDMS Samples in Agar Disc Diffusion Assays Against <i>E. coli</i> . A) Antibacterial Catheter, B) Silver Coated Catheter, C) PDMS-HNT-PEO-N, D) 100% PDMS Catheter, E) PDMS-HNT-PEO, and F) Nitrofurantoin Disc.	59
Figure 4-56: Images of PDMS Samples in Agar Disc Diffusion Assays Against <i>S. aureus</i> . A) Antibacterial Catheter, B) Silver Coated Catheter, C) PDMS-HNT-PEO-N, D) 100% PDMS Catheter, E) PDMS-HNT-PEO, and F) Nitrofurantoin Disc.	60
Figure A-1: Image of Cu-HNT Produced at Different Voltages. A) Control, B) 60 V, C) 120 V, and D) 240 V.	71
Figure A-2: XRD Pattern of Cu-HNT Produced at 60 V.	71
Figure A-3: XRD Pattern of Cu-HNT Produced at 120 V.	71
Figure A-4: TEM Image of Cu-HNT Produced at 60 V.	72
Figure A-5: TEM Image of Cu-HNT Produced at 120 V.	72
Figure B-1: SEM Images of PDMS Coated with Different Concentrations of PEO. A) PDMS, B) PDMS-PEO (1%), C) PDMS-PEO (2.5%), and D) PDMS-PEO (5%).	75
Figure B-2: SEM Images of PDMS-HNT-PEO Coated with Different Concentrations of PEO. A) PDMS-HNT, B) PDMS-HNT-PEO (1%), C) PDMS-HNT-PEO (2.5%), and D) PDMS-HNT-PEO (5%).	76
Figure B-3: Water Contact Angle Images of PDMS and PDMS-PEO. A) 103.3°, B) 97.7°, C) 8.2°, and D) 3.9°.	77
Figure B-4: Water Contact Angle Images of PDMS-HNT and PDMS-HNT-PEO. A) 103.8°, B) 90.8°, C) 15.8°, and D) 8.7°.	78
Figure B-5: Effect of PDMS-HNT-PEO on Absorbance of Fibrinogen (0-5% PEO). Sample: 1) PDMS, 2) PDMS-HNT, 3) PDMS-HNT-PEO (1%), 4) PDMS-HNT-PEO (2.5%), 5) PDMS-HNT-PEO (5%).	79

Figure C-1: Picrosirius Red Stain Assays with Mouse Embryonic Fibroblast Cells at Days 1-7 on PLGA Nanofibers.	84
Figure C-2: Picrosirius Red Stain Assays with Mouse Embryonic Fibroblast Cells at Days 1-7 on PLGA-HNT Nanofibers.	85
Figure C-3: Von Kossa Assays with Mouse Preosteoblast Cells at Days 1 and 3 on PLGA Nanofibers.	86
Figure C-4: Von Kossa Assays with Mouse Preosteoblast Cells at Days 1 and 3 on PLGA-HNT Nanofibers.	86
Figure C-5: Alcian Blue Stain Assays with Mouse Preosteoblast Cells at Day 1 on PLGA and PLGA-HNT Nanofibers.	87

ACKNOWLEDGMENTS

I would like to thank my advisor, Dr. David K. Mills, for his guidance and support of this research. Dr. Mills has been a role model during my time at Louisiana Tech University and has helped me develop as a researcher. I am thankful to the members of my dissertation committee, Dr. Sven Eklund, Dr. Jeffrey Shultz, Dr. Bryant Hollins, and Dr. William Wolf, for their useful suggestions. I would like to thank Davis Bailey, Dr. Alfred Gunasekaran, Dr. Sven Eklund, and Dr. Jibao He for their assistance with instrumentation. I would like to thank Dr. Sonali Karnik for helping with histological assays. Lastly, I would like to thank the Louisiana Space Consortium (LaSPACE) and the National Aeronautics and Space Administration (NASA) for funding a portion of this research.

CHAPTER 1

INTRODUCTION

1.1 Goal

The objective of this research was to develop novel hybrid nanoparticle composites and surface modification methods with a unified goal of advancing antibacterial surfaces by using HNTs as a platform. HNTs exist naturally around the world and can be mined from various mineral deposits, making it a very accessible nanomaterial (Lvov *et al.*, 2008). HNT-supported metal nanoparticles and HNT-polymer composites were invented and characterized by various material and surface analyses, and cell culture assays. Invented HNT-composite rubbers, nanofibers, and three dimensional (3D) printing substrates were explored as antibacterial nanostructured surfaces. The invented nanoparticles and composite combinations were used to measure the effects against Gram-negative and Gram-positive bacteria. The novel nanoparticles and nanocoatings were created to serve as multifunctional platforms for a range of antibacterial and biomedical applications.

1.2 Rationale

Nanotechnology concepts and nanoparticles are rapidly being integrated into consumer, medical, and industrial products to more precisely reduce biofilms and the spread of pathogens. HNTs have been shown to be an ideal component for fabricating

high performance polymer nanocomposites, and the clay nanotubes are currently economically viable and accessible (Abdullayev and Lvov, 2013; Guo *et al.*, 2009; Lvov *et al.*, 2008). Previous studies have shown HNTs to have a large surface area and can be loaded and coated with a variety of materials, such as drugs, polymers, and biomacromolecules for sustained and extended releases (Abdullayev and Lvov, 2013). The cytocompatibility properties of HNTs make them an ideal nanomaterial for new drug delivery systems (Mills, 2014; Vergaro *et al.*, 2010; Zhou *et al.*, 2010).

Fabricating uniform nanomaterials in high yield is a major goal in nanotechnology. The feasibility and realization of new high-throughput antibacterial nanomaterials and coatings depend on the antibacterial response and whether the nanofabrication methods are cost effective. Metals have been used as antimicrobials throughout history and are still effective against bacteria today (Abdullayev *et al.*, 2011; Yapijakis, 2009). Advancements in metallic nanoparticle synthesis have brought about a new age of antimicrobial technologies. Currently, there is nothing known about the electrolysis of metals in the presence of HNTs. The proposed electrochemical nano-assembly process acts as a new route for the deposition of metal nanoparticles on HNTs with antibacterial features. Existing HNT metallization fabrication methods rely on multi-step processes that include metal-salts or organic compounds, reducing agents, and high temperatures to achieve surface modifications (Abdullayev *et al.*, 2011; Chen *et al.*, 2012; Liu and Zhao, 2009; Rawtani and Agrawl, 2012; Tang *et al.*, 2013; Zhang *et al.*, 2013; Zhen *et al.*, 2011). Investigating the nanoparticle composites as antibacterial agents and in combination with commonly used medical polymers is an adequate response to the challenges of our time.

1.3 Significance

The realization of scalable and cost effective antibacterial nanocoating fabrication techniques may provide civilization with a new arsenal of antibacterial materials. The hybrid nanoparticle fabrication techniques created in this research and the invented HNT-polymer biomaterials provide a foundation for future nanotechnology researchers to explore.

A surging demand for the development of new antimicrobial materials exists across various industries. The frequency of medical device associated infections, the spread of pathogens through highly touched objects, and the new era of resistant bacteria are examples of current challenges in healthcare.

Pathogens can survive for months on dry surfaces and spread from many frequently touched surfaces (Kramer *et al.*, 2006). The spread of infectious diseases from highly touched objects remains a growing concern, and the number of medical device infections continues to be grand challenges in healthcare. In industrial environments, biofilms are a serious challenge to human health, quality control, and industrial productivity. Biofilms remain a constant and expensive problem for numerous industries and can affect water quality, contaminate products, enhance corrosion, and damage equipment over time (Parsek and Singh, 2003). Biofilms created by defective surfaces have been linked as the causative agent in a host of microbial infections (Breyers, 2008).

1.4 Hypothesis

It is hypothesized that electrolysis can be used to fabricate HNT-supported metal nanoparticles with predictable antibacterial features. It is hypothesized that as the concentration of Ag-HNT and Cu-HNT are increased in a fluid system, antibacterial

mechanisms occur and the concentration of bacteria is decreased. In addition, the multifunctional hybrid inorganic HNTs can be used to produce enhanced nanostructured polymer coatings for antibacterial and biomedical applications.

CHAPTER 2

BACKGROUND

2.1 Halloysite Nanotubes

HNTs exist naturally around the world and can be mined from various mineral deposits, making them a very accessible and cost effective nanomaterial (Lvov *et al.*, 2008). The clay nanotubes exist as a two-layered aluminosilicate with tubular features and are chemically identical to kaolin clay. HNTs typically display an inner diameter between 15–50 nanometers (nm.), and a length between 100–2000 nanometers. HNTs present a large surface area and can be loaded and coated with a variety of materials, such as drugs and biomacromolecules (Abdlayev and Lvov, 2013). A wide range of active agents, including antibiotics, cancer drugs, marine biocides, and biological molecules can be entrapped within the inner lumen, as well as within void spaces within the aluminosilicate mineral shells (Lvov *et al.*, 2016). HNTs have been shown to be non-cytotoxic on a variety of cell types including; chondrocytes, dermal fibroblasts, osteoblasts, and stem cells (Zhou *et al.*, 2010). Examination of HNTs with *in-vitro* assays showed that cells proliferated and maintained their cellular phenotype (Vergaro *et al.*, 2010). A recently completed biocompatibility study in a rat dermal model showed that HNTs do not provoke a cytotoxic response or a host immune response (Mills, 2014). As HNTs exhibit high levels of cytocompatibility, they represent ideal candidates for new

drug delivery, polymer additives, and as templates in nanotechnology (Abdullayev *et al.*, 2013).

2.1.1 Routes to a Metallized HNT

A number of methods exist for depositing metal nanoparticles on the outer surfaces and inner lumens of HNTs with each using a specific metal compound or salt with multi-step chemical reactions and high temperature calcination. Many HNT metallization efforts use HNTs as a metal catalyst support and for sensing systems. The advantages of using HNTs as a metal support system include nanometer scale tubular morphology, high surface area, availability, and low cost.

For example, palladium nanoparticle deposition was achieved through multi-step reactions with sodium tetrachloride palladate (Na_2PdCl_4), methanol, and poly(vinyl pyrrolidone) followed by heating (Zhang *et al.*, 2013). HNT-supported cobalt was achieved through calcination of HNTs and cobalt nitrite under temperatures as high as 349 °C (Chen *et al.*, 2012). Deposition of Ag onto nanotubes has included in situ reduction of Ag-nitrite through the polyol process (Liu and Zhao, 2009). Similarly, HNT-supported gold was explored through reacting gold-chloride and ammonia solutions followed by heating to 300 °C (Zhen *et al.*, 2011). Additionally, iron and nickel can be deposited on HNTs through mixing metal-compounds and calcination with high temperatures (Tang *et al.*, 2013).

Biomedical applications of Ag-loaded HNTs have included DNA sensors (Rawtani *et al.*, 2013). The Ag nanoparticles on the HNTs were created by reducing Ag-nitrate in solution. The Ag-HNT particles were able to interact with single and double-stranded oligonucleotides. Ag nanorod synthesis in the inner lumen of HNTs was

achieved by vacuum loading Ag-acetate followed by high temperature calcination (Abdullayev *et al.*, 2011). The study validated the nanoparticles as antibacterial additives for commercial paints. The paint composites were shown to be effective against bacteria and the HNTs strengthened the material properties. Overall, metal-HNTs have demonstrated multifunctional properties and are viewed to be an important material for future technologies.

2.2 Antibacterial Metal Surfaces and Particles

Metals have been used as antimicrobials since the time of Hippocrates (Yapijakis, 2009) and continue to show effectiveness today (Lemire *et al.*, 2013). During the first part of the 20th century until the introduction of synthetic antibiotics, electric colloids of Ag were commonly used for antimicrobial therapy (Alexander, 2009). Ag and Cu particle technologies are commonly seen in health related applications, from wound dressings to disinfecting sprays (Piozzi, 2015). Metal nanoparticles, such as Cu and Ag, have shown to be extremely toxic to bacteria at very low concentrations, and it is theorized that transition metals disrupt respiration and electron transport systems upon absorption into bacterial cells (Lemire *et al.*, 2013). Transition metals have been incorporated into inert polymer materials for the prevention of infections. Recent trends in industry show an increase in use of Ag as antimicrobial agents for textiles. Many methods have produced platforms for high performance textiles, antimicrobial polymers and washes (Windler *et al.*, 2013).

The recent developments in metal nanoparticle synthesis and characterizations have led to various new areas of science and technology (Anselmann, 2001; Mazzola, 2003). Metal nanoparticle synthesis approaches include laser ablation (Lee *et al.*, 2001),

gamma irradiation (Long *et al.*, 2007), electron irradiation (Bogle *et al.*, 2006), various chemical reductions (Bonnemann and Richards, 2001), photochemical methods (Mallick *et al.*, 2004), microwave processing (Yin *et al.*, 2004), thermal decompositions (Navaladian *et al.*, 2007), and electrochemical synthesis techniques (Reetz and Helbig, 1994).

Cu nanoparticles are redox-active essential metals that can be easily oxidized during interaction with bacteria cell membranes. Cu nanoparticles can act as catalytic cofactors generating or catalyzing reactive oxygen species (ROS) (Shleeva *et al.*, 2005). Cu-induced toxicity is theorized to occur by several mechanisms, which include the formation of ROS by free Cu ions, where cupric and cuprous ions can participate in redox reactions (Gaetke and Chow, 2003). Studies show that Cu^{2+} can be reduced to Cu^+ in the presence of reducing agents, catalyzing the formation of hydroxyl radicals from hydrogen peroxide (Bremner, 1988). The extremely reactive hydroxyl radicals further react and can be detrimental to cellular molecules and processes, such as protein oxidation.

Ag nanoparticles anchor to the bacterial cell wall, penetrate, and cause structural damage that eventually leads to cell death (Gianluigi *et al.*, 2015; Prabhu and Poulouse, 2012; Franci *et al.*, 2015). As seen with most metals, the main toxic mechanism of Ag nanoparticles is the release of Ag ions (Feng *et al.*, 2008). It is suggested that Ag nanoparticles may also generate free radicals in the presence of bacteria, when examined under electron spin resonance spectroscopy (Danilcauk *et al.*, 2009). The free radicals make the cell membrane porous and lead to cell death (Kim *et al.*, 2007). In a recent study, Ag nanoparticles increased membrane permeability of Gram-negative bacteria, and also restored antibiotic susceptibility to a resistant strain. Within *in-vitro* and *in-vivo*

models of urinary tract infection, Ag induces oxidative stress and potentiates antibiotic activity (Ramirez *et al.*, 2013). The research by Ramirez's group showed that Ag could be used to enhance existing antibiotics, thus strengthening the antibacterial arsenal for infectious diseases.

2.3 Bacterial Biofilms

A biofilm is a multicellular community of microbes that forms on a solid surface or at a liquid-air interface (Stoodley *et al.*, 2002). In a biofilm, microbes are densely packed within a self-assembled extracellular matrix that provides protection for resident bacteria from various environmental agents (Bryers, 2008; Niklas *et al.*, 2003; Stewart and Costerton, 2001). Biofilm formation occurs in several stages, which include attachment, development, maturation, and disassembly (Vlamakis *et al.*, 2013). Biofilms remain a constant and expensive problem for healthcare and industry. Biofilms can affect water quality, contaminate products, enhance corrosion, and damage equipment over time (Parsek and Singh, 2003). In industrial environments, biofilms are a serious challenge to human health, quality control, and industrial productivity. Pathogens can spread from many frequently touched surfaces (Kramer *et al.*, 2006). Biofilms created by defective surfaces have been linked as the causative agent in a multitude of microbial infections (Breyers, 2008).

Hospital acquired infections (HAI) are commonly associated with implantable medical devices or surgical procedures. In intensive care units (ICUs), Gram-negative bacteria account for about 70% of hospital-acquired infections (Gaynes *et al.*, 2005). The most common biomaterial-associated HAI is catheter-associated urinary tract infections (CAUTI) and infections are predominately caused by Gram-negative bacteria (Behzadi *et*

al., 2010). Surface adsorption of serum proteins initiates bacterial adhesion and proliferation on the implant surface leading to biofilm formation on devices.

A number of attempts were made to prevent biofilm formation on surfaces, including antimicrobial anti-fouling coatings on titanium implants and other medical devices (Zhao *et al.*, 2009). Various biomaterials have been developed as drug-releasing device coatings and include polyurethanes, poly(vinyl alcohol), poly(acrylic acid), polyamide, poly(vinyl pyrrolidone), polylactides, polyanhydrides, and poly(dimethylsiloxane) (Vasiliev *et al.*, 2009). There has been a considerable research effort aimed at preventing post-surgical infections after implantation of permanent devices and from minimally invasive devices. A common approach to prevent biofilm is to coat the surface with bactericidal or bacteriostatic substances. The antibacterial properties of antibiotics are well documented in the scientific literature, as well as the uses in implantable devices (Hickok and Shapiro, 2012).

Many commonly used medical implants, especially those in urinary catheters, promote biofilm formation and are responsible for infections. Catheter associated urinary tract infection (CAUTI) is one of the most common hospital acquired infections worldwide, which causes serious economic burdens for patients and hospitals (Behzadi *et al.*, 2010). The majority of commercial catheters and implantable materials offer no surface protection against bacteria and biofilm formation. This has become a major public health crisis and a major economic burden on healthcare. CAUTI rates increased since 2009 and the estimated total cost in the USA ranges from \$340 million - \$450 million annually (Meddings *et al.*, 2013). There are over 30 million urinary catheter insertions a year in the United States in hospital settings, and the World Health

Organization (WHO) estimates that over 200 million people are suffering from bladder control problems that require urinary catheterization.

2.4 Layer-by-Layer Self-Assembly

Layer-by-layer (LBL) nanofabrication is based on the sequential adsorption of oppositely charged polyelectrolytes and materials with intermediate wash steps. The self-assembly process occurs spontaneously and structural formations occur from disordered systems. Nano-assembly through a layer-by-layer technique was first proposed in 1966 (Iller, 1966), and was later pioneered during the 1990's by Gero Decher (Decher, *et al.*, 1991; Decher, 1997) and Yuri Lvov (Lvov *et al.*, 1995). The LBL method is cheap, versatile, easy to replicate and can be used with a wide variety of polyelectrolytes and nanoparticles.

There are a variety of biocompatible and biodegradable materials that can be used in LBL multilayers. The LBL processes are reversible and interact by non-covalent intermolecular forces. This process is often referred to as supramolecular chemistry and is widely used in thin film fabrication methods. Common polycation and polyanion materials used in the LBL process include polystyrene sulphonate, polyethylene imine, poly(vinyl pyrrolidone), poly(acrylic acid), dextran sulfate, and sodium alginate. Recent progress has shown LBL microcapsules to be an important new tool for drug delivery applications (Ariga *et al.*, 2011). Studies have shown that encapsulation of polyelectrolyte microcapsules are capable of delivering drugs through a potential hydrogen (pH) responsive release (Kumar *et al.*, 2009). LBL can be used to encapsulate a variety of biomaterials and nanomaterials, including HNTs for extended and sustained release of drugs and bioactive agents (Veerabadran *et al.*, 2009).

2.5 Three Dimensional Printing

Three-dimensional (3D) printing through hot melt extrusion is an emerging field that may replace many conventional biomaterial-manufacturing approaches, where customizable implants and localized drug delivery is more feasible (Mamidwar *et al.*, 2012). Typically in 3D plastic printing, material is extruded from a heated nozzle in a layer-by-layer fashion and the layers form a 3D structure. The positioning is controlled with an x, y, z -axis system (Kesner and Howe, 2011) and can be used to create custom medical devices with tailored formulations. Medical applications for 3D printing are expanding rapidly and have gained much interest for pharmaceutical applications. Antibiotic drugs and other agents are effective when coupled with 3D printing technologies and the combination is creating a new era of custom antibacterial medical devices (Sandler *et al.*, 2014; Weisman *et al.*, 2015).

2.6 Nanofiber Production

Nanofiber mats and scaffolds have a wide range of biomedical applications including bone repair and regeneration, drug delivery, wound dressings, regenerative medicine, and tissue engineering (Kolakovic *et al.*, 1997; Vasita and Katti, 2006). Nanofibers are typically generated by the method of electrospinning. During the electrospinning process, surface tension holds a polymer solution at the tip of the needle (Shin *et al.*, 2001), and a high voltage electric field is applied in the needle tip; charge is induced in the polymer solution. The polymer jet is initiated when the charge repulsion within the solution overcomes the surface tension. When the polymer jet travels, the solvent evaporates and the polymer fibers are deposited on the collector plate. The jet from the needle forms a cone-like pathway known as the Taylor cone (Zuo *et al.*, 2005).

Generating fibers and films through solution blow spinning is a high-throughput alternative technique requiring a very simple set-up: a concentrated polymer solution in a volatile solvent, and an airbrush fitted to a high-pressure gas source. Previous studies have described its ease of use, and rapid deposition rate as compared to electrospinning (Behrens *et al.*, 2014). This technique has been studied for a range of applications including drug delivery, microfiltration, and tissue engineering (Tutak *et al.*, 2013). The solution blow-spin method allows for direct deposition of nanofiber meshes and scaffolds onto a variety of geometries. The concept allows for on-demand fabrication of conformal nanofiber mats and allows for precise and site-specific construction. The approach may potentially be used as surgical sealant in place of or in addition to sutures in applications such as vascular, intestinal, or airway anastomosis. Solution blow spinning could also be useful in areas requiring the use of a hemostatic material or sealant, especially when large areas are exposed and conventional suturing may not be possible.

CHAPTER 3

METHODS

3.1 Design and Objectives

This research examined HNTs as a platform for antibacterial nanostructured coatings. HNTs were used as substrate material for antibacterial agents and also explored as composite additives for plastic and elastic biomaterials. Electrolysis techniques were explored as novel methods for depositing metal nanoparticles onto HNT surfaces. HNT-particles were validated through various instruments including scanning electron microscopy (SEM), energy-dispersive X-ray spectroscopy (EDAX), X-ray powder diffraction (XRD), Fourier transform infrared spectroscopy (FTIR) and transmission electron microscopy (TEM). The antibacterial activity of metal-HNTs and drug-loaded derivatives were monitored against Gram-negative and Gram-positive bacteria with a spectrophotometer. Plastic and elastomeric polymers infused with HNTs were examined through various surface characterization methods, material analysis, and *in-vitro* assays. The following sections give a more in depth breakdown of the objectives and methods.

3.2 Materials and Methods

Halloysite nanoclay, *Escherichia coli* (*E. coli*) ATCC® 11775™ 1000 CFU, *Staphylococcus aureus* (*S. aureus*) ATCC® 6538™ 50 CFU, chloroform (HPLC grade), absolute ethanol, acetone (HPLC grade), poly(D,L-lactide-co-glycolide) (PLGA, 50:50,

molecular weight ~30,000-60,000), poly(vinyl pyrrolidone) (PVP, molecular weight ~1,300,000), poly(acrylic acid) solution (PAA, molecular weight ~250,000, 35 wt.% in H₂O), acetone (HPLC grade), LB powder growth medium, nitrofurantoin crystalline (N), hydrochloric acid, Alcian blue stain, and bovine fibrinogen ($\geq 70\%$ protein basis) were purchased from Sigma-Aldrich (St. Louis, MO). Silver rods (99.99% pure, 304 mm. x 3.3 mm.) and copper rods (99.95% pure, 304 mm. x 3.3 mm.) were purchased from Amazon.com LLC (Seattle, WA). Picrosirius red stain and Von Kossa stain kit were purchased from PolySciences (Warrington, PA). Poly(dimethylsiloxane ethylene oxide), methyl terminated (molecular weight ~ 600) was acquired from Polysciences Inc. (Warrington, PA). Liquid implant grade silicone rubber was purchased from Applied Silicone Corporation (Santa Paula, CA). Translucent silicone rubber (PDMS) was purchased from AeroMarine Products (San Diego, CA). Antibacterial intermittent catheters and silver coated Foley catheter were purchased from commercial antibacterial catheter suppliers. Nitrofurantoin susceptibility test discs (100 mm.) were purchased from Becton Dickenson and Company (Franklin Lakes, NJ). Micro BCA protein assay kit, Mueller-Hinton agar plates, and Mueller-Hinton liquid broth were purchased from Thermo Fisher Scientific (Waltham, MA). A Master Airbrush G22 with 0.2 mm. needle was purchased from TCP Global (San Diego, CA) and 3-(trihydroxysilyl) propyldimethyloctadecyl ammonium chloride (S) was purchased from Gelest Inc. (Morrisville, PA).

3.2.1 Instrumentation

A FEI Tecnai G2 F30 twin transmission electron microscope (Hillsboro, OR) was used to study the nanoparticle structures (located at Tulane University in New Orleans, LA)

(**Figure 3-1**). The particles were stabilized on carbon support film mounted on 200 mesh Cu gilder TEM grids. All other instruments used were located at Louisiana Tech University (Ruston, LA). A HITACHI S-4800 field-emission scanning electron microscope (Tokyo, Japan) (**Figure 3-2**) was used to characterize the HNTs and polymer surfaces, and the energy dispersive X-ray spectroscopic analysis feature was used for evaluation of chemical elements on HNT surfaces. The HNTs were mounted to carbon conductive adhesive tapes for SEM viewing and elemental analysis. A D8 X-ray diffractometer by Bruker (Billerica, MA) was used to study the HNT diffraction patterns (**Figure 3-3**). A Genesys™ 20 Visible Spectrophotometer by Thermo Fisher Scientific (Waltham, MA) was used to monitor bacteria absorbance values (**Figure 3-4**). A Fourier transform infrared spectroscope Nicolet IR100 and a NanoDrop 2000c by Thermo Fisher Scientific (Waltham, MA) were used to monitor HNT samples.

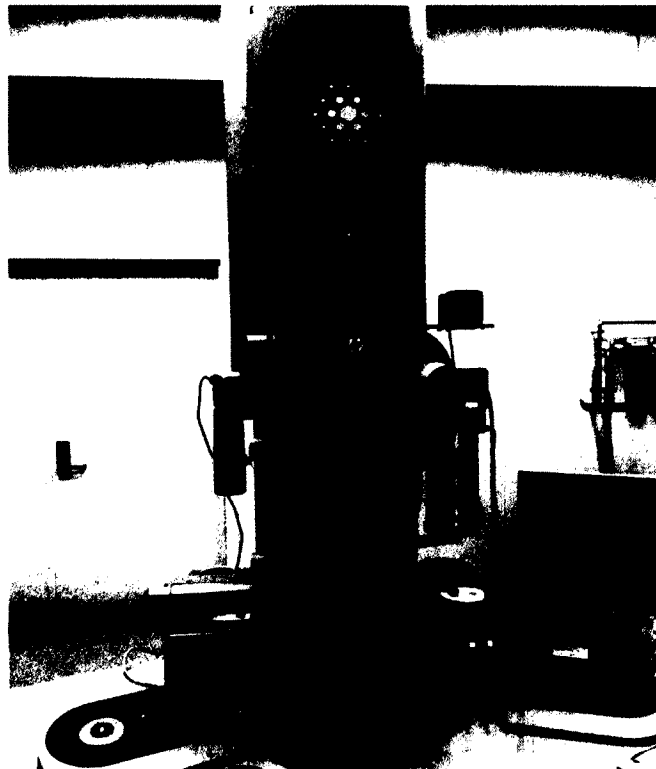


Figure 3-1: FEI Tecnai G2 F30 TEM at Tulane University.

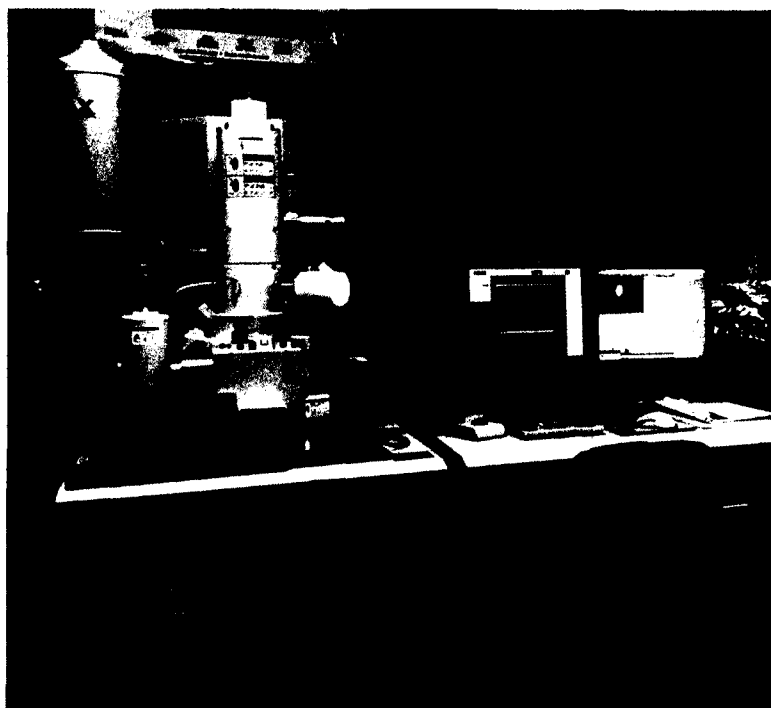


Figure 3-2: HITACHI S 4800 FE-SEM/EDAX at Louisiana Tech University.

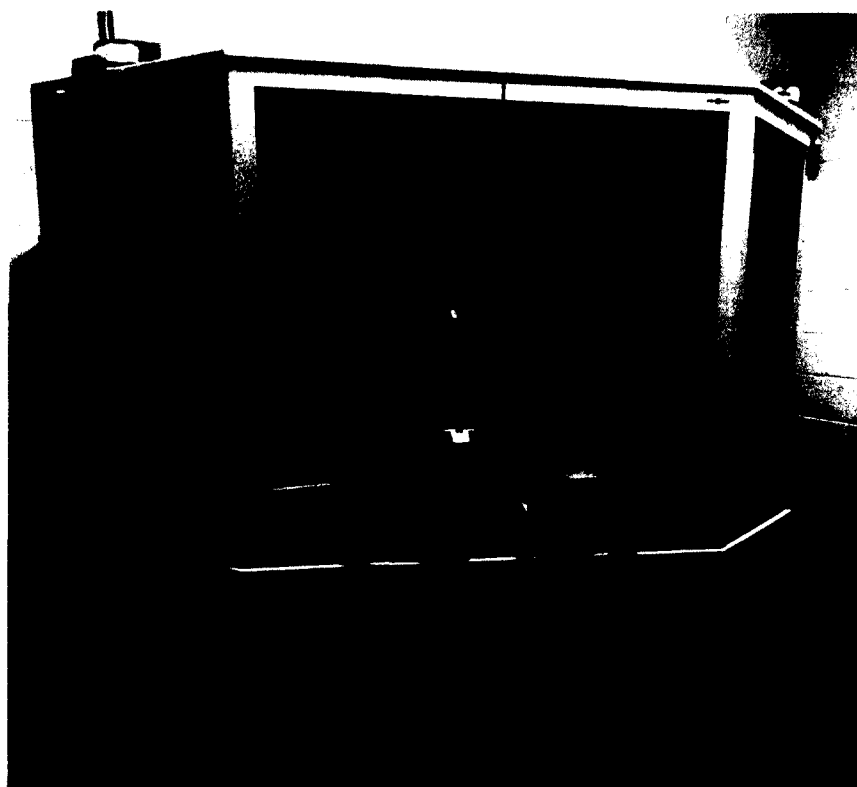


Figure 3-3: Bruker D8 XRD at Louisiana Tech University.

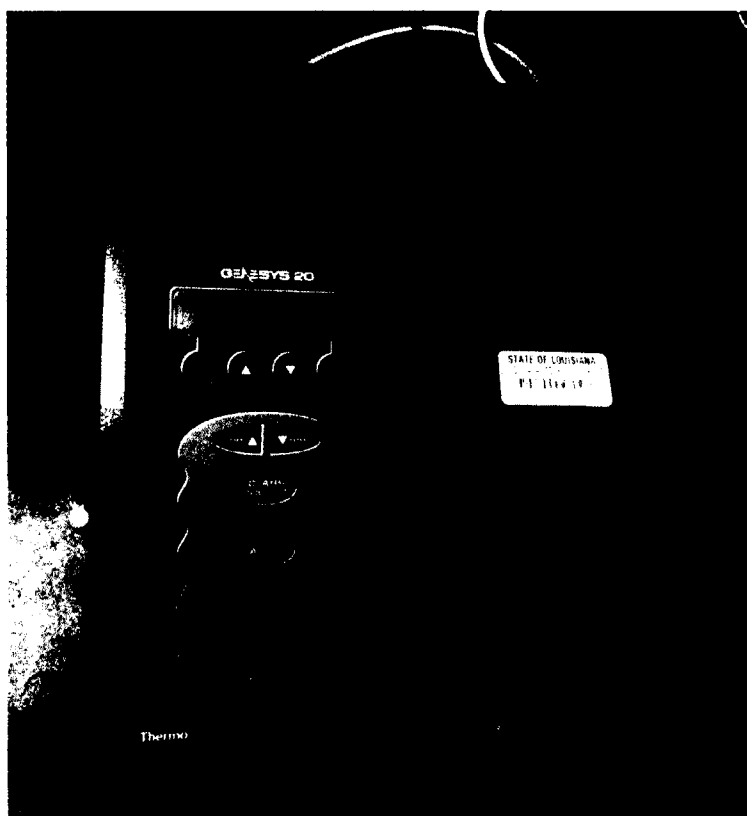


Figure 3-4: Genesys™ 20 Visible Spectrophotometer at Louisiana Tech University.

3.3 Methods

Electrolysis of pure Ag and Cu was explored as a route to modify the surface of HNTs for antibacterial applications. In distilled water, HNTs were mixed and a constant direct current was applied to metal electrodes to synthesize metal nanoparticles and facilitate metal nanoparticle deposition on HNT surfaces. The following sections give a more in depth breakdown of the electrochemical syntheses.

3.3.1 Silver-HNT Synthesis

Ag electrodes were placed in 500 milliliters (ml.) of distilled water and the distance between electrodes was 0.5 inches (in.). The mixture was heated to 95 °Celsius (C) and connected to a direct current (D/C) power supply. Next, 300 milligrams (mg.) of HNTs was added and continuously mixed with a magnetic stirrer. Next, direct current

was applied and kept constant at 30 volts (V) for 40 minutes. After 40 minutes, the power supply was disconnected and the mixture was centrifuged. The supernatant was decanted and the final Ag-HNT product was dried at 60 °C for 24 hours (hr.) for SEM and EDAX.

To examine scalability, Ag electrodes were placed in 1,000 ml. of distilled water and heated to 95 °C. The distance between electrodes was 0.5 in. and 5 grams (g.) of HNTs was added and continuously mixed with a magnetic stirrer. D/C voltage was applied and was kept constant at 30 V for 2 hours. After 2 hr. the D/C power supply was disconnected, the solution was centrifuged and decanted. The Ag-HNT product was dried at 60 °C for 24 hr. and stored for material characterization and antibacterial assays.

3.3.2 Copper-HNT Synthesis

Cu electrodes were placed in 500 ml. of distilled water and the distance between electrodes was 0.5 inches. The solution was heated to 95 °C and connected to a D/C power supply. Next, 300 mg. of HNTs were added and continuously mixed to create a suspension. Next, D/C voltage was applied and was kept constant at 240 V for 40 minutes. After 40 minutes the power supply was disconnected and the mixture was centrifuged and decanted. The Cu-HNT product was dried at 60 °C for SEM and EDAX.

To examine scalability, Cu electrodes were placed in 1,000 ml. of distilled water and heated to 95 °C. The distance between electrodes was 0.5 in. and 5 g. of HNTs was added and continuously mixed with a magnetic stirrer. Next, D/C voltage was applied and kept constant at 240 V for 2 hr. The power supply was disconnected after 2 hr. and the mixture was centrifuged and decanted. The Cu-HNT product was dried at 60 °C for 24 hr. and stored for material characterization and antibacterial assays. It is important to note that all antibacterial assays were examined with the scaled synthesis products.

3.3.3 Metal-HNT Drug Loading

Ag-HNT and Cu-HNT powders were explored as platforms for delivering multiple antibacterial agents in combination. Nitrofurantoin (N) (25 mg.) was mixed with 5 ml. of acetone. The dissolved nitrofurantoin mixture was next added to 45 ml. of water and was used to load Ag-HNT and Cu-HNT (1 ml./25 mg.) for 24 hr. under a vacuum (28 pounds per square inch). Next, the powders were air-dried for 24 hr. for antibacterial assays. The drug loaded HNTs are referred to as Ag-HNT-N and Cu-HNT-N.

Ag-HNT-N and Cu-HNT-N samples were nanocoated with polyelectrolytes and silane-quaternary ammonium salt (S). PVP powder was mixed with distilled water (1 mg./ml.) and PAA solution was mixed with distilled water (3 ml./100 ml.). Each polyelectrolyte mixture was adjusted to pH 3 by adding hydrochloric acid. PVP (1 ml.) and PAA (1 ml.) coatings, with wash steps in between, were repeated to form three bilayers on Cu-HNT (25 mg.) and Ag-HNT (25 mg.) surfaces. Lastly, the samples were immersed in 3-(trihydroxysilyl) propyldimethyloctadecyl ammonium chloride (S) (6% in distilled water) for five minutes and air dried for 24 hr. for antibacterial assays. The LBL coated HNTs are referred to as Ag-HNT-N-S and Cu-HNT-N-S.

3.3.4 Fabrication of Polymer-HNT Composites

Fabrication of HNT-loaded nanofibers used solution blow-spinning methods. PLGA was dissolved in acetone at 10% weight/weight (wt./wt.). HNT, Ag-HNT, Ag-HNT-N, Ag-HNT-N-S, Cu-HNT, Cu-HNT-N, and Cu-HNT-N-S powders were added to PLGA-acetone mixtures to form 1% wt./wt. HNT mixtures. The mixtures were placed in a sonication water bath for 20 minutes and then 1 ml. of each was pipetted into a separate commercial airbrush system reservoir. The air pressure for each run was set to 30 pounds

per square inch and the mixtures were sprayed onto wax paper with a 5 cm. spray distance. The PLGA products were air dried for antibacterial assays. Each fibrous mat had final dry weight of 10% wt./wt. HNTs. For SEM viewing, square silicon wafers (1x1 mm.) were sprayed with PLGA and PLGA-HNT at 5 cm. distances.

Fabrication of HNT-loaded filaments used direct bulk additive manufacturing and hot-melt extrusion. ABS plastic pellets were mixed with HNT, Ag-HNT, and Cu-HNT dry powders (5% wt./wt.), and blends were extruded at 230 °C to form filaments for SEM and antibacterial assays.

Fabrication of the PDMS-HNT nanocomposites used direct bulk modification methods. Translucent PDMS was thoroughly mixed with HNT, Ag-HNT, and Cu-HNT powders (0 - 10% wt./wt.) and with curing agent (10:1 wt./wt.). The uncured PDMS-HNT composites were poured into flat polystyrene petri dishes and stored in a refrigerator at 8 °C for 24 hr. to remove trapped air. The samples were then cured in an oven at 60 °C for 24 hr. and were cut into circular discs (0.60 mm diameter and 0.2 mm thickness) using a sterile hole punch for antibacterial assays.

Similarly to the metal-HNT loaded PDMS fabrication, a PEO-antibiotic version was fabricated and used bulk modification. Implant grade silicone samples were thoroughly mixed with HNTs (0 and 10% wt./wt.) and with curing agent (10:1 wt./wt.). The uncured PDMS-HNT composites were poured into flat polystyrene petri dishes and stored in a refrigerator at 8 °C for 24 hr. to remove trapped air. The samples were then cured in an oven at 60 °C for 24 hr. and were cut into circular discs (0.60 mm diameter and 0.2 mm thickness) using a sterile hole punch. A PDMS hydrophilic surface modification method was adapted from the established surface modification method

(Dhruv, 2009) and applied to PDMS-HNT substrates. The samples were submerged in chloroform for 24 hr. to remove residual cross-linker and unreacted monomers, then dried in an oven for 24 hr. at 60 °C. Next, the samples were placed in chloroform solutions for 24 hr. with amphiphilic block copolymer PDMS-PEO (PEO) (0%-5% wt./wt.). Samples were dried in an oven at 60 °C for 24 hr. and then thoroughly rinsed with ethanol and air dried. The treated PDMS-HNT-PEO composites were then placed in nitrofurantoin-acetone (5.1 mg./ml.) for 24 hr. and air-dried. The fabricated rubber composite is referred to as PDMS-HNT-PEO-N.

3.3.5 Antibacterial Assays

E. coli and *S. aureus* vitroids were used to create 0.5 McFarland standard bacterial suspensions. Fifty microliters ($\mu\text{l.}$) of standard bacterial suspensions were added to Mueller-Hinton broths and standard Mueller-Hinton agar plates for incubation with samples. Mueller-Hinton broth (5 ml.) assays were tested against different HNT concentrations (0-24 mg.). Each were added to broths and compared in triplicates after 24 hr. of incubation at 37 °C. Additional control broths with and without bacterial suspensions and with HNTs were monitored in triplicates. Bacterial optical densities (OD) of the broth cultures were monitored with a visible spectrophotometer at wavelength (λ) 600 nanometers (nm.) for *E. coli* and *S. aureus*. For qualitative analysis, 12 mg. of HNT, Ag-HNT, Cu-HNT, Ag-oxide, and Ag-HNT-N-S powders were added to Mueller-Hinton agar plates and incubated at 37 °C for 24 hours.

For antibacterial assays with HNT-loaded polymers, *E. coli* and *S. aureus* vitroids were used to create 0.5 McFarland standard bacterial suspensions. Mueller-Hinton broths (5 ml.) were used to validate the antibacterial properties of PDMS-HNT discs, PLGA-

HNT mats, and ABS-HNT filaments. PDMS-HNT-PEO-N were validated by agar disc diffusion and broth assays. Samples of each set were compared in triplicates after 24 hr. of incubation at 37 °C. Bacterial zones of inhibition (ZOI) were monitored with a digital caliper. The optical densities (OD) of the broths were monitored with a visible spectrophotometer at $\lambda=600$ nm. for *E. coli* and *S. aureus*.

CHAPTER 4

RESULTS

4.1 Metal-HNT Characterization

The feasibility of using electrolysis as a HNT surface modification platform for antibacterial applications was confirmed in a series of experiments designed to characterize material properties, interface, and antibacterial activity. Validation of the hybrid nanotubes included SEM, TEM, EDAX, XRD, and FTIR. The characterization techniques demonstrated metallic nanoparticles could be deposited on HNT surfaces through electrolysis.

The naturally occurring white appearance of the HNT powder was altered to a variety of colors depending upon the type of metal used during electrolysis processing. During the electrolysis of Ag, the mixtures appeared to change color. The final Ag-HNT dry product was colored gray, which indicated that the HNTs underwent a chemical change or adsorption of Ag particulate (**Figure 4-1** and **Figure 4-2: A and C**). The electrolysis of Cu with HNTs produced a final product with brown coloration (**Figure 4-2: B**). The electrolysis syntheses were repeated five times and the color changes were replicable. It was concluded by visual inspection that the nanotubes underwent surface modification during the electrolysis processing.

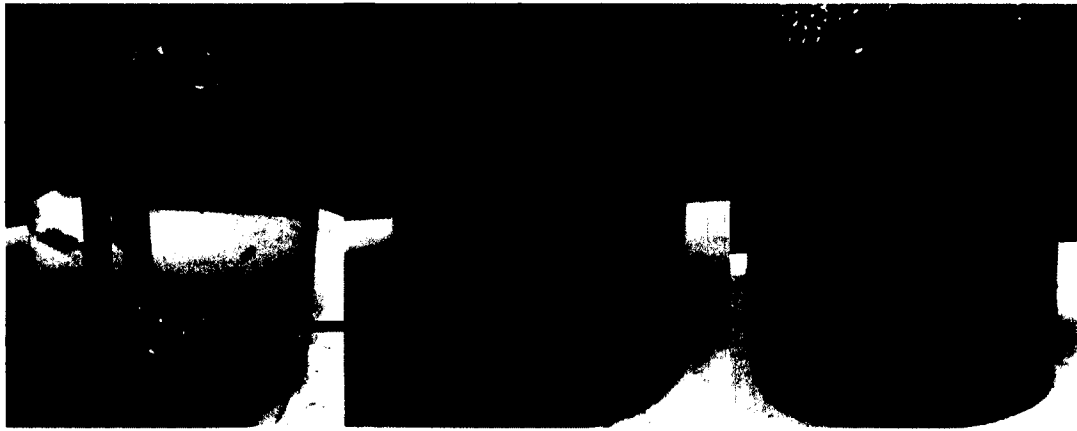


Figure 4-1: Image of the Ag-HNT Electrolysis Process.

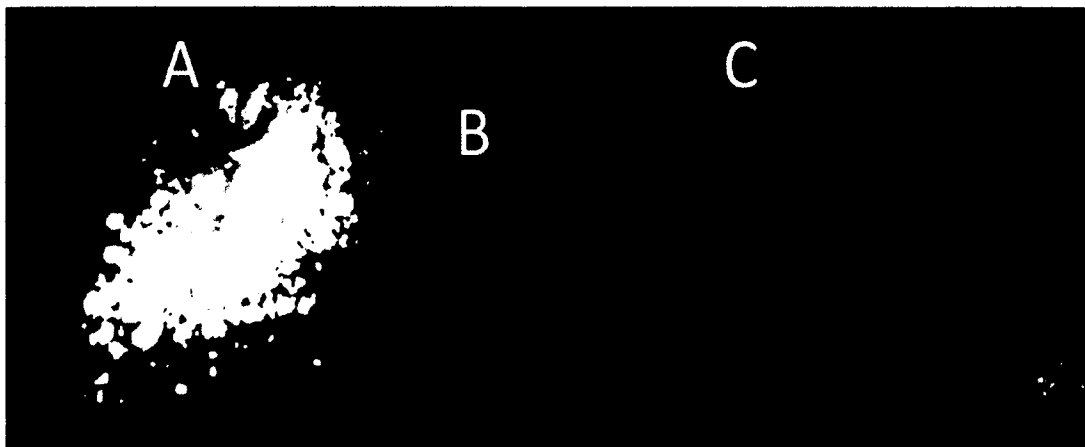


Figure 4-2: Image of HNTs, A) HNT, B) Cu-HNT, and C) Ag-HNT.

4.1.1 EDAX, SEM, and TEM

EDAX was used to further explore the HNT surfaces and it appeared that the HNT tubular structures underwent a metallic surface modification. It is important to note that the presence of carbon in measurements was due to the conductive carbon adhesive tape and should be ignored in all EDAX readings. EDAX of HNTs are well documented and the weight % ratios of alumina to silica display similar percentages to previous studies (Fernandez *et al.*, 2014). EDAX readings of the pure HNTs showed a similar elemental weight percentage ratio of alumina (21.48 %) and silica (20.45 %)(**Figure 4-3**).

EDAX of the first Ag-HNT synthesis route showed a 26% elemental weight percentage of Ag on the surface (Figure 4-4). EDAX of the scaled Ag-HNT synthesis route also showed the presence of Ag, with 10.17% Ag elemental weight on the surface (Figure 4-5). EDAX of the first Cu-HNT synthesis route showed 9.99% Cu elemental weight on the surface (Figure 4-6) and the scaled Cu-HNT synthesis (Figure 4-7) displayed 6.89% Cu elemental weight on the surface. EDAX further validated the assumptions and it was concluded that metallic particulates were present in the various nanotube samples.

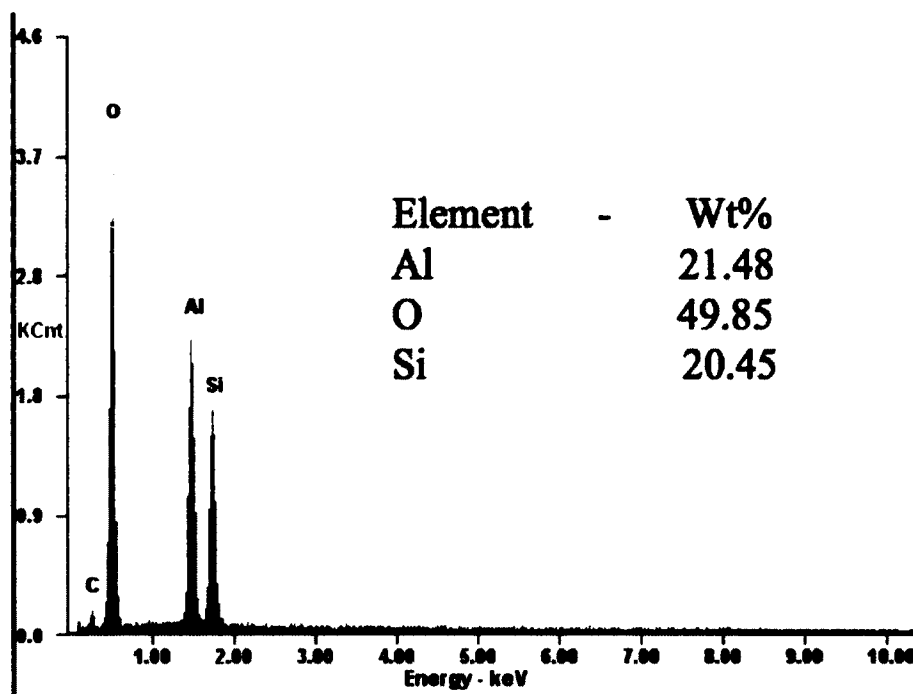


Figure 4-3: EDAX of HNT.

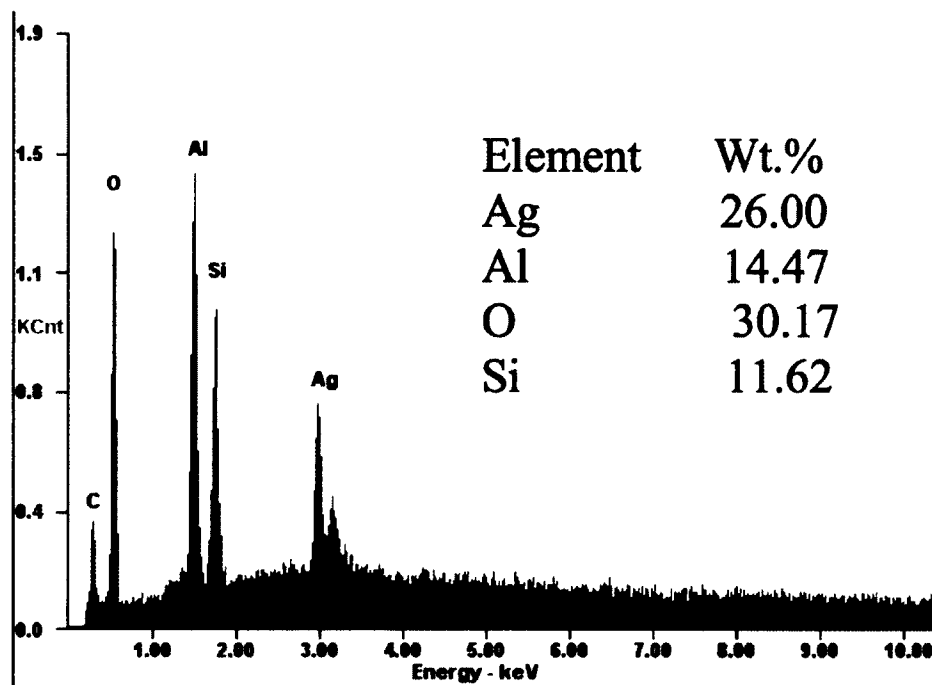


Figure 4-4: EDAX of Ag-HNT.

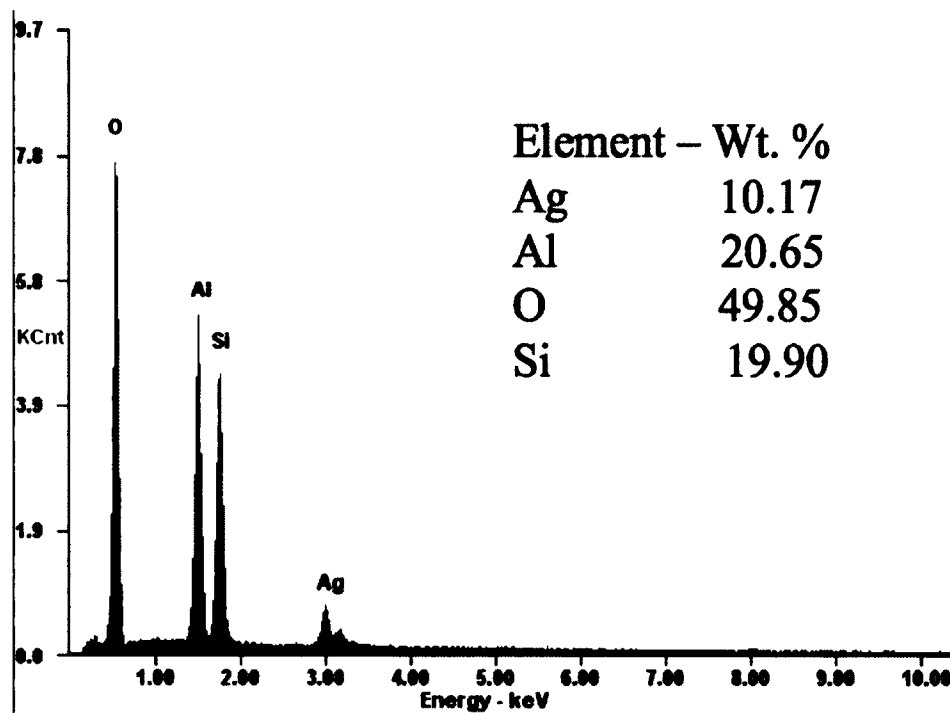


Figure 4-5: EDAX of Scaled Ag-HNT.

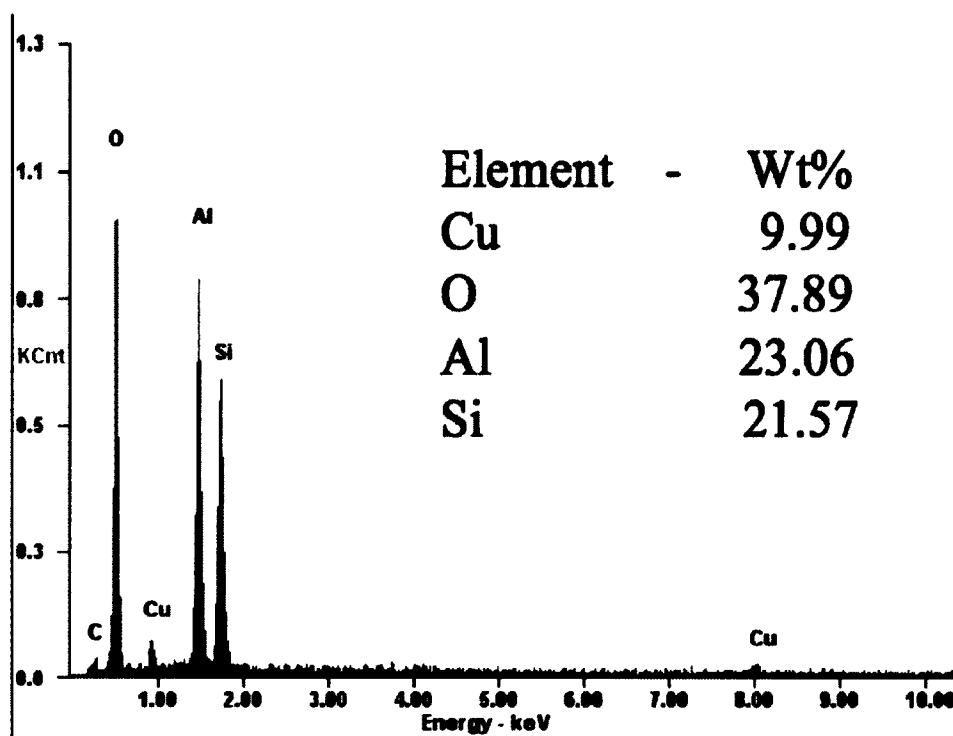


Figure 4-6: EDAX of Cu-HNT.

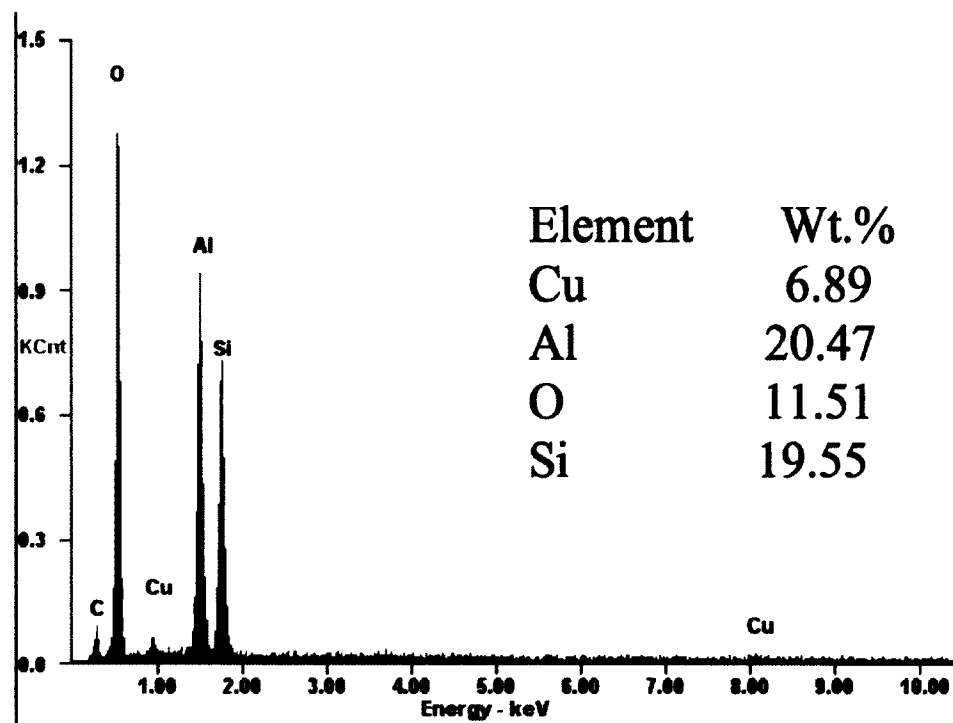


Figure 4-7: EDAX of Scaled Cu-HNT.

The Ag-HNT and Cu-HNT products were examined under SEM and TEM to validate the deposition of metal particles on the surface. The electron micrographs further validated the assumption that the electrolysis method was capable of producing metallic nanocoatings on the surfaces of HNTs.

The pure HNT powder showed typical tubular features when viewed under SEM and TEM (**Figure 4-8**, **Figure 4-9**, and **Figure 4-10**). Typical tubular features were also detected for the Ag-HNT powder (**Figure 4-11**). Spherical Ag nanoparticles and clusters were clearly visible on the Ag-HNT surfaces in SEM and TEM images (**Figure 4-12** and **Figure 4-13**). Ag-HNT particles that underwent drug loading and LBL nanocoatings also displayed Ag nanoparticles on the surfaces (**Figure 4-14**). All Ag nanoparticles detected in TEM images displayed diameters under 100 nanometers.

SEM images of the Cu-HNT showed HNT typical tubular structures (**Figure 4-15** and **Figure 4-16**). Cu nanoparticles and clusters were visible on the surfaces of HNTs in TEM images (**Figure 4-17** and **Figure 4-18**). The metal Cu-HNT displayed different morphologies compared to Au-HNT. The Cu-HNT displayed Cu clusters on the surface of HNTs. As evidenced by electron micrographs, it was confirmed that metallic nanoparticles were successfully deposited on HNTs through the electrochemical syntheses.

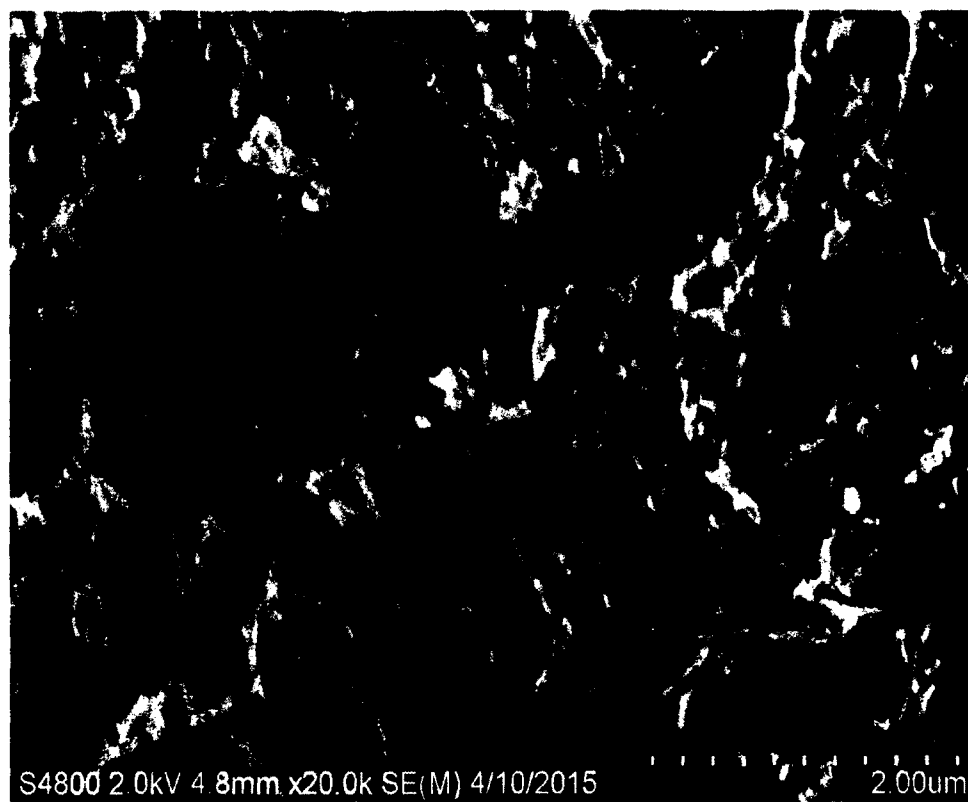


Figure 4-8: SEM Image of HNT.



Figure 4-9: SEM Image of HNT.

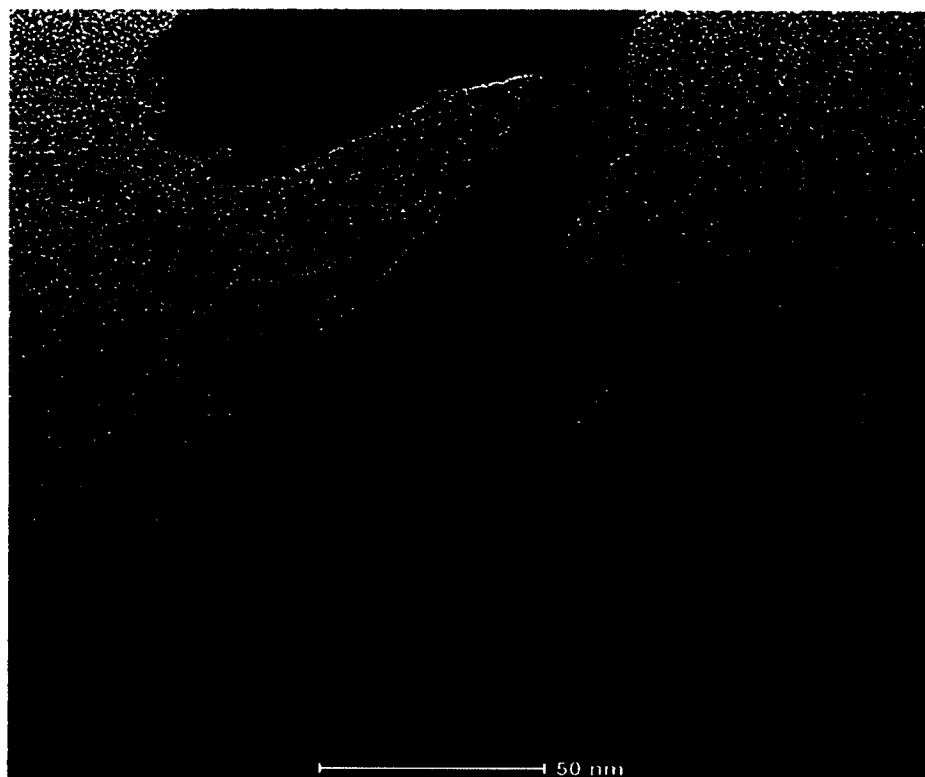


Figure 4-10: TEM Image of HNT.

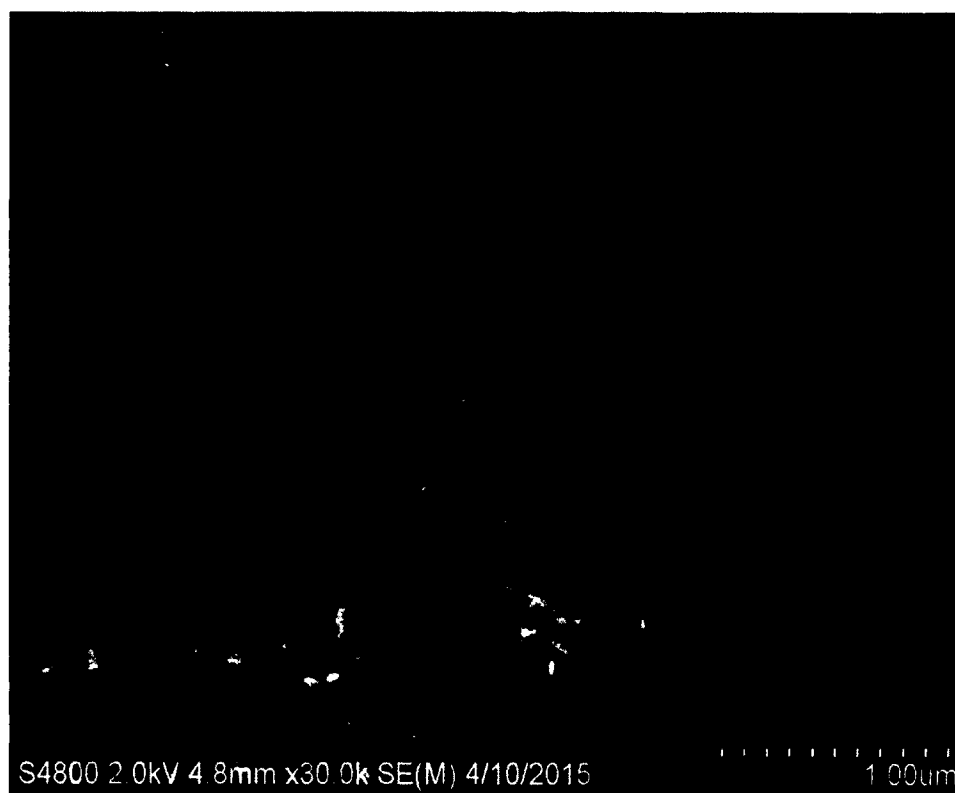


Figure 4-11: SEM Image of Ag-HNT.

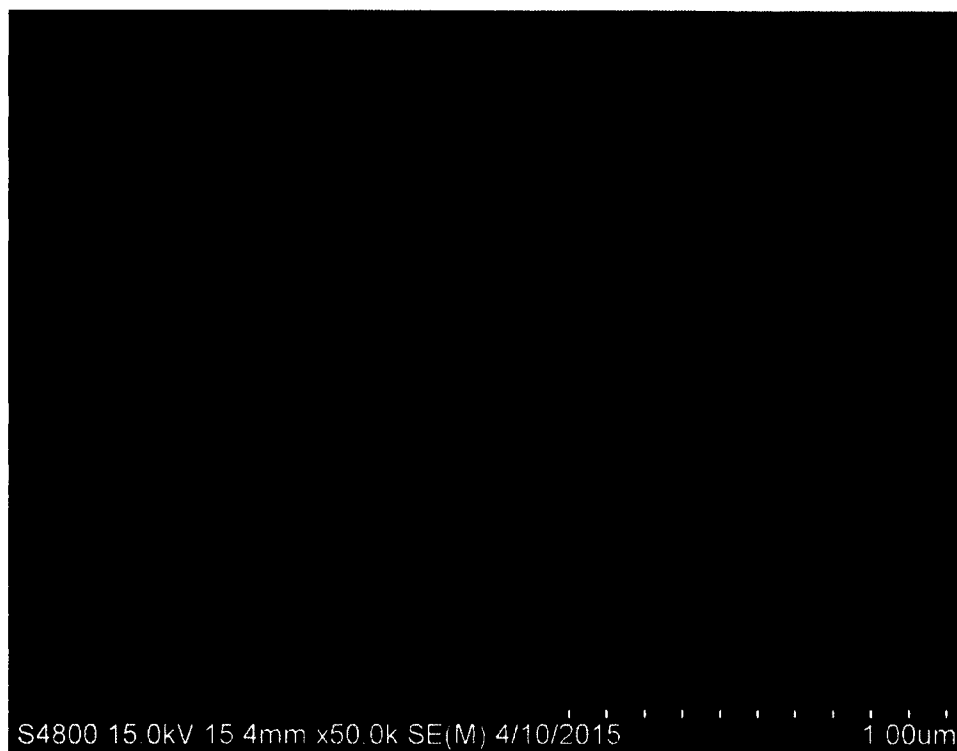


Figure 4-12: SEM Image of Ag-HNT.

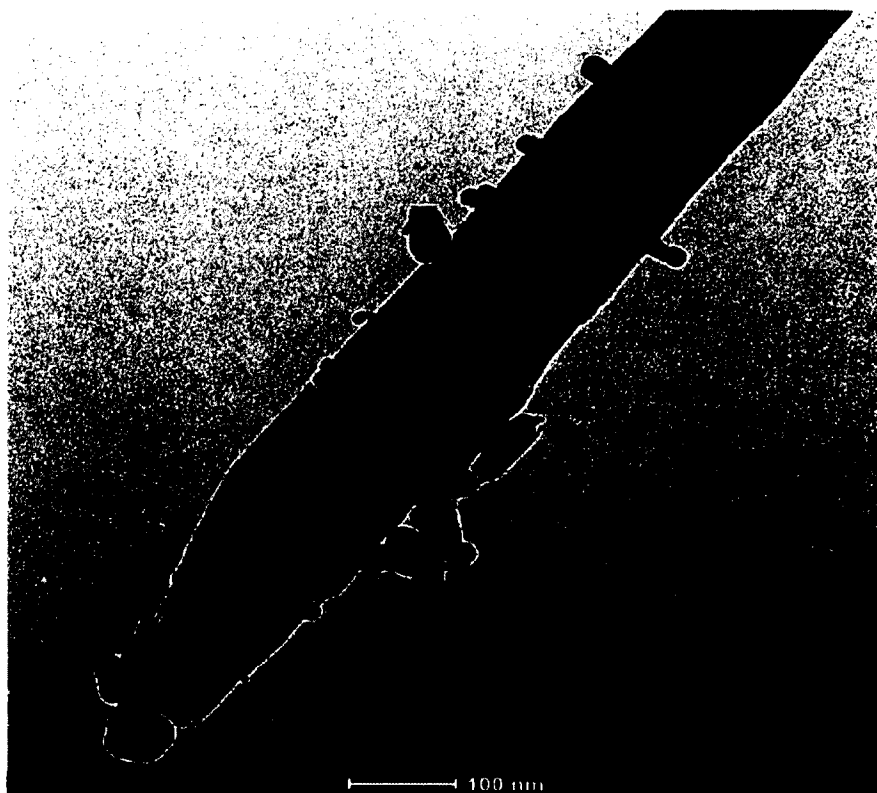


Figure 4-13: TEM Image of Ag-HNT.

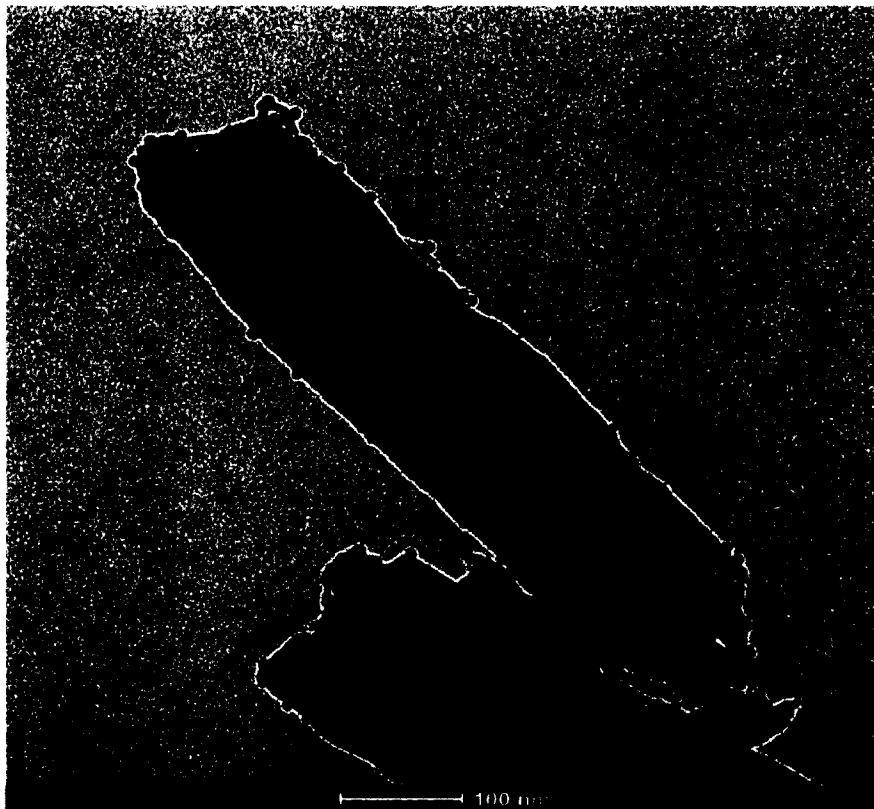


Figure 4-14: TEM Image of Ag-HNT-N-S.

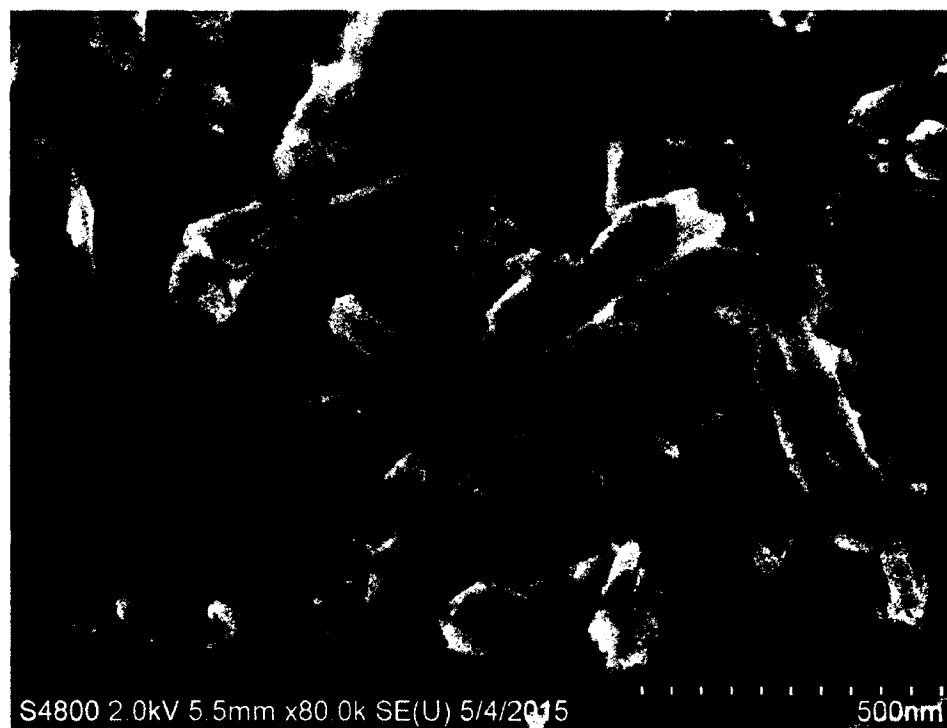


Figure 4-15: SEM Image of Cu-HNT.

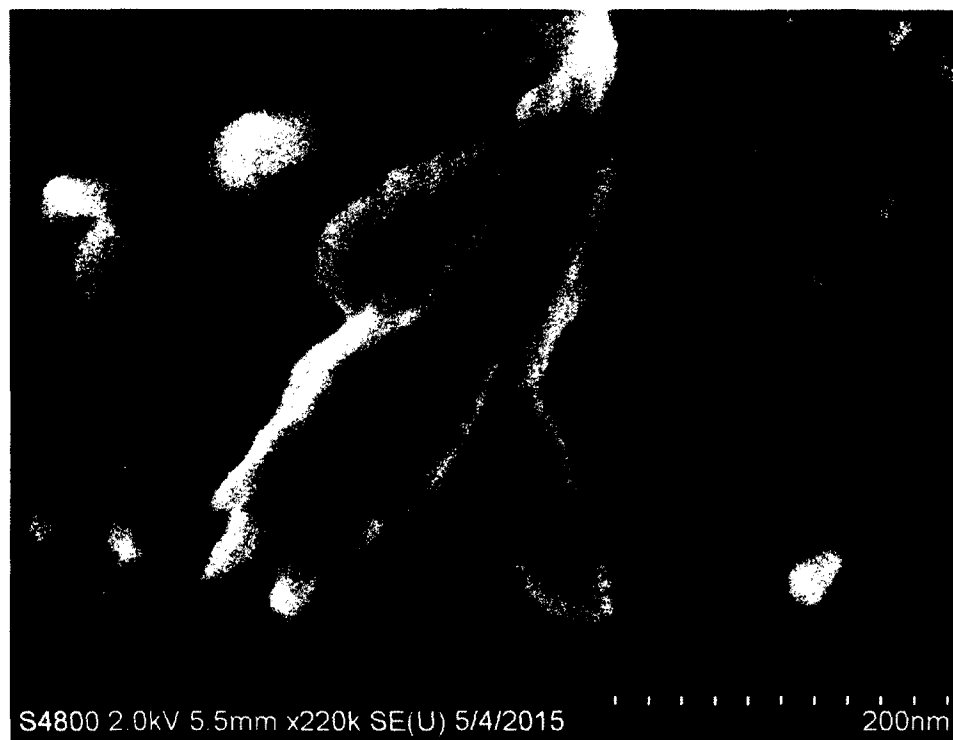


Figure 4-16: SEM Image of Cu-HNT.

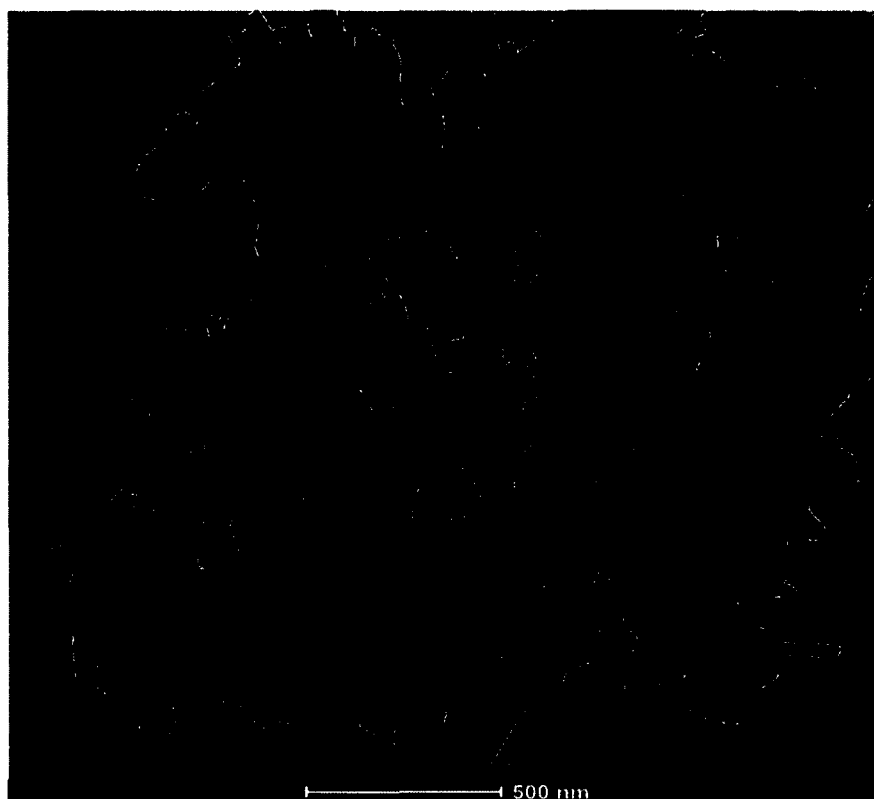


Figure 4-17: TEM Image of Cu-HNT.

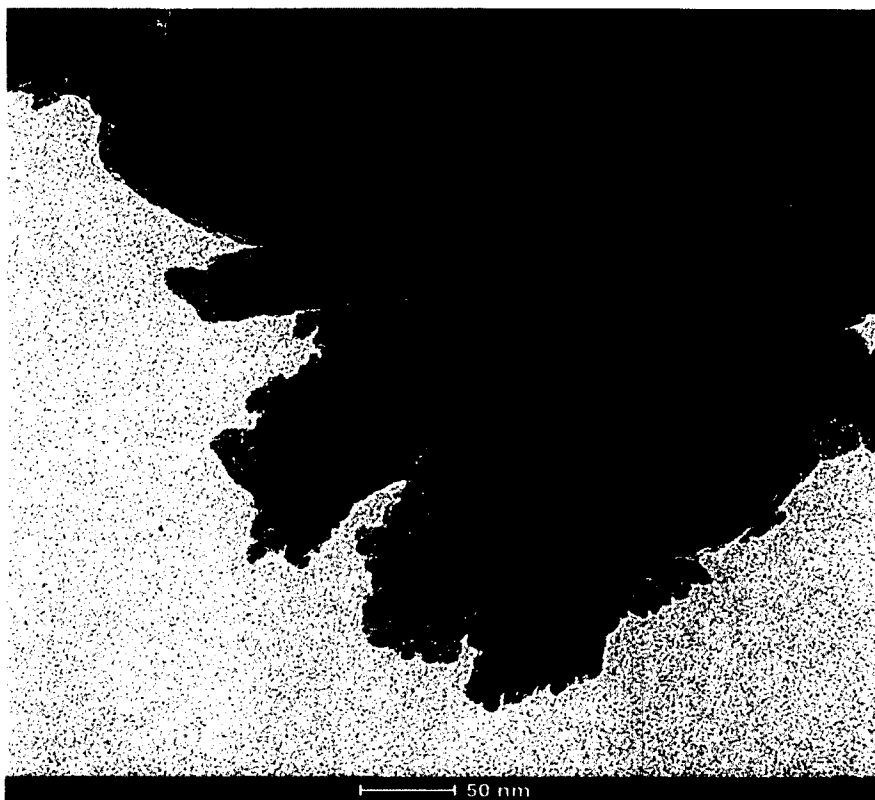


Figure 4-18: TEM Image of Cu-HNT.

4.1.2 XRD and FTIR

XRD was used as a tool for analyzing the HNT and metal-HNT crystal structures. Various factors like Bragg factor, crystallographic factor, and profile factor determined the sharpness of peaks and number of noise peaks seen in the XRD patterns. The calculated pattern of pure HNT powder displayed a maximum peak at $20 (2\theta)$ with an intensity of more than 4500 A.U., which indicated the maximum crystallinity (**Figure 4-19**). No impurity was found in the HNT samples, which indicated a single-phase sample. Calculated XRD patterns of HNTs are well documented and these results showed similar patterns when compared to previous HNT XRD patterns (Fernandez *et al.*, 2014; Zhang *et al.*, 2013). The XRD pattern of Ag-HNT showed peaks at $20 (2\theta)$ and at $38 (2\theta)$ (Ag), and the pattern indicated that the crystallinity of HNTs was not disturbed (**Figure 4-20**).

Ag-oxide was used as a control and showed a similar Ag peak at 38 (2θ) (Figure 4-21). The XRD pattern of Cu-HNT powder showed a broader peak at 20 (2θ) as compared to HNT and Ag-HNT powders. A peak was also observed at 35 (2θ) for the Cu samples, which indicated the crystallinity of Cu (Figure 4-22). Cu XRD patterns are well documented and these results showed similar patterns (Venkata *et al.*, 2015). The Cu-HNT XRD pattern indicated that no chemical reaction occurred and the crystallinity of HNTs was not disturbed during the Cu electrolysis processing.

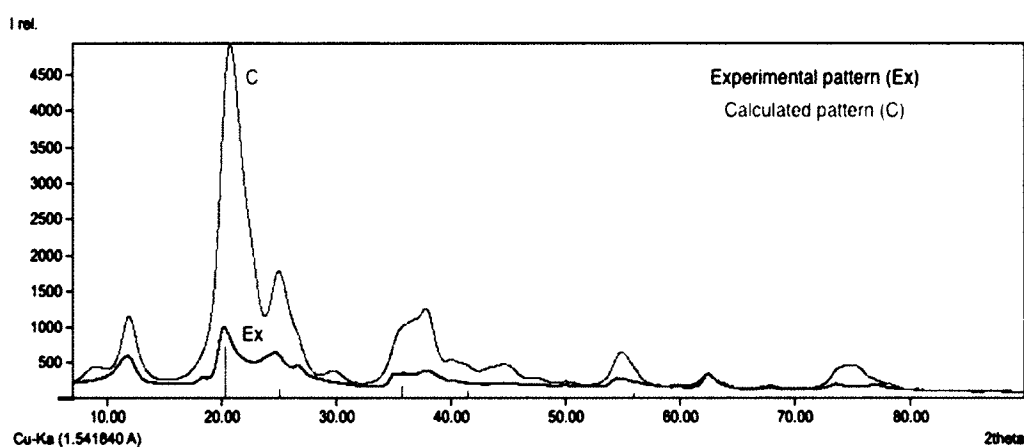


Figure 4-19: XRD Pattern of HNT.

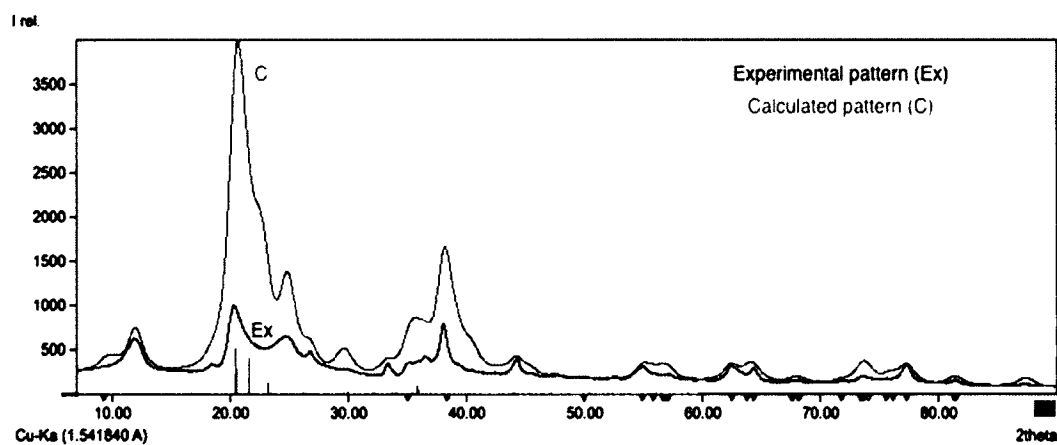


Figure 4-20: XRD Pattern of Ag-HNT.

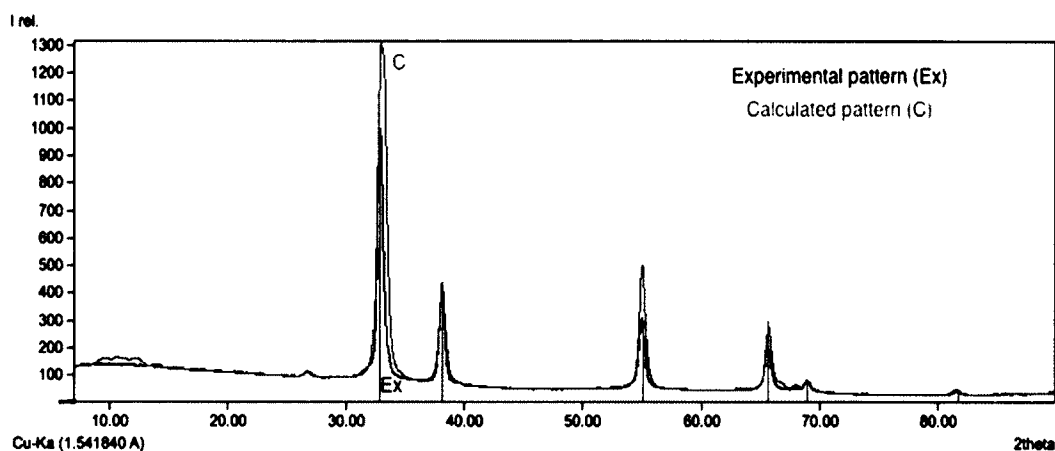


Figure 4-21: XRD Pattern of Ag-Oxide.

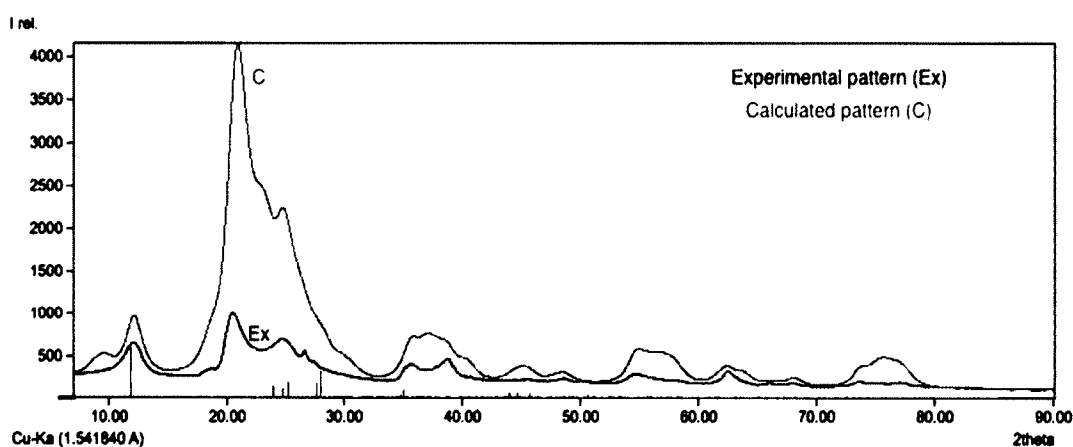


Figure 4-22: XRD Pattern of Cu-HNT.

FTIR was used to examine the adsorption bands of HNTs and the metallized versions. The general stretching absorption bands for kaolin clays are well established (Fernandez *et al.*, 2014; Zhang *et al.*, 2013) and were detected by Interpret IR+ software analysis. The software demonstrated the similarities between kaolin clay and experimental samples. The HNTs displayed band patterns consistent with kaolin clay highlighted patterns (**Figure 4-23**). For the Ag-HNT, similar bands were detected and were consistent with kaolin clay highlighted bands (**Figure 4-24**). Cu-HNT also displayed similar bands when compared to standard kaolin bands (**Figure 4-25**).

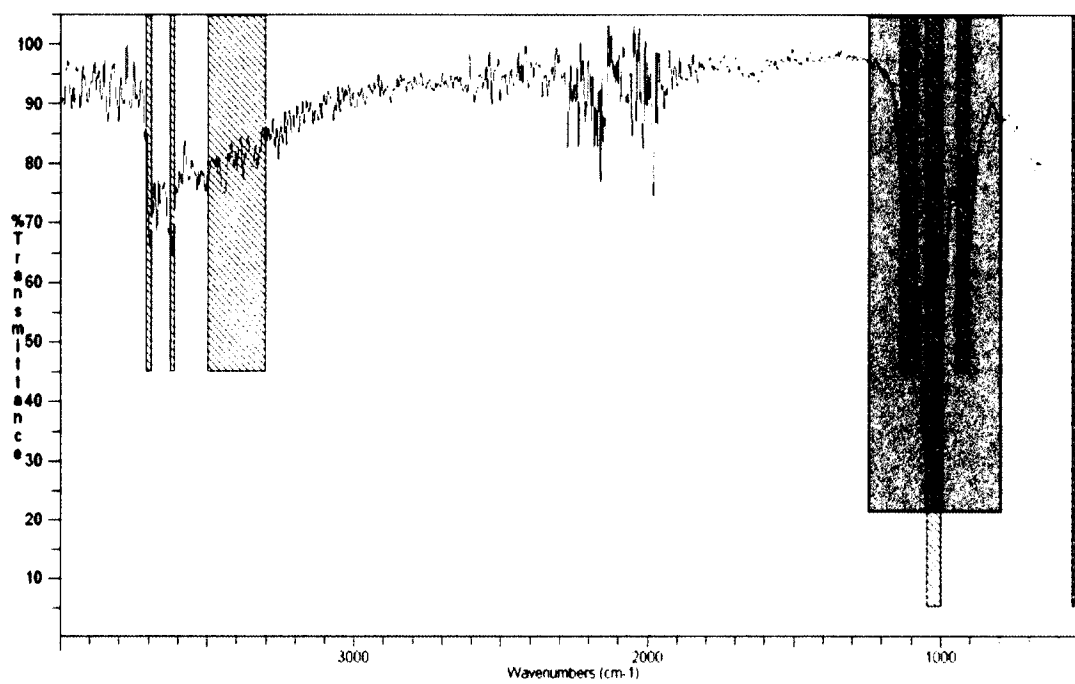


Figure 4-23: FTIR Spectrum of HNT.

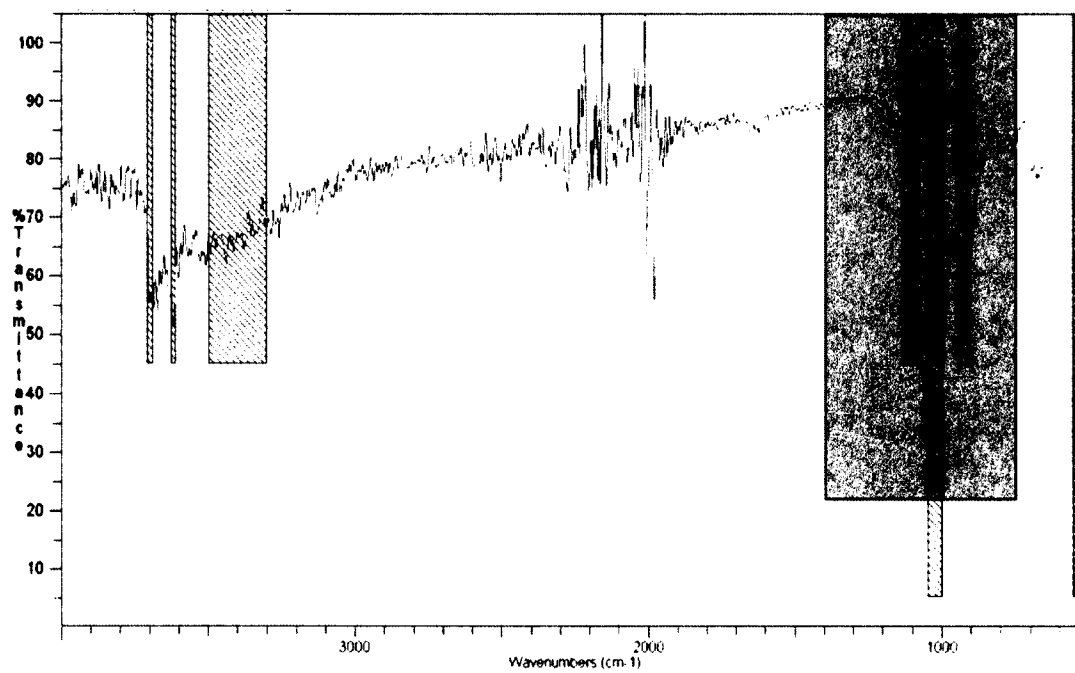


Figure 4-24: FTIR Spectrum of Ag-HNT.

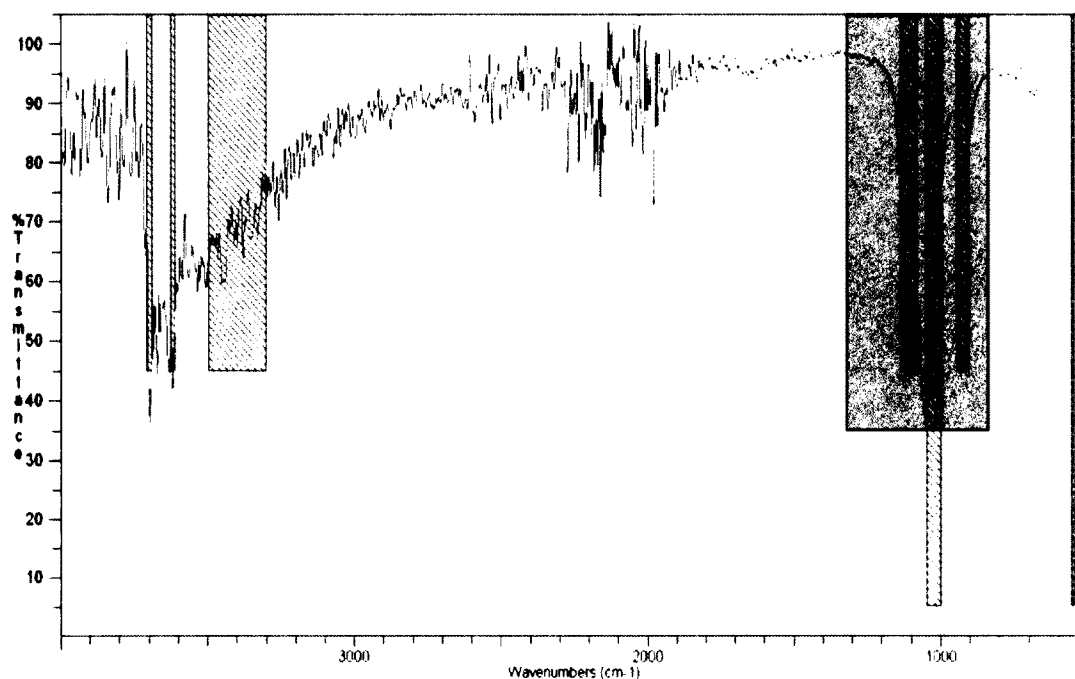


Figure 4-25: FTIR Spectrum of Cu-HNT.

4.2 Metal-HNT Antibacterial Assays

The feasibility of the electrolysis method for creating nanostructured antibacterial coatings on HNTs was confirmed in a series of experiments designed to optimize inhibitory responses of Gram-negative and Gram-positive bacteria. It was determined that the pure HNTs were not effective at inhibiting growth under dynamic contact conditions (**Figure 4-26** and **Figure 4-27**). As the concentration of Ag-HNT was increased in the broth cultures, the absorbance values were decreased (**Figure 4-28** and **Figure 4-29**). The Ag-HNT was more effective at inhibiting the growth of *E. coli* when compared to *S. aureus*. A 99.9% reduction of *E. coli* was detected for the Ag-HNT samples (2-24 mg.). Similar to Ag-HNT, the Cu-HNT was more effective at reducing *E. coli* growth. As the concentration of Cu-HNT was increased in broth cultures the absorbance values were decreased (**Figure 4-30** and **Figure 4-31**). Ag-HNT was concluded to be more effective than Cu-HNT at reducing bacterial growth in liquid broth assays.

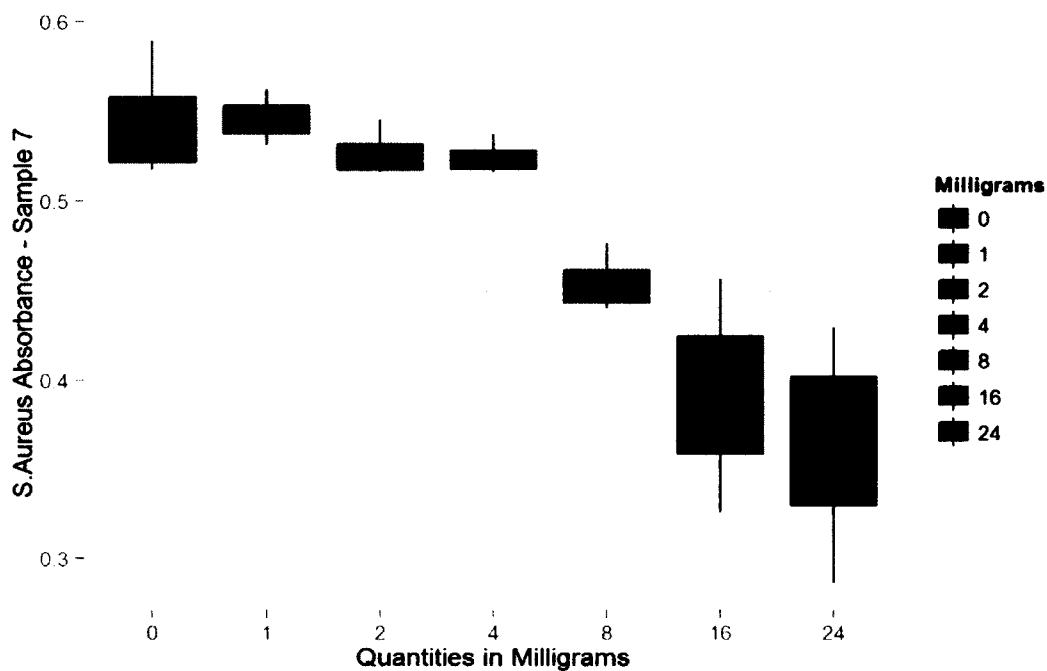


Figure 4-26: Effect of HNT on Absorbance of *S. aureus*.

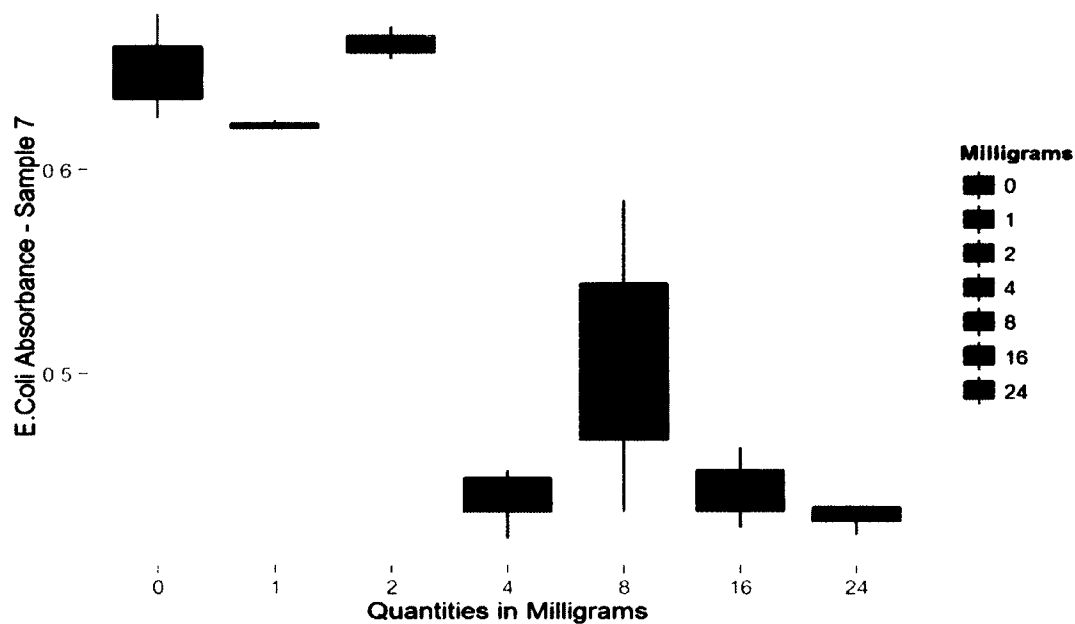


Figure 4-27: Effect of HNT on Absorbance of *E. coli*.

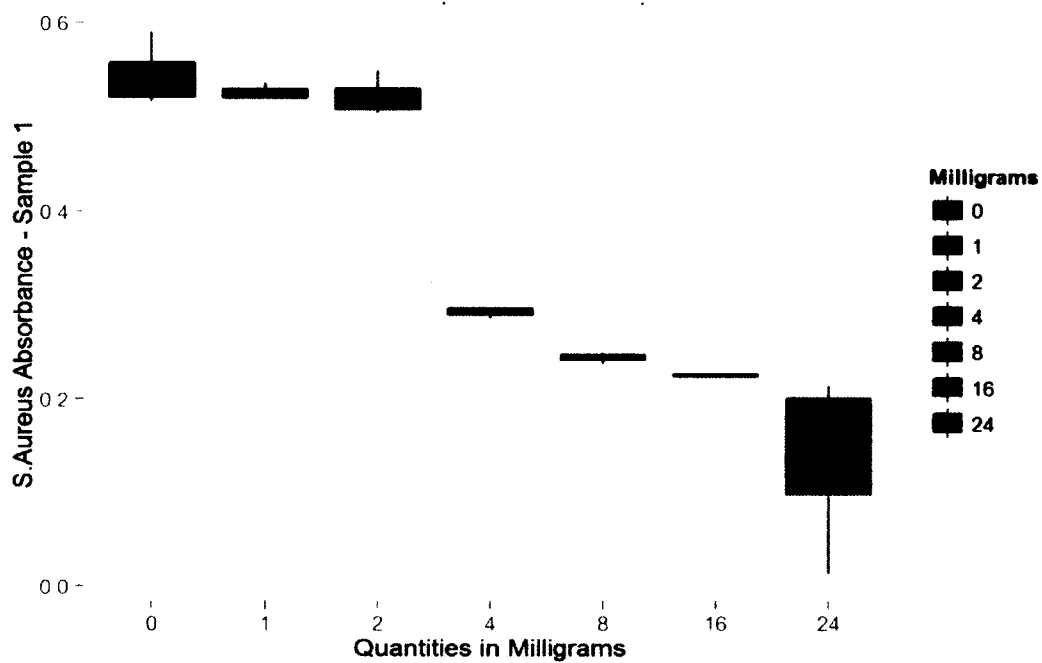


Figure 4-28: Effect of Ag-HNT on Absorbance of *S. aureus*.

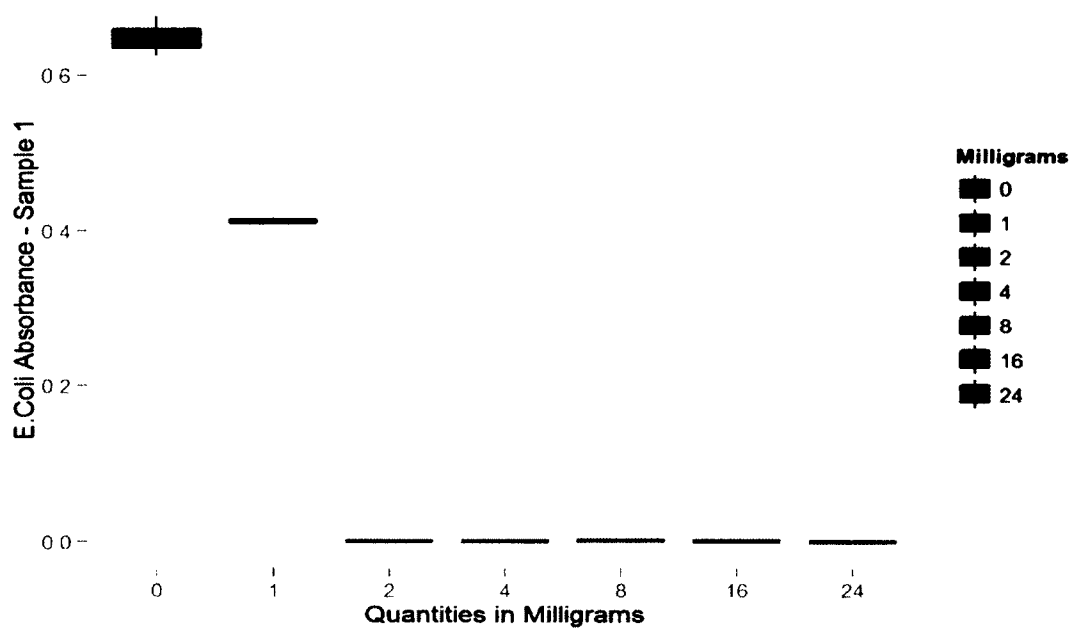


Figure 4-29: Effect of Ag-HNT on Absorbance of *E. coli*.

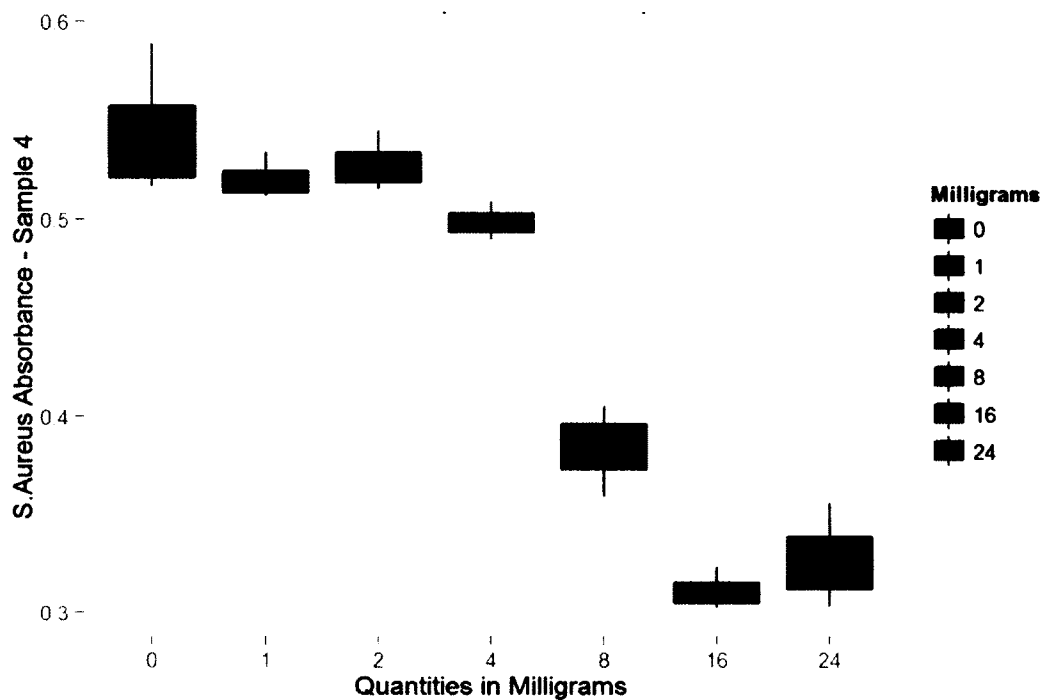


Figure 4-30: Effect of Cu-HNT on Absorbance of *S. aureus*.

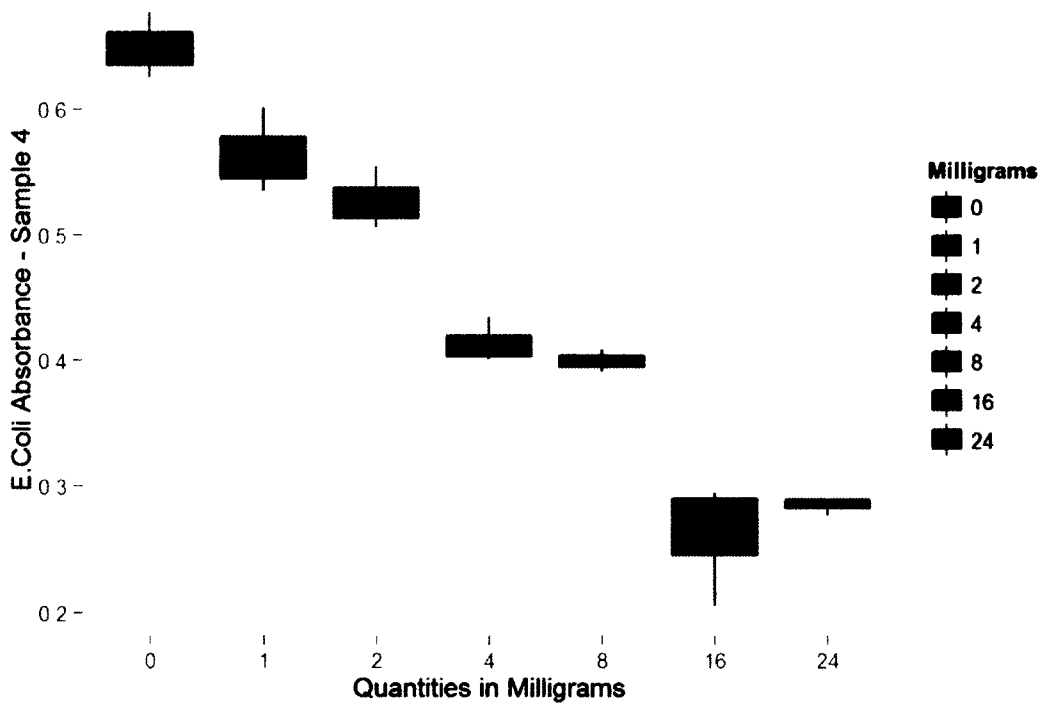


Figure 4-31: Effect of Cu-HNT on Absorbance of *E. coli*.

Ag-HNT-N was effective at inhibiting the growth of *E. coli* and *S. aureus* in broth cultures (Figure 4-32 and Figure 4-33). The growth of *S. aureus* significantly decreased at 4-24 mg. concentrations (Figure 4-32). Similar to Ag-HNT, the Ag-HNT-N decreased *E. coli* by 99% at 2-24 mg. concentrations (Figure 4-33).

The Cu-HNT-N powder was also effective at inhibiting the growth of *E. coli* and *S. aureus*. (Figure 4-34 and Figure 4-35). Cu-HNT-N decreased the absorbance of *S. aureus* by 99% at 16-24 mg. concentrations (Figure 4-34) and decreased the absorbance of *E. coli* by 99% at 4-24 mg. concentrations (Figure 4-35). The loading of nitrofurantoin in Cu-HNT and Ag-HNT samples resulted in greater inhibitory effects on growth of *E. coli* and *S. aureus*.

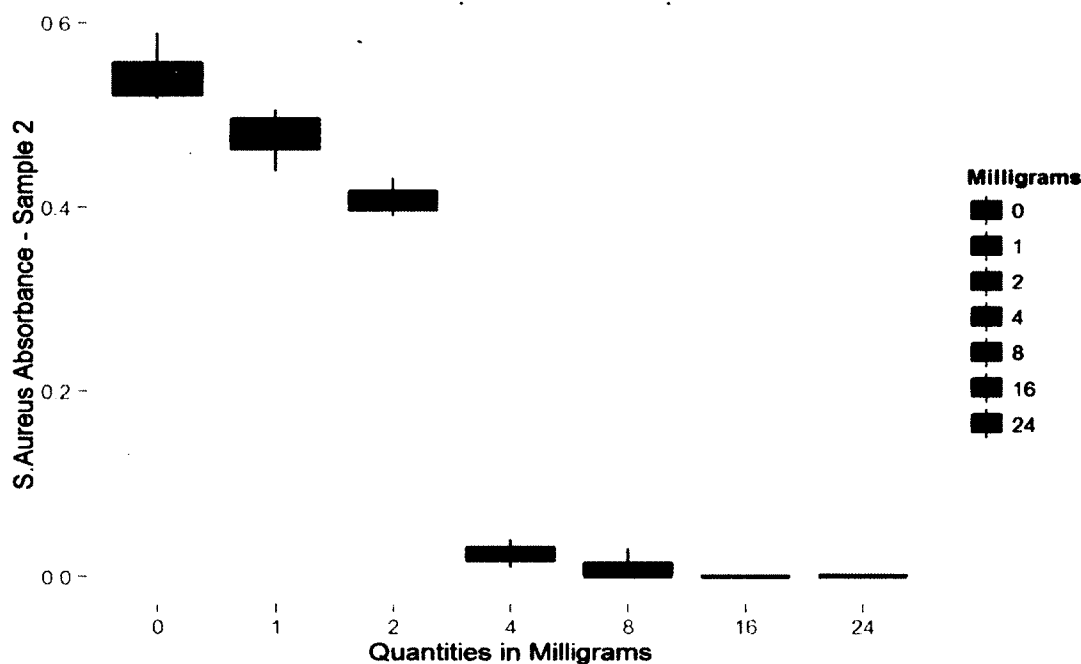


Figure 4-32: Effect of Ag-HNT-N on Absorbance of *S. aureus*.

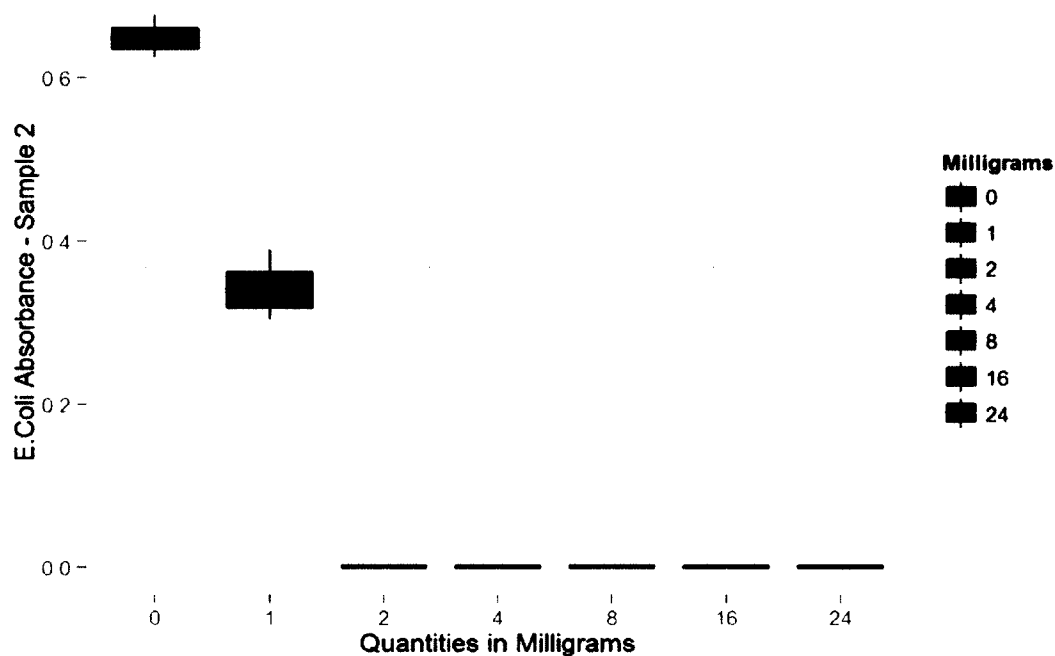


Figure 4-33: Effect of Ag-HNT-N on Absorbance of *E. coli*.

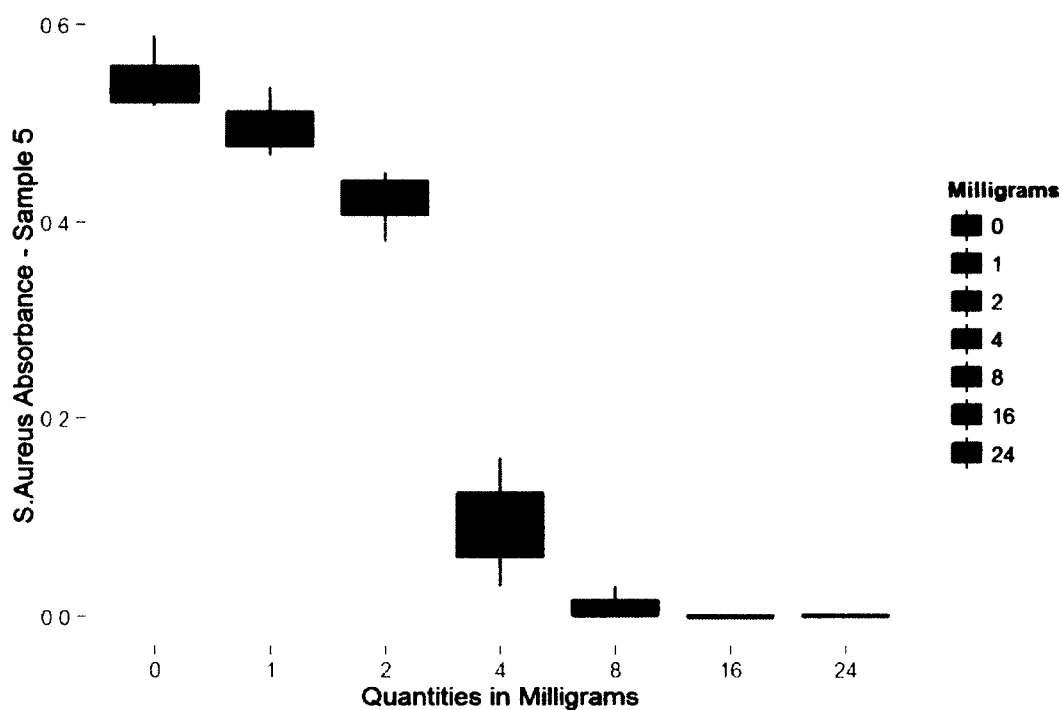


Figure 4-34: Effect of Cu-HNT-N on Absorbance of *S. aureus*.

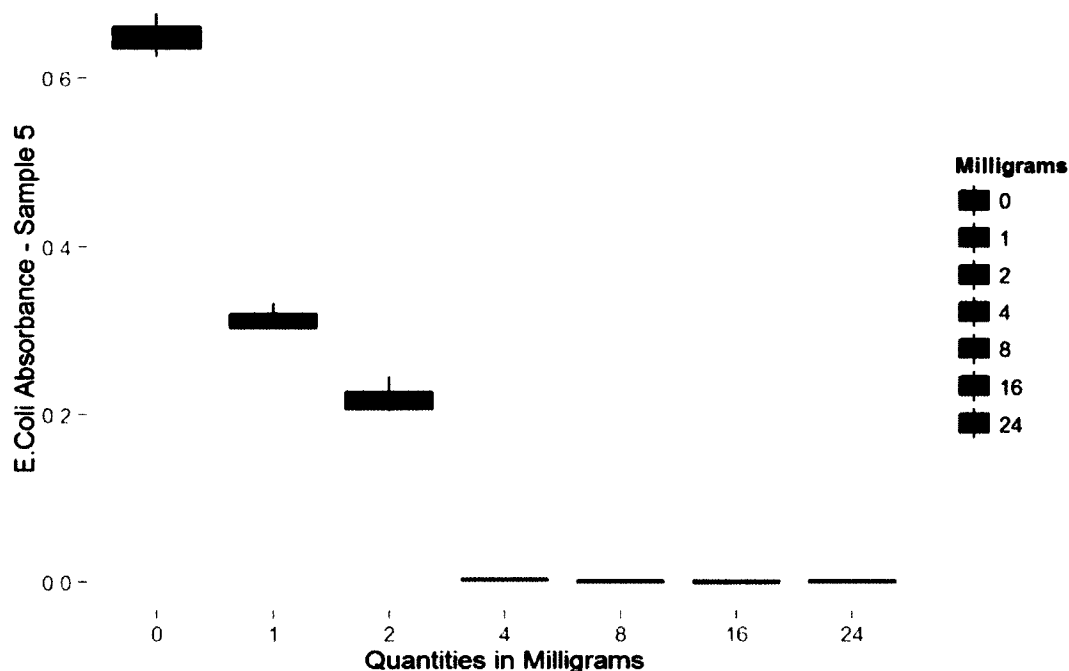


Figure 4-35: Effect of Cu-HNT-N on Absorbance of *E. coli*.

Ag-HNT-N-S was effective at inhibiting *E. coli* and *S. aureus* (Figure 4-36 and Figure 4-37). As the concentration of the Ag-HNT-N-S was increased, the absorbance was decreased. The Ag-HNT-N-S showed similar inhibiting effects against *S. aureus* as compared to Ag-HNT-N (Figure 4-36). Ag-HNT-N-S reduced *E. coli* absorbances by 99% at 2-24 mg. concentrations (Figure 4-37). Cu-HNT-N-S showed significant reductions of *E. coli* and *S. aureus* at 4-24 mg. concentrations (Figure 4-38 and Figure 4-39). Overall, it was concluded that by increasing the concentration of metallized HNTs in the inoculated broth cultures, *E. coli* and *S. aureus* concentrations were decreased.

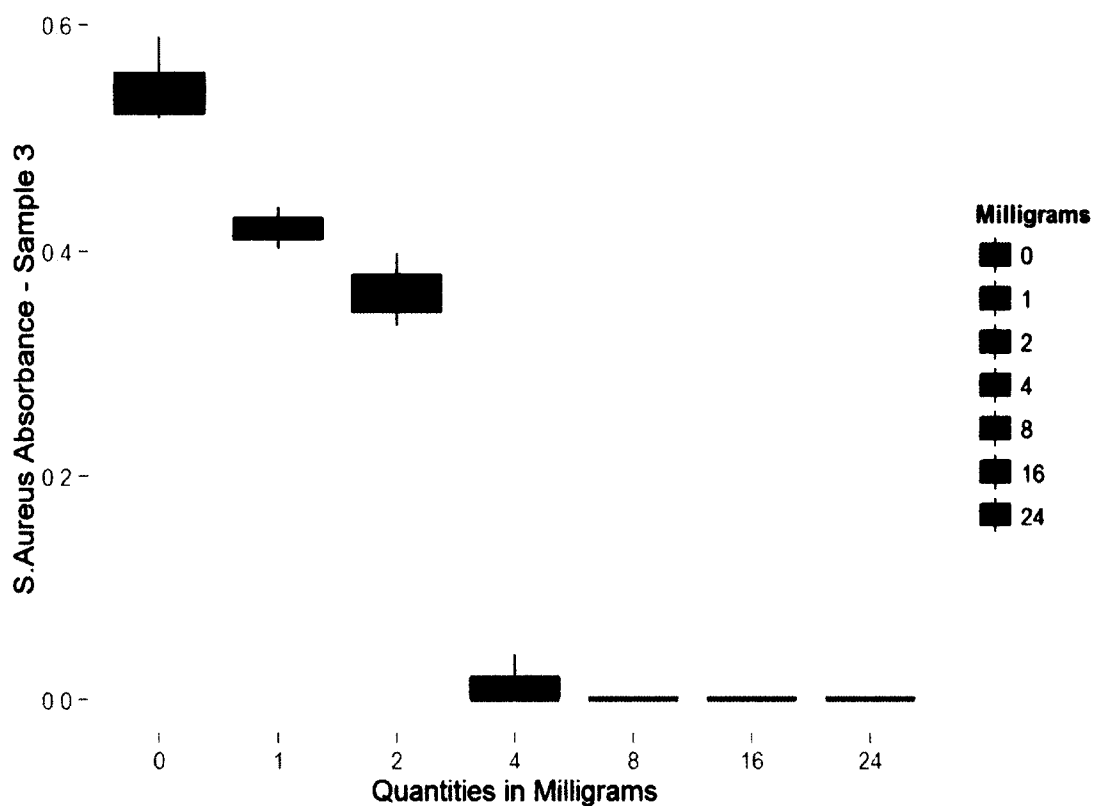


Figure 4-36: Effect of Ag-HNT-N-S on Absorbance of *S. aureus*.

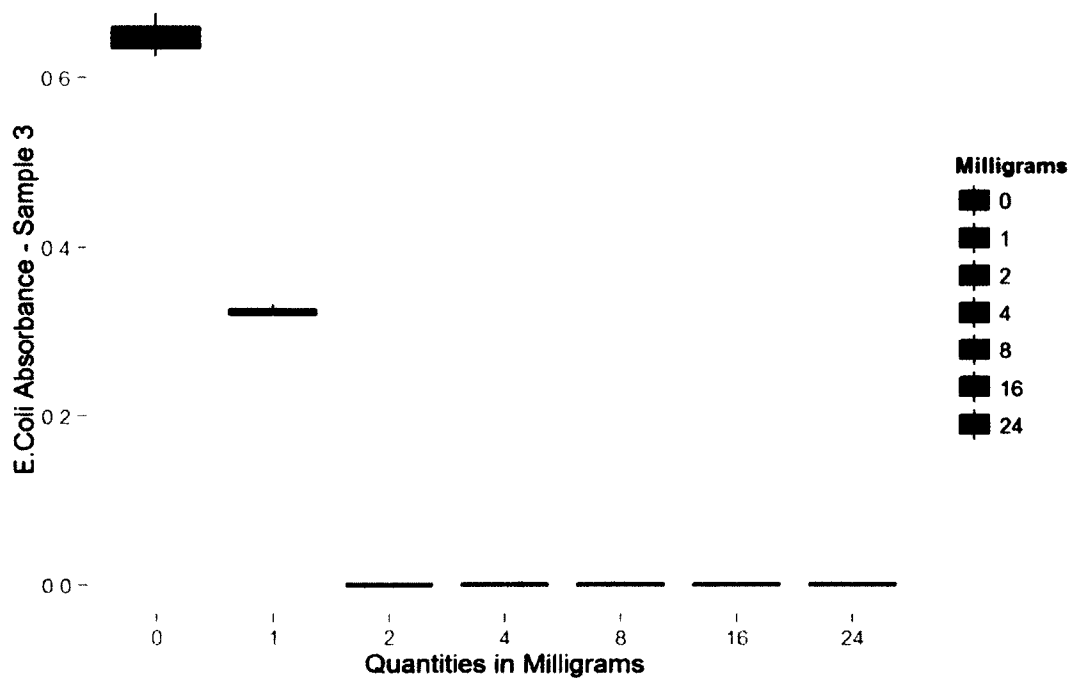


Figure 4-37: Effect of Ag-HNT-N-S on Absorbance of *E. coli*.

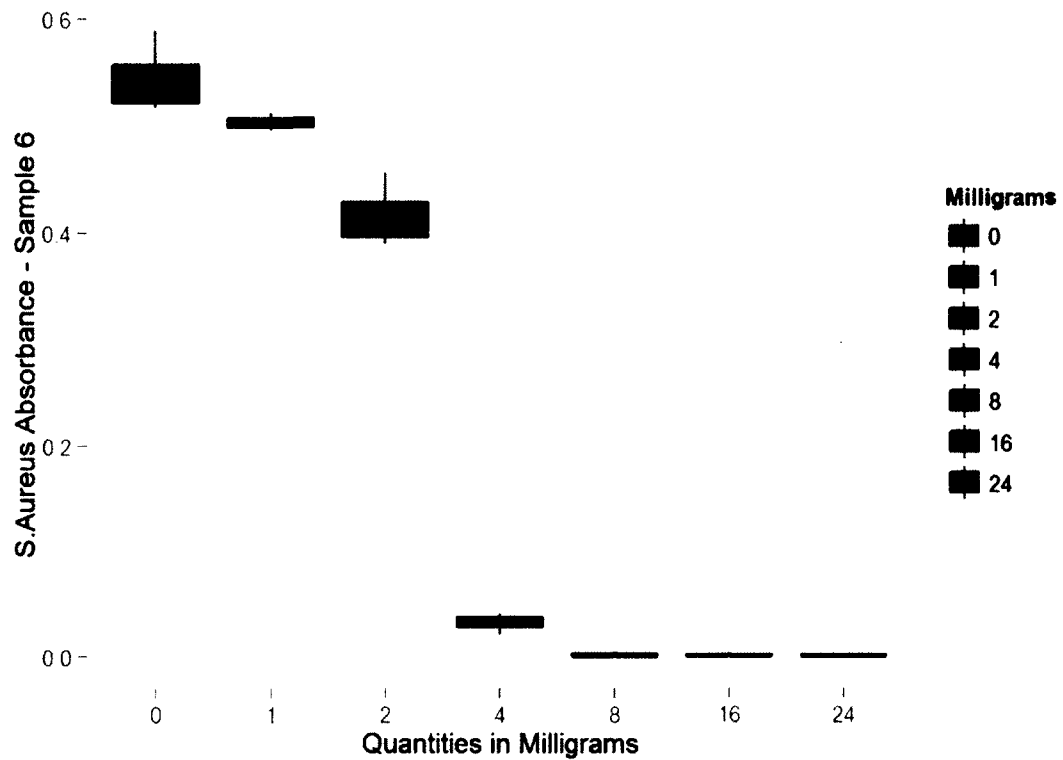


Figure 4-38: Effect of Cu-HNT-N-S on Absorbance of *S. aureus*.

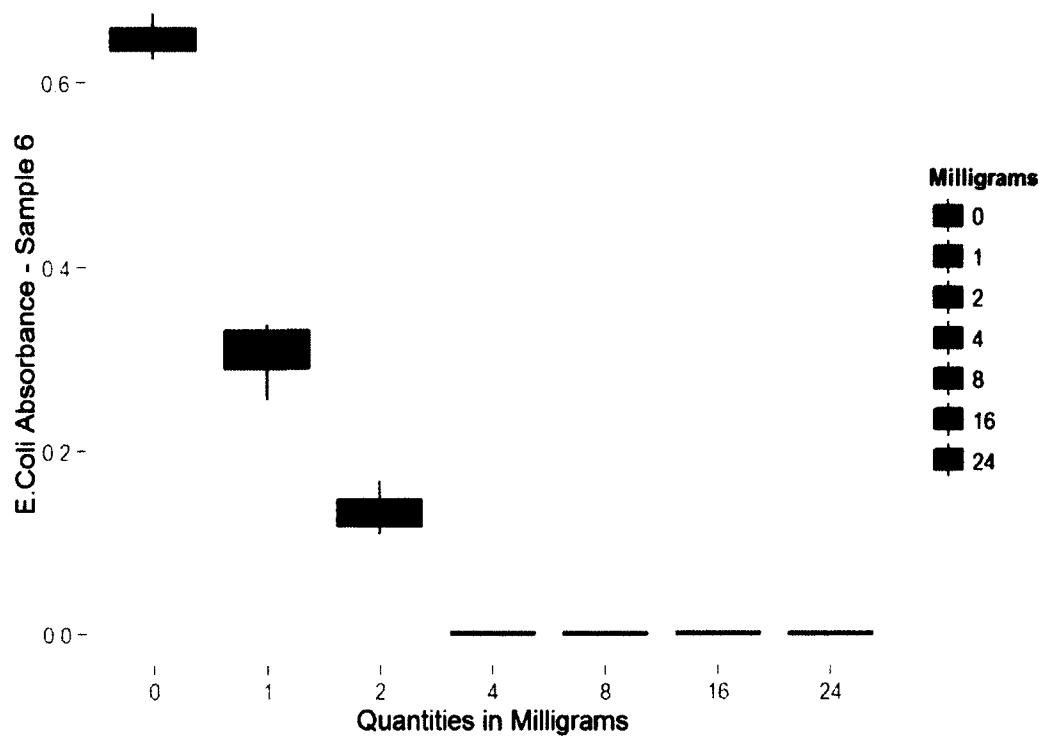


Figure 4-39: Effect of Cu-HNT-N-S on Absorbance of *E. coli*.

All metal-HNT samples reduced *E. coli* growth in broth cultures (Figure 4-40). Cu-HNT and Ag-HNT reduced the turbidity of *S. aureus* broth cultures; however, the nitrofurantoin-loaded versions were most effective (Figure 4-41). There were consistent trends across each type of nanoparticle tested (Figure 4-42), where as the concentration was increased, the amount of bacteria growth was decreased. For broth tests, the concentrations (mg.) were the predictor variables and the bacteria absorbance values were the response data. The HNT-metal composites displayed high correlation and the P-values were lower than 0.05, which showed that the concentration of metallized HNTs could be used as accurate predictors of the response characteristics of *E. coli* and *S. aureus* (Figure 4-42).

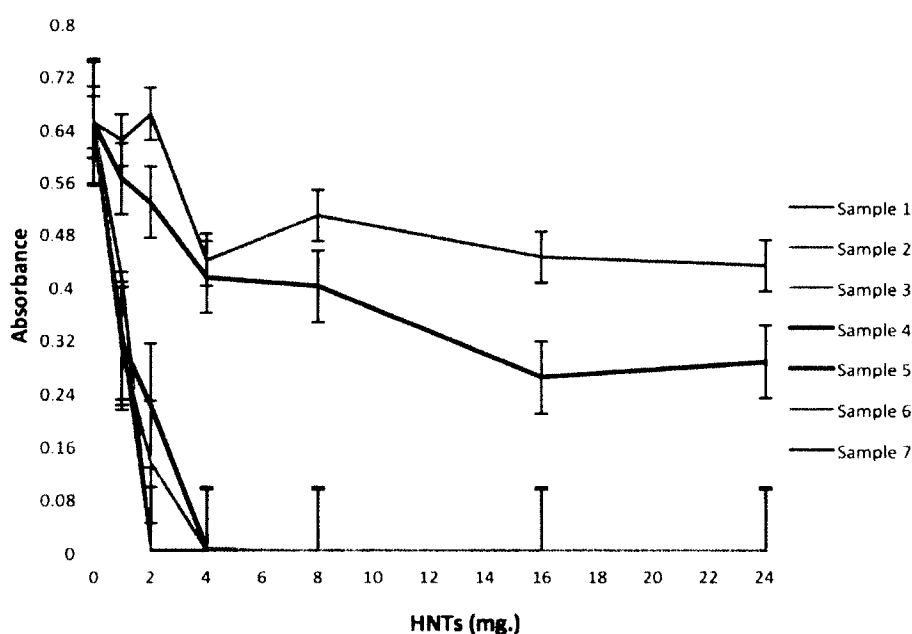


Figure 4-40: Effect of Concentration of HNTs on Absorbance of *E. coli*. Samples: 1) Ag-HNT, 2) Ag-HNT-N, 3) Ag-HNT-N-S, 4) Cu-HNT, 5) Cu-HNT-N, 6) Cu-HNT-N-S, and 7) HNT.

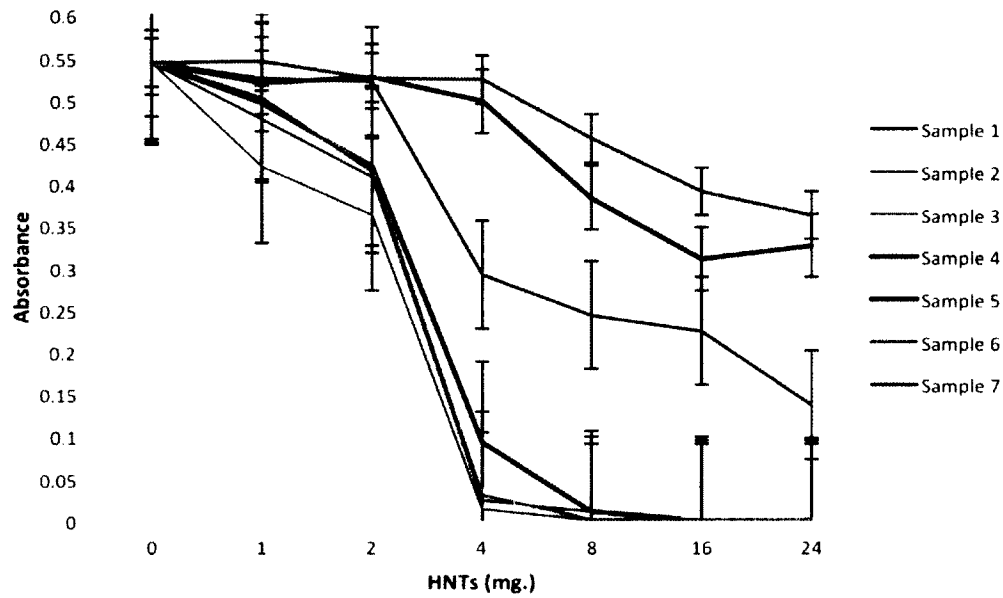


Figure 4-41: Effect of concentration of HNTs on Absorbance of *S. aureus*. Samples: 1) Ag-HNT, 2) Ag-HNT-N, 3) Ag-HNT-N-S, 4) Cu-HNT, 5) Cu-HNT-N, 6) Cu-HNT-N-S, and 7) HNT.

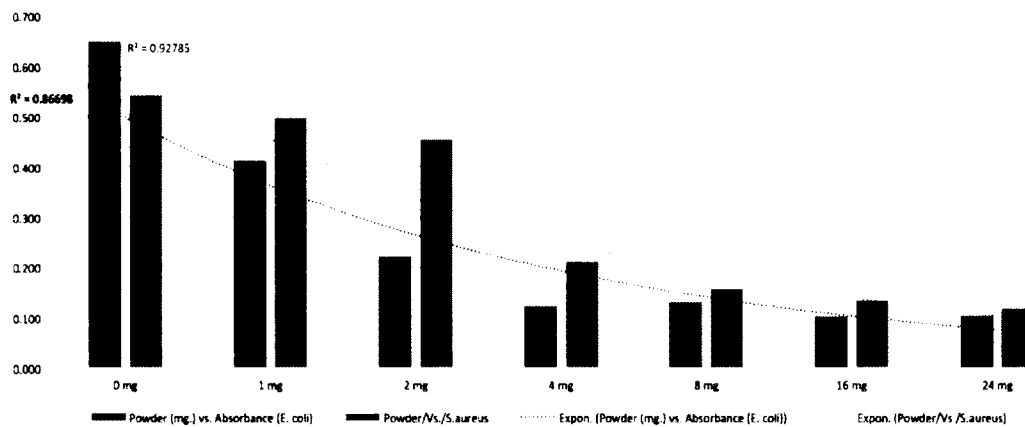


Figure 4-42: Effect of concentration of HNTs on Absorbance of *E. coli* and *S. aureus* with Correlation and Exponential Comparison.

Mueller-Hinton agar assays were used for qualitative analysis of the metal-HNTs.

Dense biofilm formation occurred on the control HNT sample and displayed no ZOI

(Figure 4-43: A). Metallized-HNTs were effective at reducing bacteria growth and

biofilm formation near the surfaces. Ag-HNT displayed a large ZOI and prevented biofilm formation on the surfaces (**Figure 4-43: B**).

Cu-HNT displayed a smaller ZOI and appeared to have changed colors during the assay (**Figure 4-43: C**). In all broth and agar tests performed, the Cu-HNT changed from brown to a white-blue coloration after incubation. It was assumed that oxidation reactions occurred during the incubation periods with Cu-HNT.

In agar and broth assays, Ag-HNT particles retained gray coloration during incubation periods with bacteria (**Figure 4-43: B**). Black Ag-oxide powder was used for color change comparison with Ag-HNT, and color change was not detected for Ag-HNT during incubation periods (**Figure 4-43: B and E**). The Ag-oxide powder converted to a red-orange color during incubation periods. Ag-HNT-N-S displayed a large zone of inhibition and appeared to enhance the inhibiting effect of the Ag (**Figure 4-43: F**). A standard nitrofurantoin disc was used for comparison with Ag-HNT-N-S (**Figure 4-43: D**).



Figure 4-43: Effect of HNTs on *E. coli* in Agar Diffusion Assays. Sample: A) HNT, B) Ag-HNT, C) Cu-HNT, D) Nitrofurantoin disc, E) Ag-Oxide, F) Ag-HNT-N-S.

4.3 Polymer-HNT Composites

4.3.1 PLGA-HNT Nanofibers

Current methods for encapsulating HNTs within nanofibers include electrospinning, which has many limitations such as the need for high-voltage and a conductive collection system (Xue *et al.*, 2015). The solution blow-spin method is a more rapid nanofiber production method that can deposit nanofibers on any surface geometry (Behrens *et al.*, 2014). The feasibility of using the solution blow-spin method for encapsulation of HNTs in nanofibers was validated through electron microscopy.

The nanofibers produced through solution blow-spinning displayed a variety of surface morphologies when viewed under SEM and TEM. Image J analysis of pure PLGA fibers generated data with a mean fiber diameter of 678.5 nm. +/- 170 nm. (**Figure 4-44** and **Figure 4-45**). The pure PLGA fibers had diameters as low as 68 nm. and as high as 692 nm. (**Figure 4-44**). For PLGA-HNT fibers, larger diameters were detected with a mean average of 793 nm. +/- 456 nm. (**Figure 4-45**). PLGA-HNT fibers had a minimum diameter of 62 nm. and a maximum diameter of 1.7 micrometers (μm) (**Figure 4-45**).

TEM images of solution blown PLGA showed a uniform fiber formation (**Figure 4-46**). Solution blown PLGA with HNTs appeared to encapsulate the HNTs during solvent evaporation and was clearly visible in TEM images (**Figures 4-47**). Fiber networks were more uniform in the pure PLGA nanofibers. Solution blow spun PLGA-HNT showed for the first time that HNTs could be encapsulated within sprayed nanofiber networks.

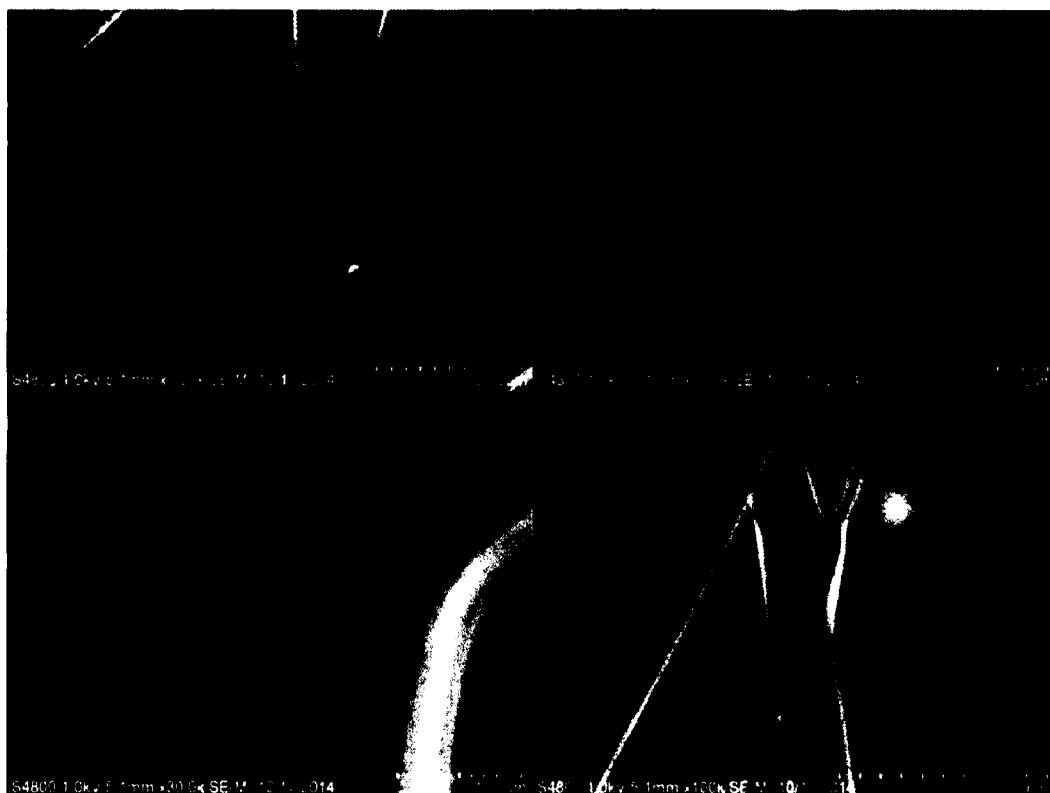


Figure 4-44: SEM Images PLGA Nanofibers.

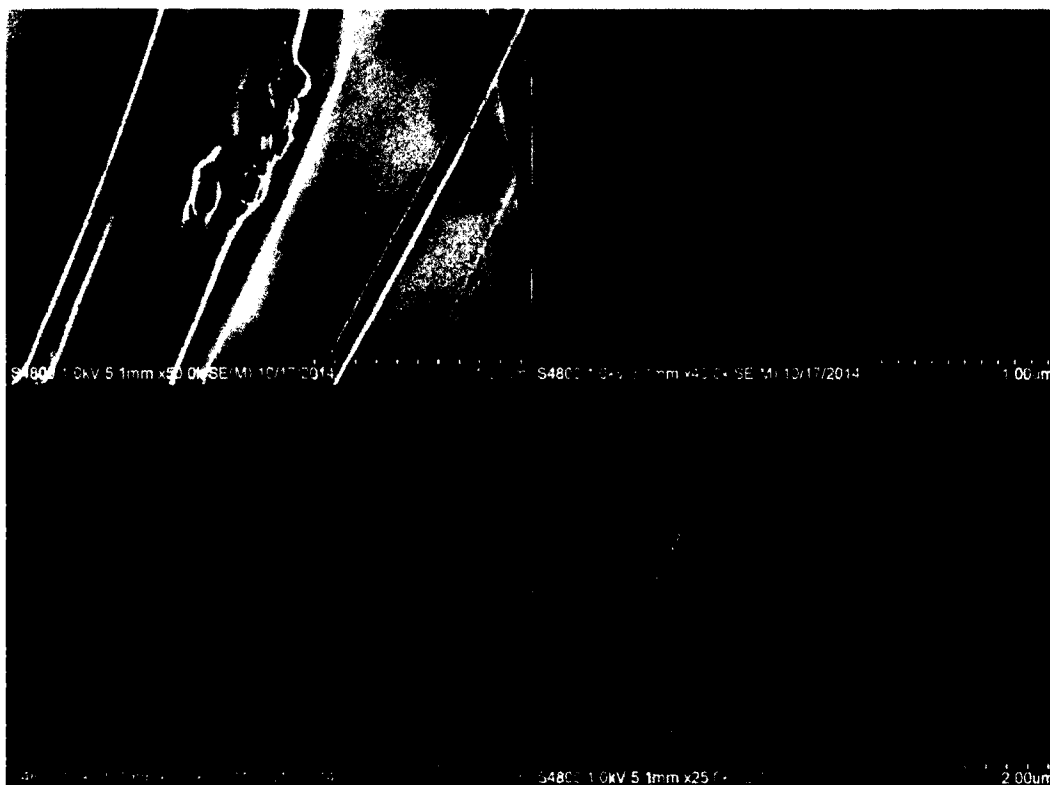


Figure 4-45: SEM Images of PLGA-HNT Nanofibers.



Figure 4-46: TEM Images of PLGA Nanofibers.

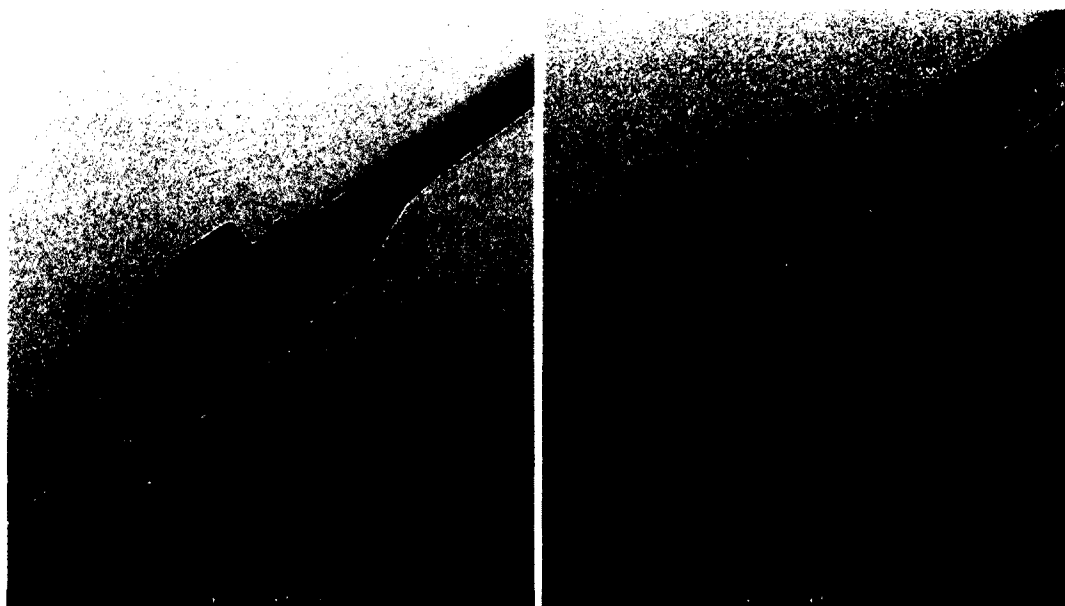


Figure 4-47: TEM Images of PLGA-HNT Nanofibers.

The feasibility of HNT-loaded PLGA nanofibers as multifunctional antibacterial substrates was demonstrated in Mueller-Hinton broth assays. PLGA and PLGA-HNT were not effective at reducing *E. coli* growth (Figure 4-48: 2 and 3). Ag-HNT, Ag-HNT-

N, and Ag-HNT-N-S were effective at reducing *E. coli* absorbance values (Figure 4-48: 4, 6, and 8). Cu-HNT had a slight inhibiting effect on *E. coli* (Figure 4-48: 5). Cu-HNT-N and Cu-HNT-N-S showed significant reduction of *E. coli* (Figure 4-48: 7 and 9). Results concluded that the *E. coli* concentration was decreased effectively in the samples containing Ag and nitrofurantoin and appeared to enhance inhibition.

PLGA, PLGA-HNT, PLGA-HNT-Ag, and PLGA-HNT-Cu were not effective at reducing *S. aureus* growth (Figure 4-49: 2, 3, 4, and 5). Samples containing nitrofurantoin showed a greater reduction of bacteria growth (Figure 4-49: 6, 7, 8, and 9).

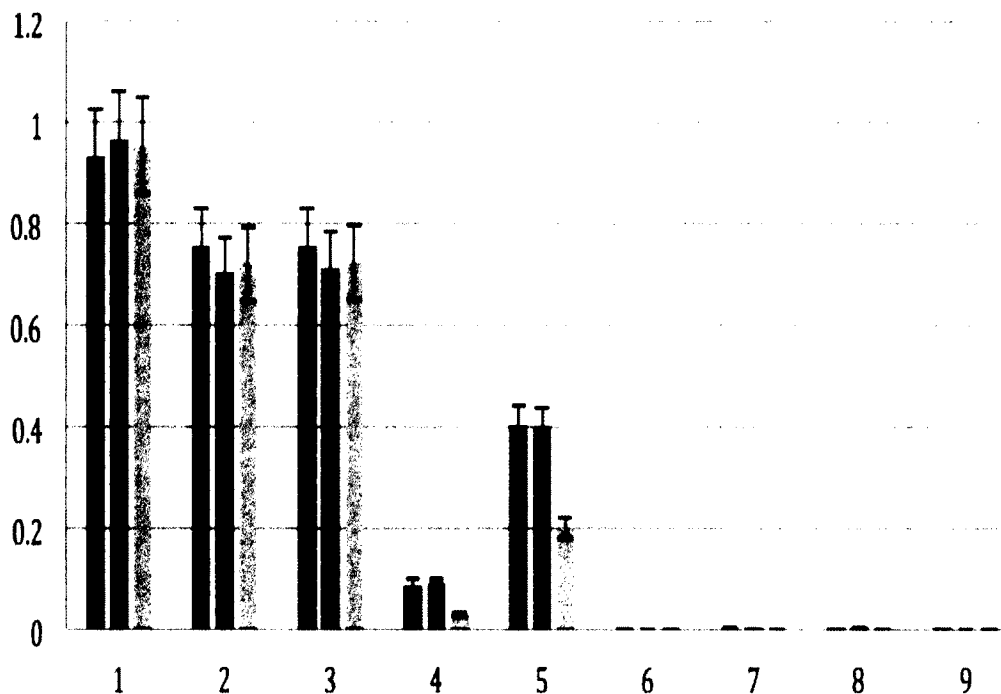


Figure 4-48: Effect of HNT-Nanofibers on Absorbance of *E. coli*. Sample: 1) Control *E. coli*, 2) PLGA, 3) PLGA-HNT, 4) PLGA-Ag-HNT, 5) PLGA-Cu-HNT, 6) PLGA-Ag-HNT-N, 7) PLGA-Cu-HNT-N, 8) PLGA-Ag-HNT-N-S, and 9) PLGA-Cu-HNT-N-S.

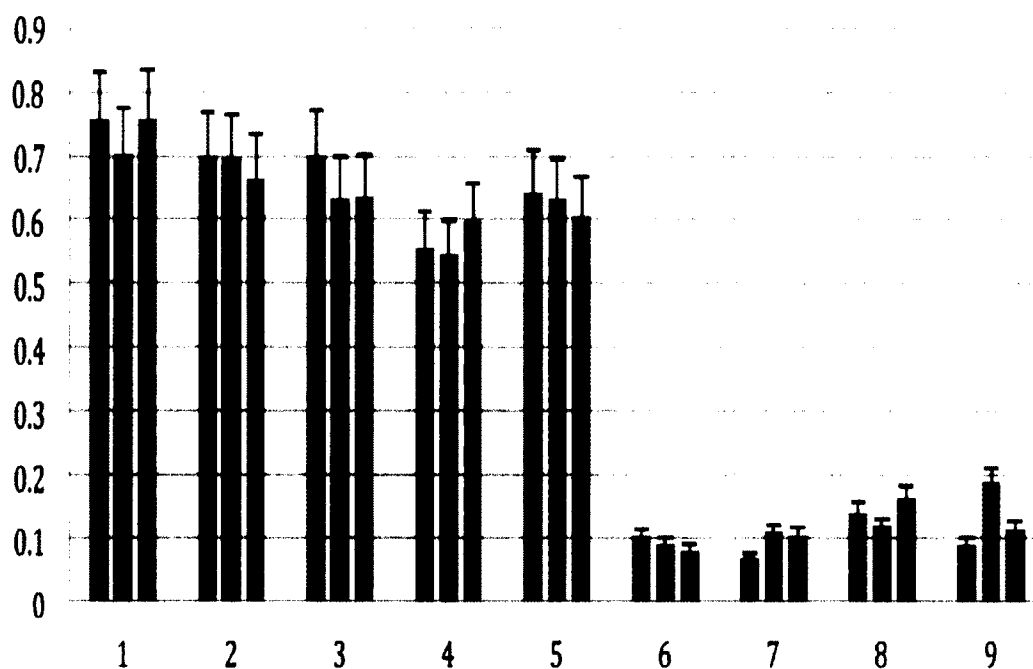


Figure 4-49: Effect of HNT-Nanofibers on Absorbance of *S. aureus*. Sample: 1) Control *S. aureus*, 2) PLGA, 3) PLGA-HNT, 4) PLGA-Ag-HNT, 5) PLGA-Cu-HNT, 6) PLGA-Ag-HNT-N, 7) PLGA-Cu-HNT-N, 8) PLGA-Ag-HNT-N-S, and 9) PLGA-Cu-HNT-N-S.

4.3.2 ABS-HNT and PDMS-HNT

Cu-HNT and Ag-HNT were examined as antibacterial materials for additive manufacturing with ABS plastic. ABS filaments were extruded with HNTs and the bacterial responses were monitored in broth assays. Surface analysis of the ABS filaments showed the dispersion of HNTs on the filaments (**Figure 4-50: A and B**). ABS loaded with Ag-HNT and Cu-HNT displayed different surface morphologies in SEM images (**Figure 4-50: C and D**). The extrusion process was able to produce extruded filaments with HNT clusters scattered along the filament edge.

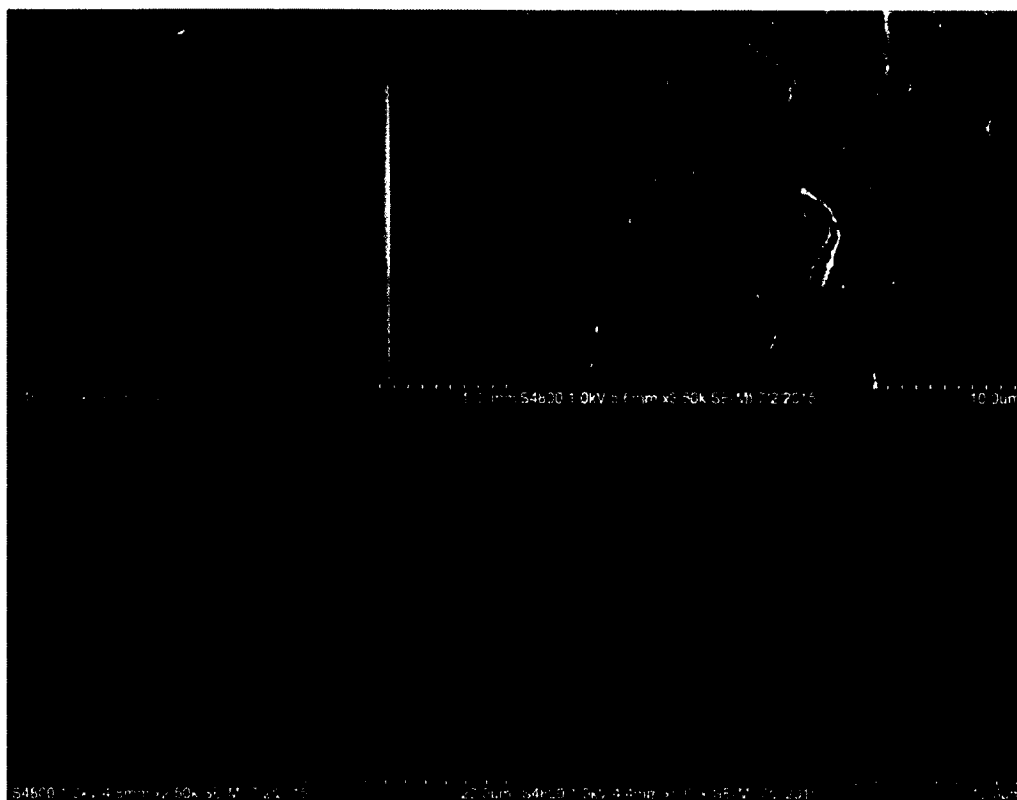


Figure 4-50: SEM Images of A) ABS, B) ABS, C) ABS-Ag-HNT, and D) ABS-Cu-HNT.

Results showed that pure ABS and ABS-HNT were not effective at reducing the growth of *E. coli* and *S. aureus* (**Figure 4-51** and **Figure 4-52: 2** and **3**). ABS-Ag-HNT was not effective at reducing *S. aureus* (**Figure 4-51: 4**). However, ABS-Ag-HNT showed a slight inhibiting effect against *E. coli* (**Figure 4-52: 4**). ABS-Cu-HNT was not effective against *E. coli* and *S. aureus* (**Figure 4-51** and **Figure 4-52: 5**). PDMS-Ag-HNT and PDMS-Cu-HNT samples were not effective at inhibiting *E. coli* and *S. aureus* and displayed high absorbance values (**Figure 4-53** and **Figure 4-54**).

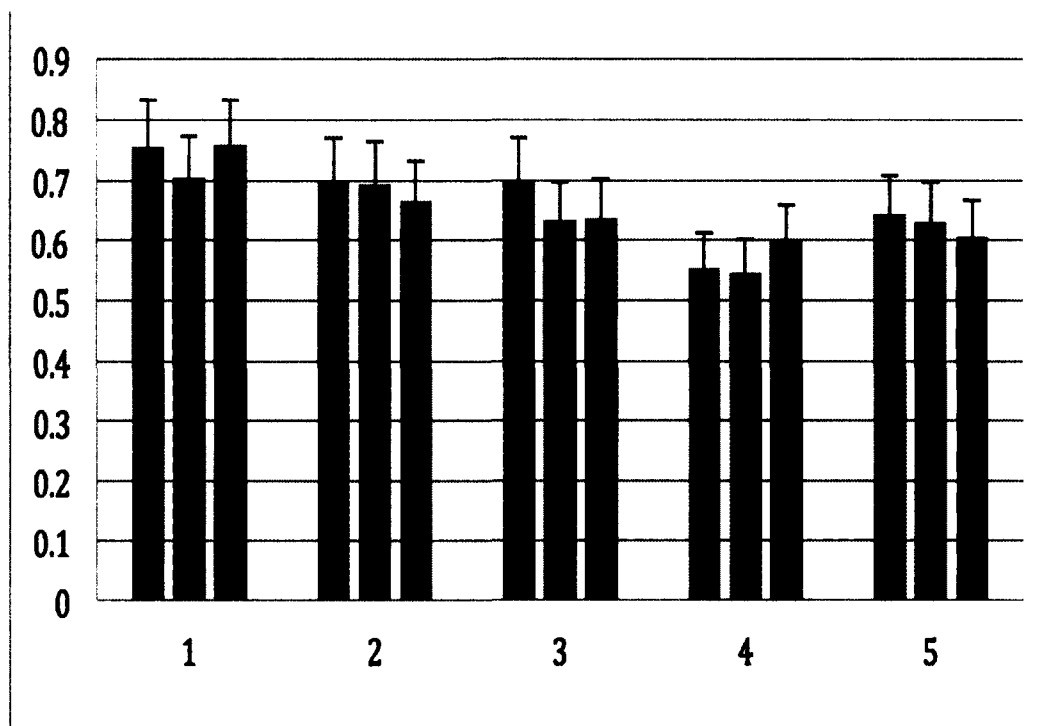


Figure 4-51: Effect of HNT-Filaments on Absorbance of *S. aureus*. Sample: 1) Control *S. aureus*, 2) ABS, 3) ABS-HNT, 4) ABS-Ag-HNT, 5) ABS-Cu-HNT.

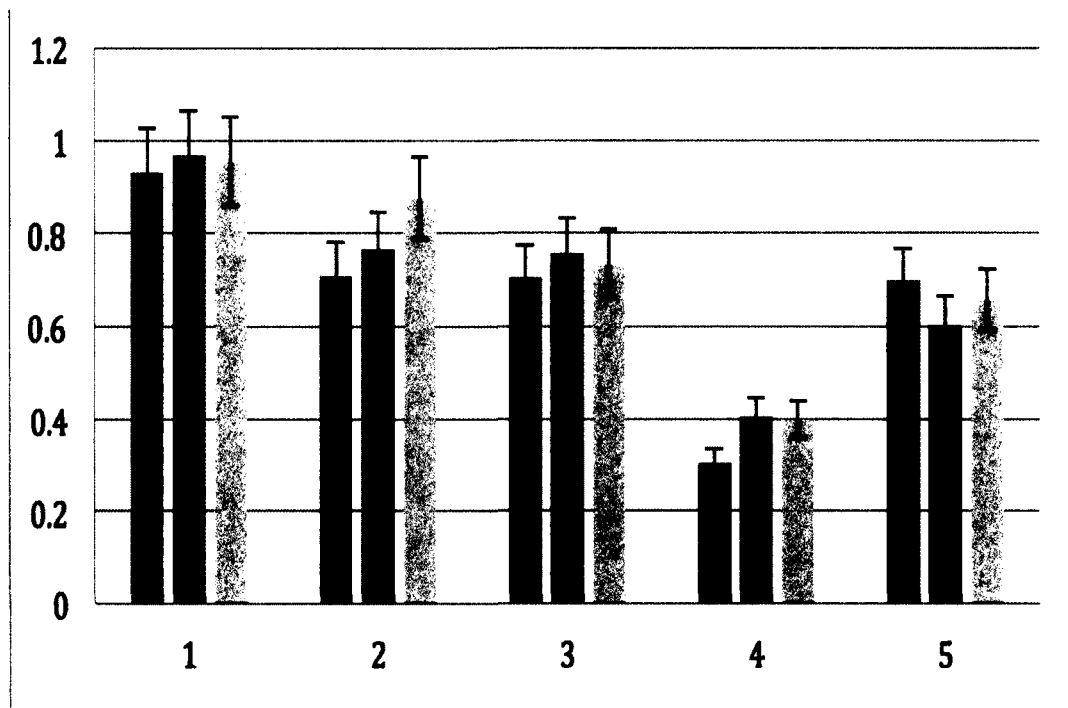


Figure 4-52: Effect of HNT-Filaments on Absorbance of *E. coli*. Sample: 1) Control *E. coli*, 2) ABS, 3) ABS-HNT, 4) ABS-Ag-HNT, 5) ABS-Cu-HNT

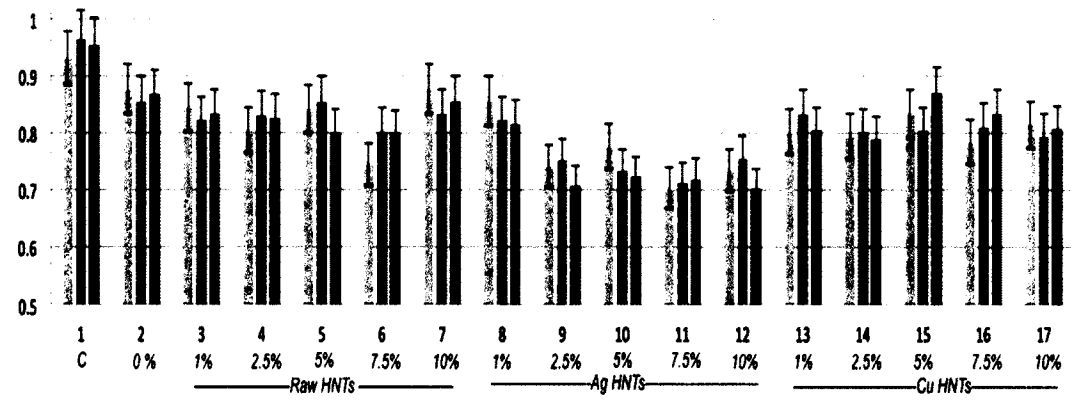


Figure 4-53: Effect of HNT-PDMS Samples on Absorbance of *E. coli*. Sample: 1) Control *E. coli*, 2) PDMS, PDMS-HNT (3-7), PDMS-Ag-HNT (8-12), and PDMS-Cu-HNT (13-17).

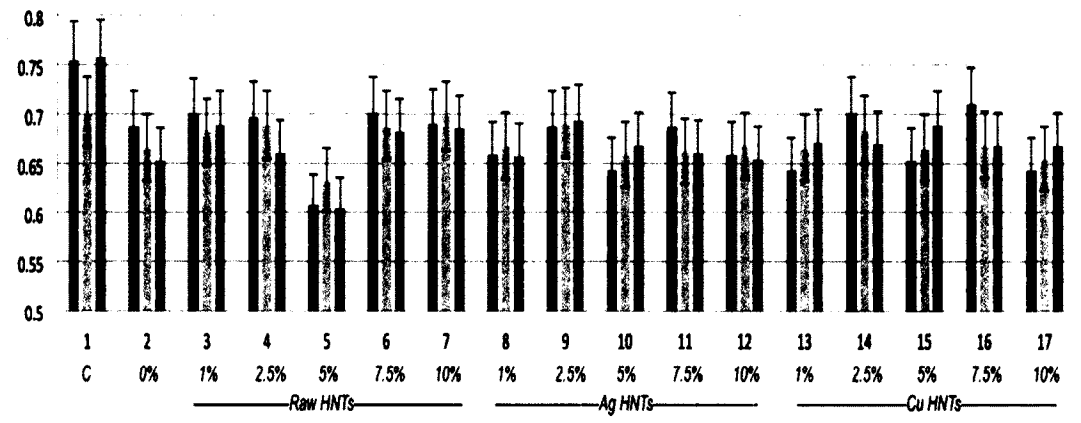


Figure 4-54: Effect of HNT-loaded PDMS Samples on Absorbance of *S. aureus*. Sample: 1) Control *S. aureus*, 2) PDMS, PDMS-HNT (3-7), PDMS-Ag-HNT (8-12), and PDMS-Cu-HNT (13-17).

4.3.3 PDMS-HNT-PEO-N

The feasibility of the PDMS-HNT-PEO-N for creating nanostructured antibacterial coatings was confirmed in a series of experiments designed to optimize inhibitory responses of Gram-negative and Gram-positive bacteria. PDMS-HNT-PEO composites loaded and coated with nitrofurantoin showed competitive antibacterial performance when compared with commercial antibacterial urinary PDMS catheters (Figure 4-55 and Figure 4-56: A and C). Table 4-1, and Table 4-2 also show the

effectiveness of PDMS-HNT-PEO-N against Gram-negative and Gram-positive bacteria. For Mueller-Hinton leaching agar assays, the 100% PDMS catheters and silver catheter were not effective. PDMS-HNT-PEO-N and drug-coated catheters were shown to be the most effective at inhibiting both bacteria types in both agar and broth assays.

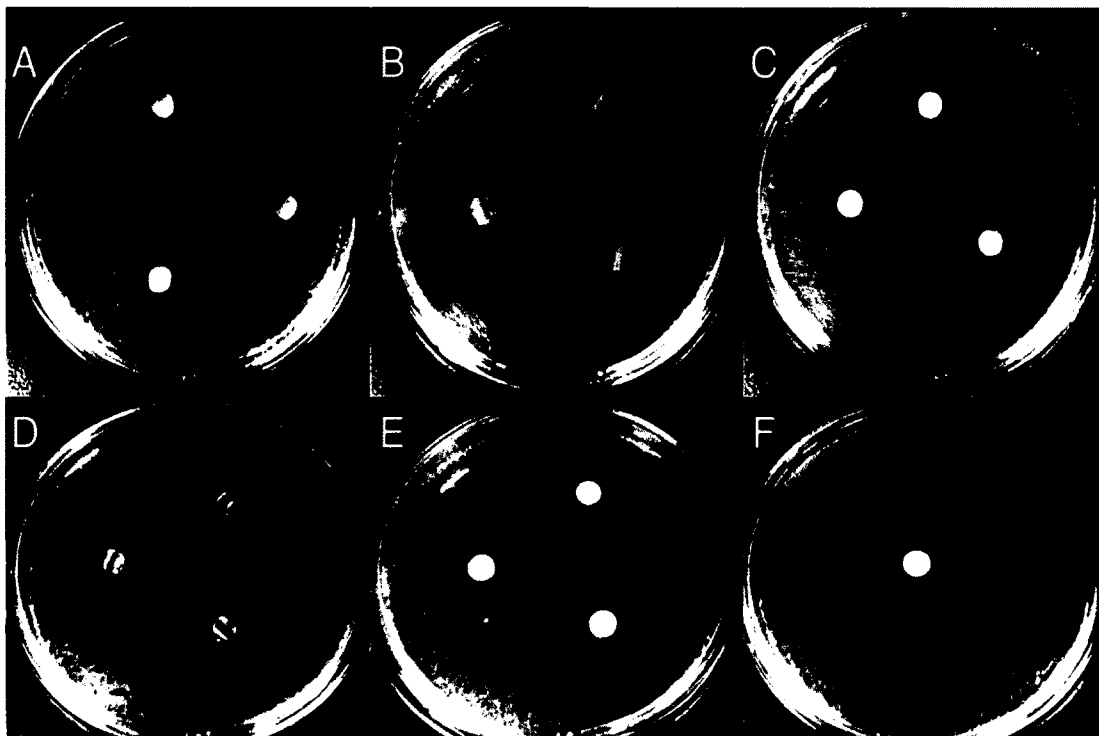


Figure 4-55: Images of PDMS samples in Agar Disc Diffusion Assays Against *E. coli*. A) Antibacterial Catheter, B) Silver Coated Catheter, C) PDMS-HNT-PEO-N, D) 100% PDMS Catheter, E) PDMS-HNT-PEO, and F) Nitrofurantoin Disc.

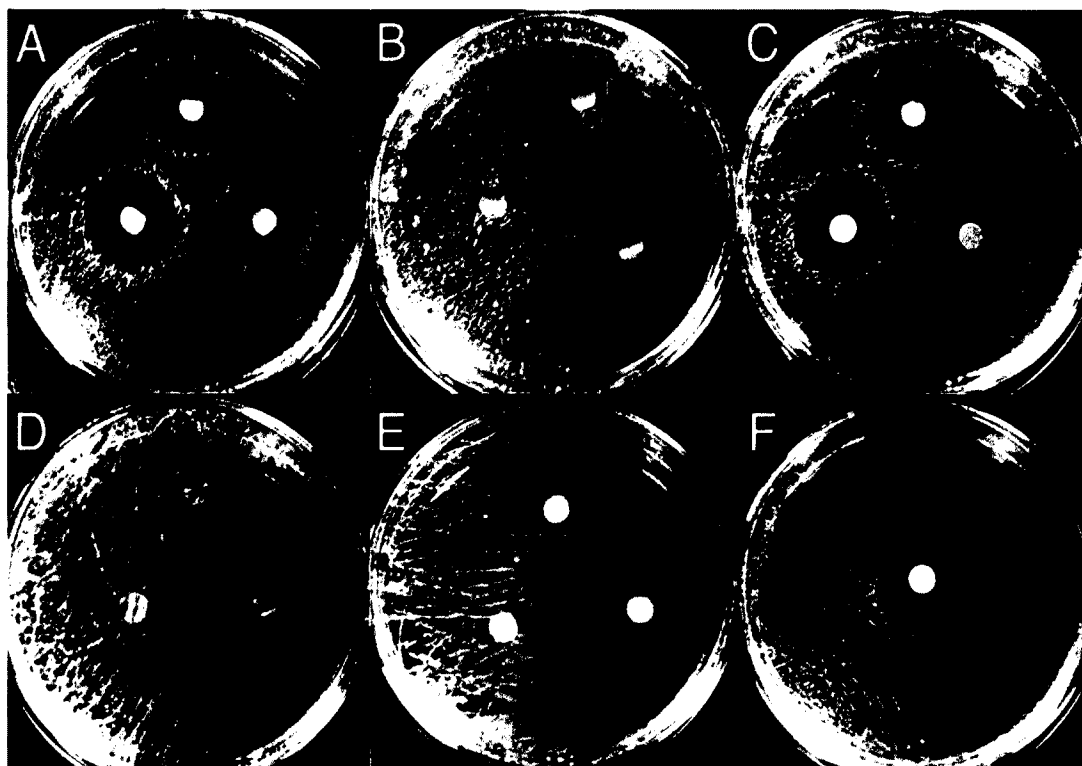


Figure 4-56: Images of PDMS Samples in Agar Disc Diffusion Assays Against *S. aureus*. A) Antibacterial Catheter, B) Silver Coated Catheter, C) PDMS-HNT-PEO-N, D) 100% PDMS Catheter, E) PDMS-HNT-PEO, and F) Nitrofurantoin Disc.

Table 4-1: Table Showing Mueller-Hinton Agar Zone of Inhibition Results for Commercial Catheters and PDMS-HNT.

Sample	ZOI (mm.) <i>E. coli</i>	ZOI (mm.) <i>S. aureus</i>
Nitrofurantoin Disc	19.730 ± 1.219	20.166 ± 0.650
PDMS-HNT-PEO-N	21.100 ± 1.326	21.955 ± 0.612
PDMS-HNT	No ZOI	No ZOI
Antibacterial Catheter	18.222 ± 0.864	20.300 ± 1.400
Silver Catheter	No ZOI	7.322 ± 2.100
100% PDMS Catheter	No ZOI	No ZOI

Table 4-2: Table Showing Mueller-Hinton Broth Absorbance Results for PDMS-HNT.

Sample	Abs. (600 nm.) <i>E. coli</i>	Abs. (600 nm.) <i>S. aureus</i>
Control <i>E. coli</i>	0.967 ± 0.016	-
Control <i>S. aureus</i>	-	0.923 ± 0.011
Nitrofurantoin Disc	0.001 ± 0.001	0.047 ± 0.009
PDMS-HNT-PEO-N	0.002 ± 0.001	0.009 ± 0.015
PDMS-HNT	0.700 ± 0.073	0.565 ± 0.068
Antibacterial Catheter	0.001 ± 0.002	0.012 ± 0.019
Silver Catheter	0.798 ± 0.151	0.657 ± 0.074
100% PDMS Catheter	0.873 ± 0.020	0.763 ± 0.032

CHAPTER 5

DISCUSSION

5.1 Metal-HNT Electrolysis Fabrication

The phenomenon of electrolysis remains an important chemical effect in chemistry and manufacturing. The technique uses D/C to drive an otherwise non-spontaneous chemical reaction through a solution. Several methods of electrolysis have since been developed for industry, which include electro-refining, electro-synthesis, and electroplating. Electrolysis continues to be a valuable technique for chemists, scientists, and industrial scale productions (Allanore, 2012).

Current methods for fabricating metal-HNT composites rely on multi-step processing with metal-compounds, metal-salts, reducing agents, chemicals, and high temperatures (Abdullayev *et al.*, 2011; Chen *et al.*, 2012; Liu and Zhao, 2009; Rawtani and Agrawl, 2012; Tang *et al.*, 2013; Zhang *et al.*, 2013; Zhen *et al.*, 2011). The previous metal-HNT fabrication methods focus on using a specific metal with multi-step reactions.

In this first ever account, the electrolysis method was shown to act as a new route, in which multiple types of metal could be deposited on HNT surfaces. In water with neutral pH 7, the outer silica surface of HNTs display a negative zeta-potential (Lvov *et al.*, 2008). It is theorized that the electrolysis produces Ag and Cu nanoparticles with positive zeta-potential and facilitates deposition on the HNT surfaces (**Figure 4-1** and **Figure 4-2**). It is suggested that HNTs act as a support system and may extend the

shelf life of the metal nanoparticles. EDAX readings of HNT, Ag-HNT samples, and Cu-HNT samples proved that electrochemical deposition is an effective route to create HNT-metal composites (**Figure 4-3, Figure 4-4, Figure 4-5, Figure 4-6, and Figure 4-7**). It is suggested that the concentration of metal deposited is dependent on the concentration of HNTs and amount of time under electrolysis. For example, Ag-HNT fabricated at 300 mg. showed a much higher Ag weight % compared to the Ag-HNT fabricated with 5 g. (**Figure 4-4 and Figure 4-5**). Cu-HNT fabricated at 300 mg. also had a higher Cu weight % compared to Cu-HNT fabricated with 5 grams (**Figure 4-6 and Figure 4-7**). Perhaps by increasing the amount of time under electrolysis, a higher metal weight % on HNT surfaces may be achieved.

Metal particles and clusters were clearly detected under TEM and further validated that the electrochemical synthesis is an effective route towards creating metal-HNT composites (**Figure 4-10, Figure 4-13, Figure 4-14, Figure 4-17, and Figure 4-18**). The Ag particles appeared mostly spherical and the Cu particles appeared to form clusters with irregular geometries (**Figure 4-13, Figure 4-14, Figure 4-17, and Figure 4-18**).

It is suggested that the amount of voltage applied affected the metallic particle sizes. Additional studies showed that lower voltages produced smaller particle sizes under TEM (**Figure A-4 and Figure A-5**). It appeared that as the voltage levels increased the nanoparticles deposition and size of particles increased. Voltage variation during electrolysis altered the coloration of the final Cu-HNT powders and appeared that particle size influenced color. Electrolysis of Cu at 60 V with HNTs produced Cu-HNT with blue coloration (**Figure A-1: B**). Electrolysis of Cu at 120 V produced Cu-HNT with a green

coloration (**Figure A-1: C**), and electrolysis at 240 V produced Cu-HNT with brown coloration (**Figure A-1: D**). The electrolysis syntheses were repeated five times and the color changes were replicable. XRD patterns and FTIR spectrums of HNT, Ag-HNT, and Cu-HNT showed that the electrolysis approach did not damage the crystal structures or adsorption band patterns of HNTs (**Figure 4-19, Figure 4-20, Figure 4-21, Figure 4-22, Figure 4-23, and Figure 4-25**). This is important because HNTs are projected to be a common template in future nanotechnologies. The combination may offer more potential applications and devices that have not yet been discovered.

Overall, the materials characterization showed that the electrolysis process was successful at creating metal-HNT composites. The advantages of using electrolysis as an HNT surface modification technique include the simple setup, the ability to fabricate using minimal starting materials, and the scalability potential. It is theorized that larger custom electrodes, designed with more surface area could be used to synthesize industrial-scale amounts of metal-HNTs. The electrolysis method may not be not limited to Ag and Cu, as other metals such as gold, palladium, platinum are theorized to behave similarly with HNTs during electrochemical syntheses.

5.1.1 *Metal-HNTs as Antibacterial Agents*

Ag has been previously coupled with HNTs for antibacterial applications in paints (Abdullayev *et al.*, 2011). In the 2011 article, nanorods were synthesized in the inner lumen of HNTs and were added to composite paints. Previous research shows the outer surface has more surface area for the loading of drugs or polymers (Lin *et al.*, 2016; Veerabadrán *et al.*, 2009). In this research, the outer surface was used to deposit Ag and Cu nanoparticles. An advantage of using the outer surface for particle deposition is that

the nanoparticles are more readily available for interactions. The electrolysis method takes advantage of the outer HNT surfaces and allows for additional loading of antibacterial agents within the inner lumens. The additional antibacterial agents offer multi-modes of action against bacteria.

The metal-HNT types created in this research showed significant reduction of bacteria growth with predictable responses (**Figure 4-28, Figure 4-29, and Figure 4-42**). There were predictable responses across all HNT nanocomposites and the null hypothesis was rejected. As the concentration of metal-HNT was increased in broth cultures, the absorbance values were decreased. The Ag-HNT-N and Ag-HNT-N-S combinations demonstrated significant reductions in both *E. coli* and *S. aureus* (**Figure 4-32, Figure 4-33, Figure 4-36, and Figure 4-37**). Cu-HNT-N and Cu-HNT-N-S performed better than Cu-HNT against bacteria compared to Cu-HNT (**Figure 4-30, Figure 4-31, Figure 4-34, Figure 4-35, Figure 4-38, and Figure 4-39**).

5.2 Polymer Metal-HNT Nanocomposites

HNTs have shown to be ideal particles for polymer reinforcement (Abdlayev and Lvov, 2013; Guo *et al.*, 2009; Lvov *et al.*, 2008). The utilization of nanofiber mats and scaffolds has been widely investigated for a variety of surgical and tissue engineering applications. The current fabrication methods, for example, electrospinning, are difficult to translate into an operating room. Solution blow spinning may offer an easily adaptable alternative that has the potential to generate on demand conformal nanofiber mats directly on a wide range of targets.

The solution blow spun nanofibers loaded with metal-HNTs and loaded with nitrofurantoin were shown to be effective at reducing bacterial growth. The addition of

metal-HNTs and drugs demonstrated the feasibility and versatility of solution blown HNT-nanofibers as antibacterial nanostructured coatings. The present study demonstrates facile fabrication of nanofibers loaded with HNTs using only a commercial airbrush and compressed air. SEM and TEM image showed that HNTs could be encapsulated in PLGA nanofibers during solution blow spinning (**Figure 4-45** and **Figure 4-47**). The images show single and clusters of HNTs in the nanofibers. The prevention of HNT aggregates in nanofibers may be achieved by reducing the concentration of HNTs or by modifying the HNT surfaces.

Additional studies showed the cytocompatibility of PLGA-HNT nanofibers (**Figure C-1, Figure C-2, Figure C-3, Figure C-4, and Figure C-5**). In the cytocompatibility assays, all cell types behaved normally on PLGA and PLGA-HNT substrates. This method offers much potential as the nanofibers can be directly deposited on to any surface and geometry with a vast array of polymer materials. It is suggested that these types of composites may have potential applications in wound healing, 3D tissue engineering, infection prevention, and hemostatic devices.

5.2.1 *ABS and PDMS Loaded with Metal-HNTs*

ABS and PMDS substrates loaded with HNTs were not effective at reducing bacterial growth (**Figure 4-51, Figure 4-52, Figure 4-53, and Figure 4-54**). The plastic and rubber materials are not as easily degraded when compared to the PLGA polymer. Perhaps coating the ABS and PMDS through the LBL method may be a more effective route. Fabricating a degradable coating may allow for available metal-HNTs on the surfaces.

Antibacterial surface modifications may allow for more effective substrates.

Additional PDMS-HNT-PEO-N studies showed that the surface may be modified for antibacterial applications (**Figure 4-55**, **Figure 4-56**, **Table 4-1**, and **Table 4-2**). The PEO coatings may have additional biomedical applications, as additional studies showed a reduction of protein adsorption of the surfaces and enhanced wettability (**Figure B-3**, **Figure B-4**, and **Figure B-5**). The substrates displayed similar surface characteristics and showed for the first time that the hydrophilic properties could be maintained with the addition of HNTs in the PDMS networks after PEO modification. Previous studies and patents have explored hydrophilic PDMS surface modifications; however, no research has been conducted with the addition of HNTs. This data confirms that PDMS-HNT (10% wt./wt. HNT) maintains hydrophilic properties when treated with PEO and may have potential uses for medical device coatings.

CHAPTER 6

CONCLUSIONS AND FUTURE WORK

6.1 Conclusions

The high-throughput electrochemical fabrication approach further advances the field of inorganic hybrid nanoparticle synthesis, specifically HNT-metallization. The feasibility of electrolysis as a method for depositing metal nanoparticles on HNT surfaces was successfully demonstrated and proved to be a new route to modifying HNTs with antibacterial features. It was concluded that metallized HNTs could be used as an antibacterial agent for predictable responses with bacteria in fluid systems. Overall, the metal-HNTs created through electrolysis provide a foundation for future researchers to explore. The realization of scalable and cost effective antibacterial fabrication methods may provide civilization with a new arsenal of antibacterial additives.

6.2 Future Work

Future work will be focused on increasing the effectiveness of the metallized HNTs and polymer loaded substrates against bacteria. The electrolysis method will be guided toward testing with other metals and with combinations of metals. In the future, custom electrodes designed with greater surface area will be explored and the electrolysis of metal-compounds. Scaling fabrication for commercial feasibility will be explored. Examining the metallized HNTs with multi-drug combination formulations will continue

to be examined in an effort to further advance current antibacterial nanomaterials. With the emergence of resistant bacteria and the increase in health-care related infections, plastic and elastic polymer substrates should continue to be examined in an effort to create new nanostructured coatings for antibacterial applications.

The inorganic hybrid nanotubes are not limited to antibacterial applications. LBL strategies in combination with metal-HNTs may be used for chemical and biological sensors. Ag nanoparticles have optical applications, conductive applications, chemical applications, and thermal applications. Some of the potential uses of silver include optical limiters, solar cells, medical imaging, conductive adhesives, catalysts, and chemical vapor sensors. Potential uses of Cu nanoparticles include electromagnetic interference shielding, thermal conductive materials, catalysts, conductive inks, electronics, and nano-lubricants. These types of products will be explored in the future. Coupling metal nanoparticles with HNTs through electrolysis may allow for the creation of novel devices and advanced antibacterial additives.

APPENDIX A

EFFECT OF VOLTAGE ON CU-HNT PRODUCTION

A.1 Effect of Voltage on Cu-HNT Color and Morphology.

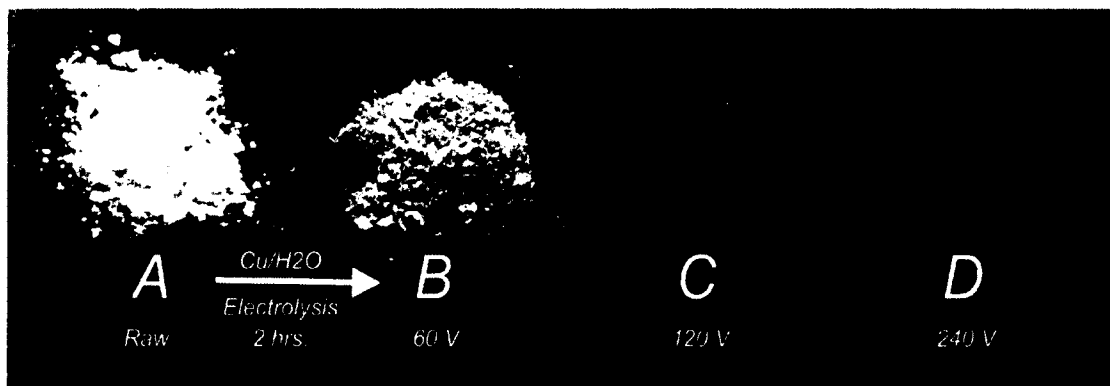


Figure A-1: Image of Cu-HNT Produced at Different Voltages. A) Control, B) 60 V, C) 120 V, and D) 240 V.

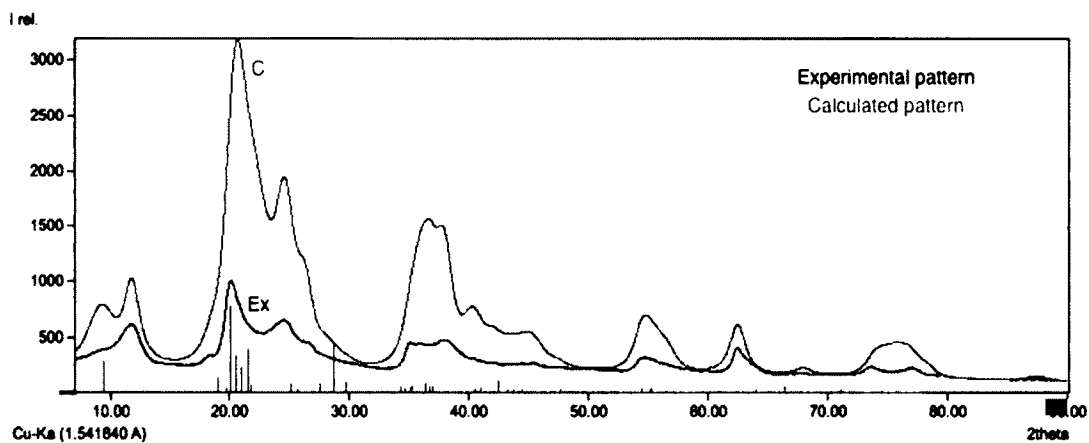


Figure A-2: XRD Pattern of Cu-HNT Produced at 60 V.

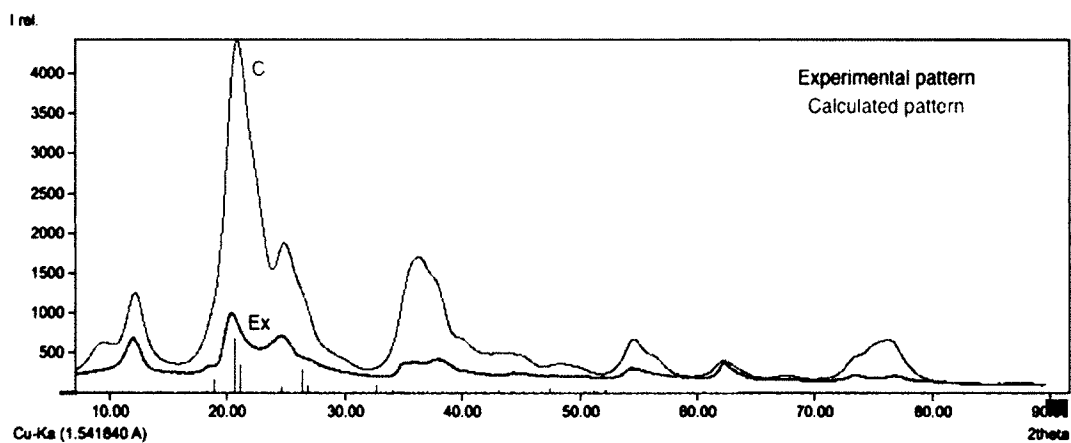


Figure A-3: XRD Pattern of Cu-HNT Produced at 120 V.

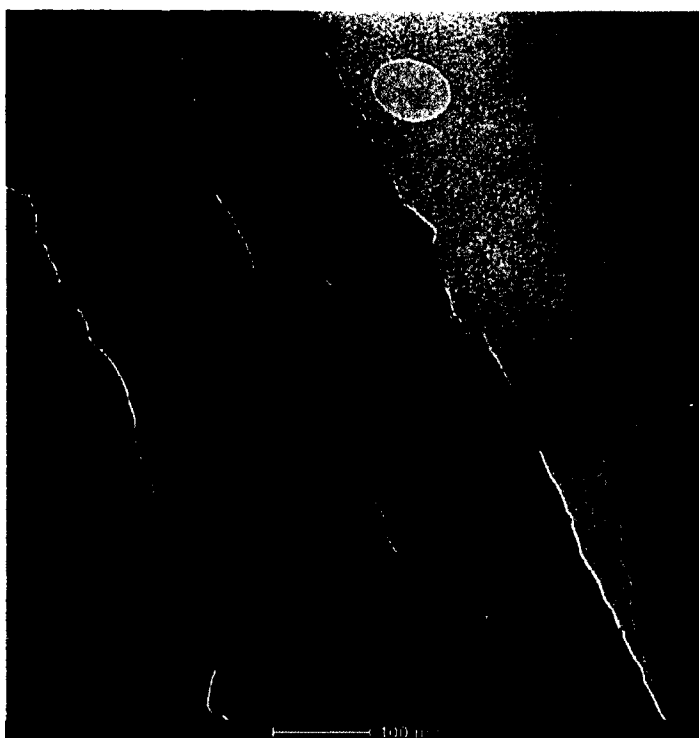


Figure A-4: TEM Image of Cu-HNT Produced at 60 V.



Figure A-5: TEM Image of Cu-HNT Produced at 120 V.

APPENDIX B

PDMS-HNT-PEO SURFACE ANALYSES

B.1 SEM and Protein Adsorption Assays

SEM was used to examine the nanocomposite surface topographies. PDMS-HNT composites treated with PEO (0%-5% wt./wt.) were adhered to a conductive adhesive tape and placed onto a stage for viewing. Gold sputter coatings (4 nm.) were applied to the surfaces with a Cressington 208 HR Metal Sputter Coater (Watford, England). The prepared stages were placed into the sample chamber and viewed with 1.0-2.0 kV. A Dynamic Contact Angle (OCA-15 plus) by DataPhysics (San Jose, CA) was used to study water contact angles.

A NanoDrop 2000c by Thermo Scientific (Waltham, MA) was used to monitor the protein adsorption properties of the modified PDMS-HNT composites with bovine-fibrinogen. All samples were pre-equilibrated for 24 hr. in phosphate buffered saline (PBS) (pH 7.4). A bovine fibrinogen solution was prepared in PBS (pH 7.4) (1 mg./ml.) and samples were placed in the protein solution for 4 hr. on a rocker. Samples were then thoroughly washed with PBS and sonicated in PBS (1% sodium dodecyl sulfate (SDS) solution for 30 minutes to desorb protein from surfaces. The product protocol for Micro-BCA assay kit was followed, added to protein solutions, and absorbance ($\lambda=562$ nm.) was monitored for each set of samples in triplicates.

SEM was used to study the modified PDMS composite surfaces morphology and nanostructure. It also provides a means for obtaining detailed topographical information about surface features. SEM micrographs showed changes in surface roughness with the addition of PEO into PDMS and PDMS-HNT (10% wt./wt. HNTs). To monitor the coating process, different PEO concentrations (0%-5% wt./wt.) were applied to the PDMS and PDMS-HNT discs. Surface roughness appeared to increase for both PDMS

and PDMS-HNT with the sequential addition of PEO concentrations (**Figure B-1** and **Figure B-2**). The PEO chains appeared to accumulate on the outermost surface (**Figure B-1: A and D**, and **Figure B-2: A and D**).

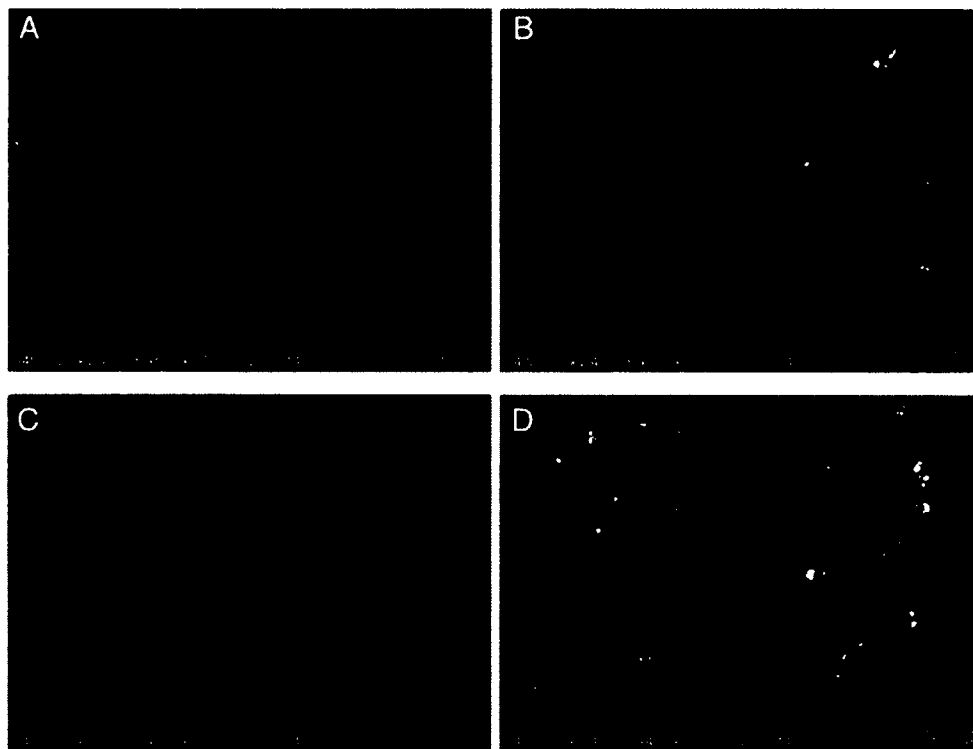


Figure B-1: SEM Images of PDMS Coated with Different Concentrations of PEO. A) PDMS, B) PDMS-PEO (1%), C) PDMS-PEO (2.5%), and D) PDMS-PEO (5%).

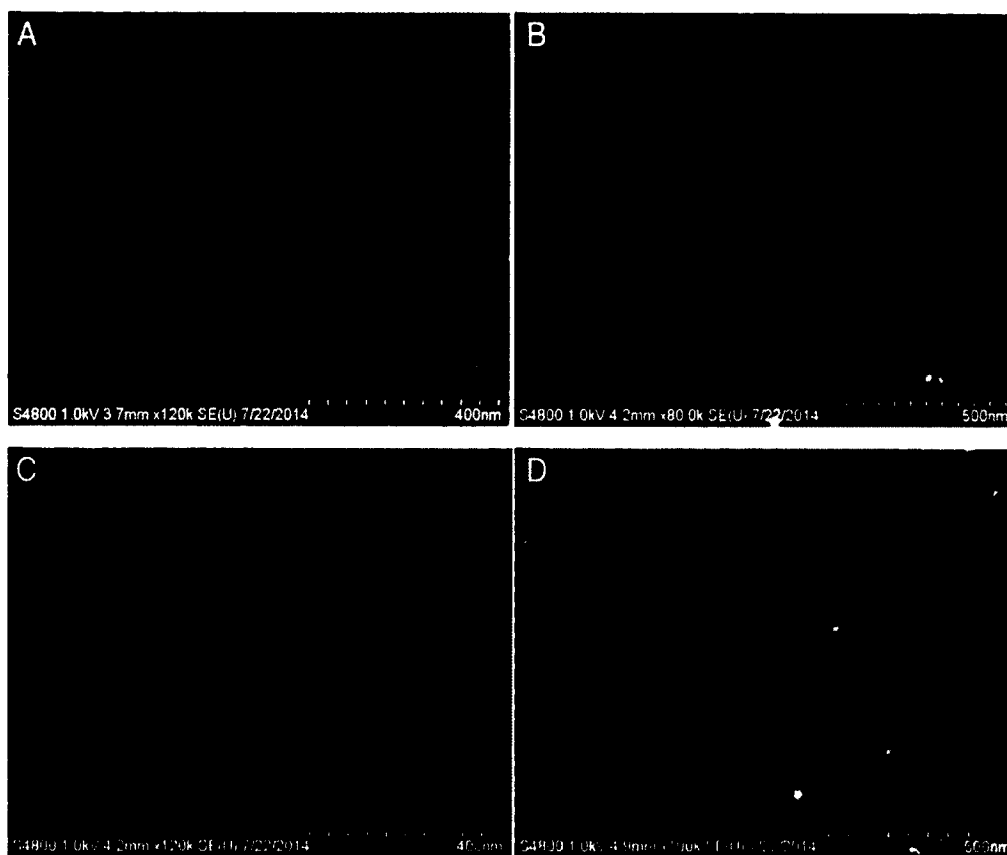


Figure B-2: SEM Images of PDMS-HNT-PEO Coated with Different Concentrations of PEO. A) PDMS-HNT, B) PDMS-HNT-PEO (1%), C) PDMS-HNT-PEO (2.5%), and D) PDMS-HNT-PEO (5%).

Similar surface characteristics were observed with the HNT loaded PDMS versions. Surface roughness appeared to increase as the PEO concentration increased. The PEO chains on the PDMS surface were easily hydrated and the rubber-water interface interactions were significantly altered. Water contact angle measurements showed the hydrophilic properties of the PEO coatings on both normal PDMS and PDMS-HNT loaded versions. Similar wettability was observed for both treated and untreated versions. Water contact angles above 100° were observed for the untreated PDMS and PDMS-HNT composites (**Figure B-3: A and B**, and **Figure B-4: A and B**). The PDMS and PDMS-HNT composites treated with PEO showed significant reduction

in water contact angle measurements, as contact angles for both versions reached under 10° angles (Figure B-3: C and D, and Figure B-4: C and D).

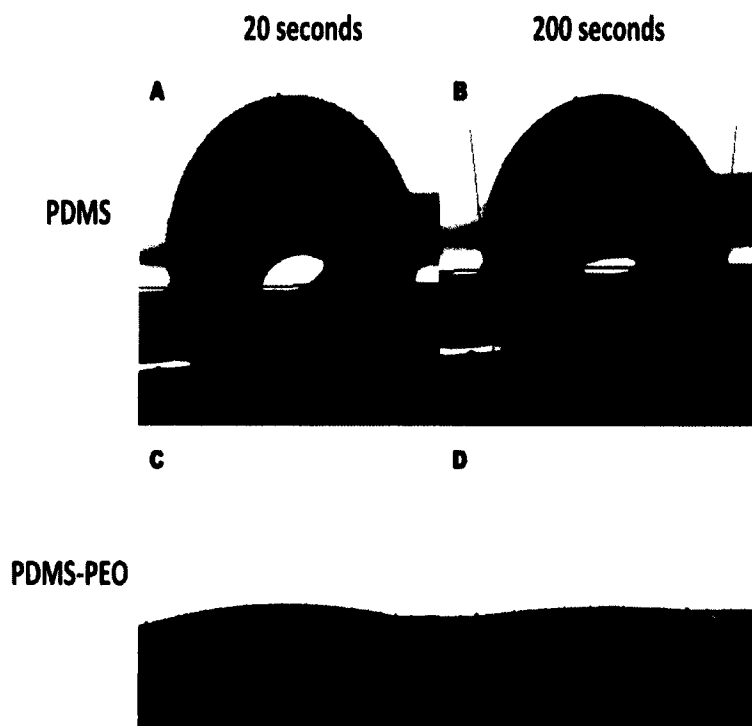


Figure B-3: Water Contact Angle Images of PDMS and PDMS-PEO. A) 103.3° , B) 97.7° , C) 8.2° , and D) 3.9° .

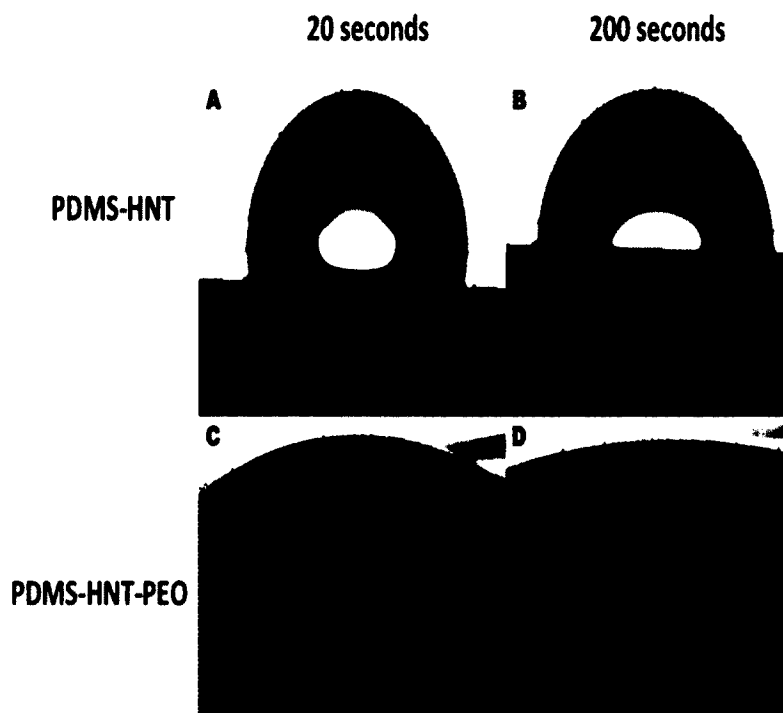


Figure B-4: Water Contact Angle Images of PDMS-HNT and PDMS-HNT-PEO. A) 103.8°, B) 90.8°, C) 15.8°, and D) 8.7°.

Hydrophilic properties were observed for the PDMS-HNT-PEO composites, and showed that wettability was maintained with the addition of HNTs. The PDMS-HNT-PEO composites were shown to reduce fibrinogen adsorption when compared to normal implant grade PDMS (**Figure B-5**). Micro BCA protein assays showed that total protein content was reduced on the composite surfaces when PEO concentrations increased on the composite surfaces. The result showed that PDMS-HNT-PEO composites were able to reduce surface protein content and offer additional biomedical applications.

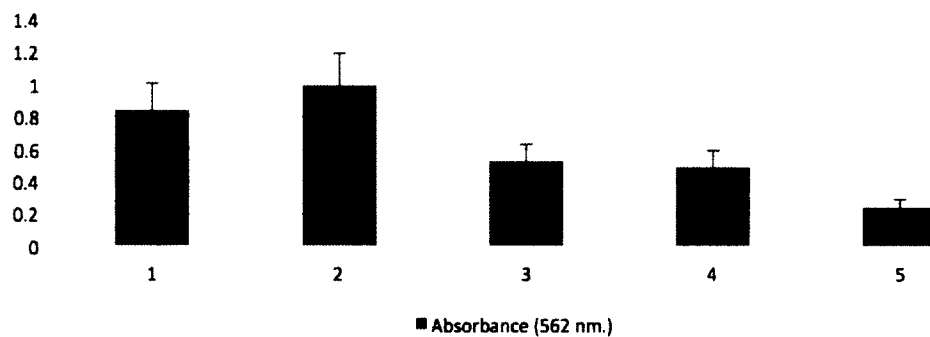


Figure B-5: Effect of PDMS-HNT-PEO on Absorbance of Fibrinogen (0-5% PEO).
Samples: 1) PDMS, 2) PDMS-HNT, 3) PDMS-HNT-PEO (1%), 4) PDMS-HNT-PEO (2.5%), 5) PDMS-HNT-PEO (5%).

APPENDIX C

CYTOCOMPATIBILITY OF HNT-NANOFIBERS

C.1 PLGA-HNT Cytocompatibility Assays

Poly(D,L-lactide-co-glycolide) (PLGA) (50:50, mol. wt. 30,000-60,000), halloysite nanoclay, acetone (HPLC grade), and Alcian blue were purchased from Sigma-Aldrich (St. Louis, MO). Picrosirius red stain and Von Kossa kit were purchased from PolySciences (Warrington, PA), and NucBlue® was purchased from Life Technologies (Carlsbad, CA). Mouse Embryonic Fibroblasts (MEF) NIH/ 3T3 ATCC CRL 1658, Mouse Preosteoblasts (MPO) subclones E1/3T3 ATCC CRL 2593, Hank's Balanced Salt Solution, Dulbecco's Minimal Essential Medium, α - Minimal Essential Medium was purchased from GIBCO, Life Technologies (Carlsbad, CA).

The previous nanofiber coating procedure was repeated and HNT mixtures were sprayed into 24-well culture plates in triplicates to form nanofiber coatings for histological investigation with two cell types. The nanofiber scaffolds were pre-treated before starting the cell studies by ultra-violet radiation for 40 minutes followed by a wash with sterile 1X Hank's Balanced Salt Solution (HBSS) to wash off the traces of chemicals. The cytocompatibility of the blow-spun PLGA-HNT nanofibers was tested on mouse embryonic fibroblasts (MEF) and the osteogenicity was tested on mouse preosteoblasts (MPO). The cells were cultured as per the standard cell culture protocols. Sterile conditions were maintained throughout the experiments and cell culture. The cell culture and growth medium for MEFs was Dulbecco's Minimal Essential Medium (DMEM) and for MPOs, α - Minimal Essential Medium (α - MEM).

For cytocompatibility and cellular adhesion, NucBlue® and Picrosirius red stains were used to monitor the MEF cells. The cells used were passage two cells pre-treated with NucBlue® and seeded on the blow-spun fibers (2.5×10^6 cells/ml). The cells were

incubated at 37 °C (days 1-8) and 5% CO₂ injected in the incubator. Picrosirius red was used to stain for collagen secretion, an indicator of extracellular matrix production. All cellular imaging was done under fluorescent and light microscope by Olympus (Tokyo, Japan).

For studying the osteogenicity of HNTs, MPO cells were seeded onto the fiber scaffolds and stained with Alcian blue to visualize the extracellular matrix production of glycosaccharides, mucosaccharides and glycoproteins over three days. Von Kossa staining assays were performed on the MPO laden scaffolds to visualize differentiation and the phosphate deposits from the mineral secretion of calcium phosphate (hydroxyapatite).

High cytocompatibility and proliferation levels were observed for both cell types on all scaffolds. High levels of cell attachment and growth were observed under Picrosirius red staining at days 3 and 7 and the arrows point to locations of interest such as cellular multi-layers and dense collagen production sites (**Figure C-1** and **Figure C-2**). Picrosirius red staining showed that dense collagen networks formed with both PLGA and PLGA-HNT nanofiber scaffolds. Cellular penetration was observed with the scaffolds and produced dense multilayered three-dimensional cellular networks and collagen secretion (**Figure C-2**). The collagen production and networks appeared to be more diverse in staining for the HNT loaded versions, which indicated multiple collagen types might have been produced (**Figure C-2**).

Both nanofiber scaffolds, pure PLGA and PLGA-HNT, were able to support the growth and proliferation of fibroblast cells over seven days. Von Kossa assays showed that preosteoblasts were able to proliferate, mature, and start mineralization production

on all blow-spun scaffolds by day 3 (**Figure C-3** and **Figure C-4**). Dense mineralization occurred along fiber networks. Darker silver staining was observed at the denser scaffold regions, which indicated cellular penetration and compatibility along the nanofiber networks. Additionally, Alcian blue staining demonstrated that both scaffold types could support preosteoblast attachment, maintain growth, and support extracellular matrix production at as early as 24 hr. (**Figure C-5**). Overall, the blow-spun PLGA and PLGA-HNT nanofibers were shown to support cell attachment and growth for both cell types, and demonstrated that multilayered cellular networks could be created.

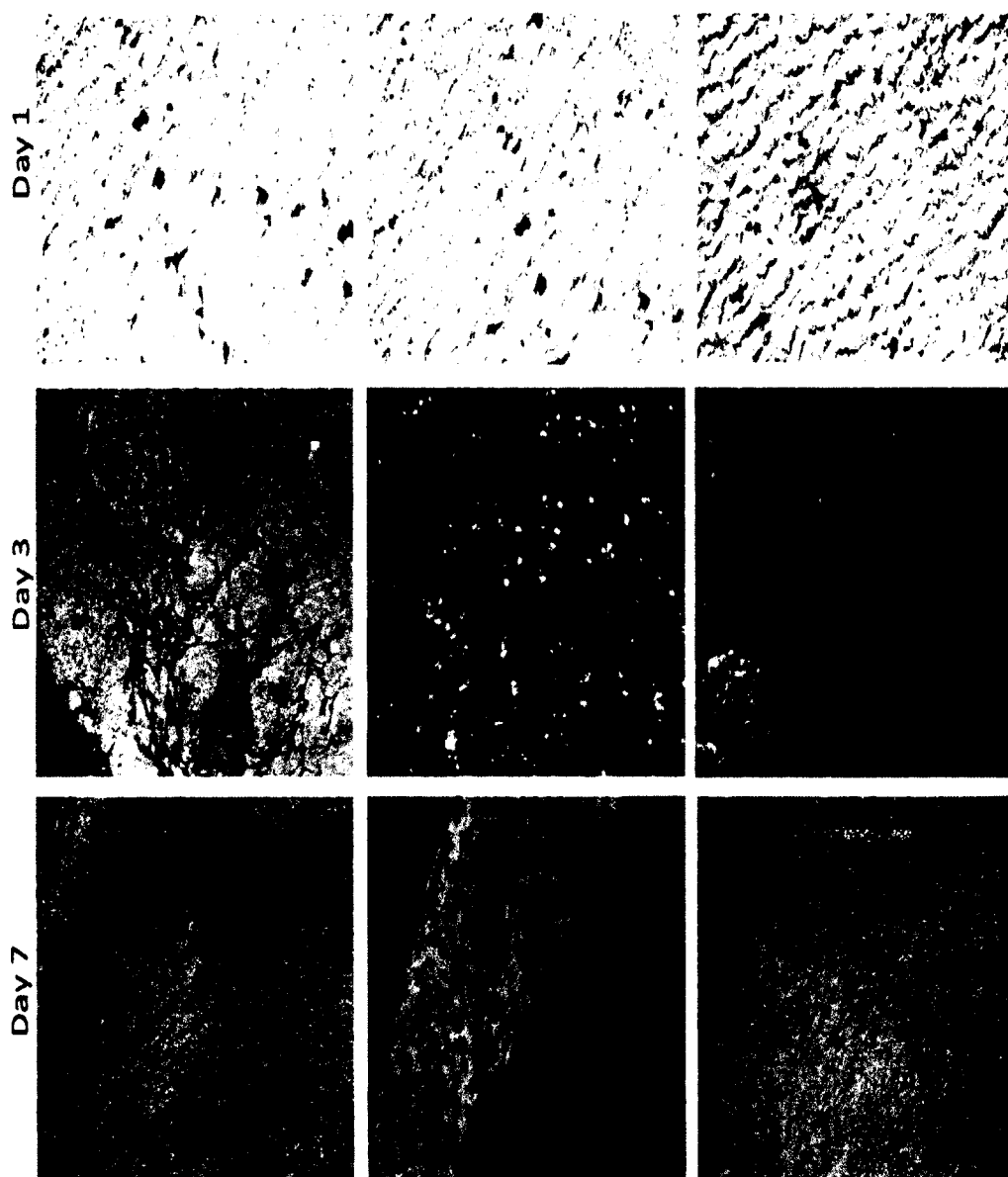


Figure C-1: Picrosirius Red Stain Assays with Mouse Embryonic Fibroblast Cells at Days 1-7 on PLGA Nanofibers.

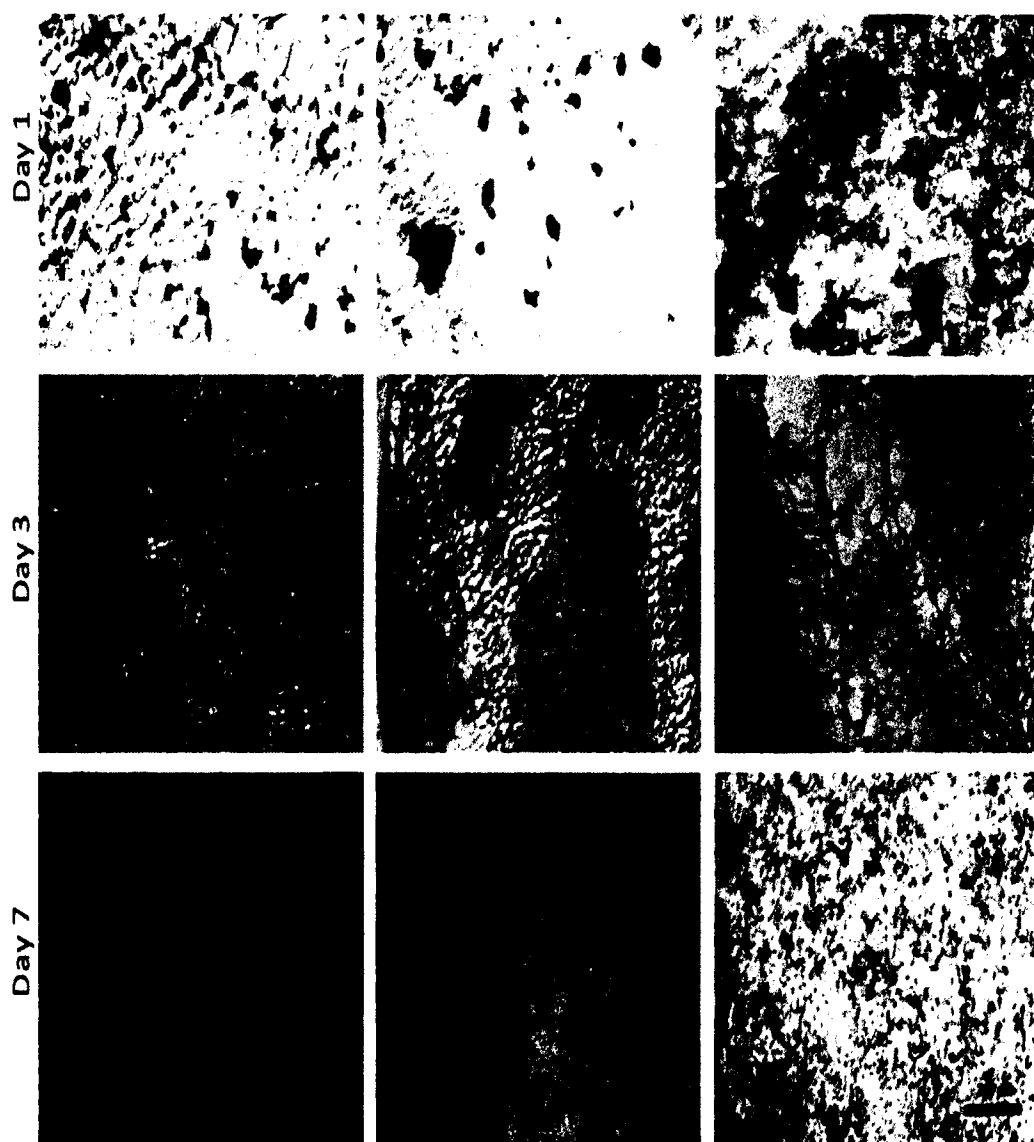


Figure C-2: Picrosirius Red Stain Assays with Mouse Embryonic Fibroblast Cells at Days 1-7 on PLGA-HNT Nanofibers.

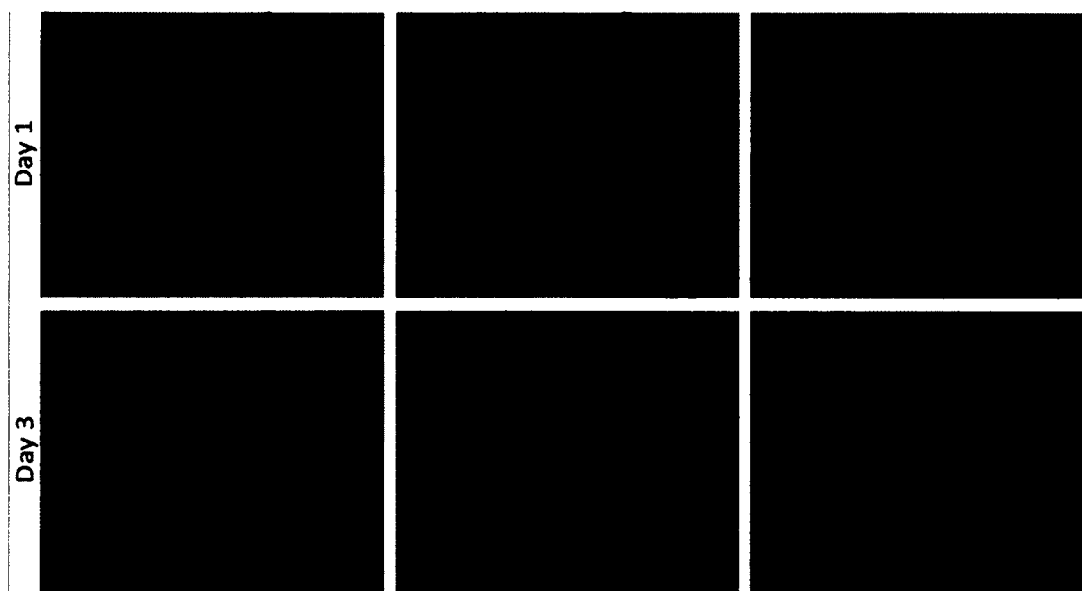


Figure C-3: Von Kossa Assays with Mouse Preosteoblast Cells at Days 1 and 3 on PLGA Nanofibers.

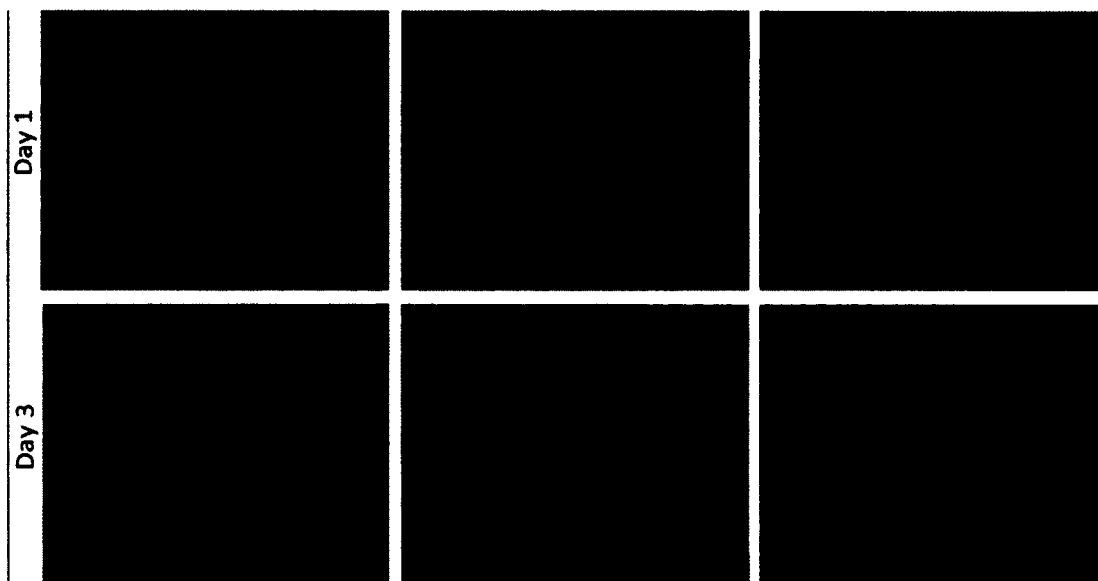


Figure C-4: Von Kossa Assays with Mouse Preosteoblast Cells at Days 1 and 3 on PLGA-HNT Nanofibers.

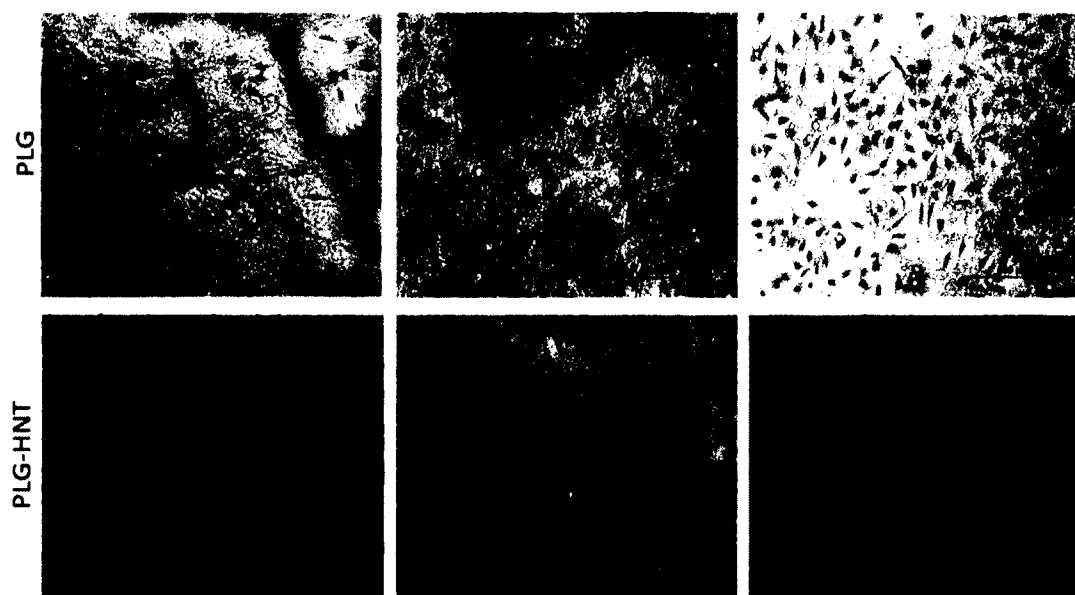


Figure C-5: Alcian Blue Stain Assays with Mouse Preosteoblast Cells at Day 1 on PLGA and PLGA-HNT Nanofibers.

BIBLIOGRAPHY

Abdullayev E, and Lvov Y. Functional polymer clay nanotube composites with sustained release of chemical agents. *Progress in Polymer Science*, 2013; 38:1690–1719.

Abdullayev E, and Lvov Y. Halloysite clay nanotubes as a ceramic “skeleton” for functional biopolymer composites with sustained drug release. *Journal of Materials Chemistry B*, 2013; 1:2894–2903.

Abdullayev E, Sakakibara K, Okamoto K, Wei W, Ariga K, and Lvov Y. Natural tubule clay template synthesis of silver nanorods for antibacterial composite coating. *American Chemical Society Applied Materials and Interfaces*, 2011; 3:4040–4046.

Alexander J. History of the medical use of silver. *Surgical Infections*, 2009; 10: 289–292.

Allanore A. Contribution of electricity to materials processing: Historical and current perspectives. *The Journal of the Minerals, Metals, and Materials Society*, 2012; 65:130–135.

Anselmann R. Nanoparticles and nanolayers in commercial applications. *Journal of Nanoparticle Research*, 2001; 3:329–336.

Ariga K, Lvov Y, Kawakami K, Ji Q, and Hill J. Layer-by-layer self-assembled shells for drug delivery. *Advanced Drug Delivery Reviews*, 2011; 63:762–771.

Behrens A, Casey B, Sikorski M, Wu K, Tutuak W, Sandler A, and Kofinas P. In situ deposition of PLGA nanofibers via solution blow spinning. *American Chemical Society Macro Letters*, 2014; 3:249–254.

Behzadi P, Behzadi E, Yazdanbod H, Aghapour R, Cheshmeh M, and Orman D. A survey on urinary tract infections associated with the three most common uropathogenic bacteria. *Journal of Clinical Medicine*, 2010; 5:111–115.

Bogle K, Dhole S, and Bhoraskar V. Silver nanoparticles: Synthesis and size control by electron radiation. *Nanotechnology*, 2006; 17:3204–3208.

Bonnemann H, and Richards R. Nanoscopic metal particles: synthetic methods and potential applications. *European Journal of Inorganic Chemistry*, 2001; 10:2455–2480.

Bremner I. Manifestations of copper excess. *The American Journal of Clinical Nutrition*, 1988; 67:1069–1073.

Bryers J. Medical biofilms. *Biotechnology and Bioengineering*, 2008; 100:1–18.

Chen S, Li J, Zhang Y, Zhang D, and Zhu J. Effect of preparation method on halloysite supported cobalt catalysts for Fischer-Tropsch synthesis. *Journal of Natural Gas Chemistry*, 2012; 21:426–430.

Danilcauk M, Lund A, Saldo J, Yamada H, Michalik J. Conduction electron spin resonance of small silver particles. *Spectrochimica Acta Part A*, 2009; 63:189–191.

Decher G. Fuzzy nanoassemblies: toward layered polymeric multicomposites. *Science*, 1997; 277:1232–1237.

Decher G, and Hong J. Buildup of ultrathin multilayer films by a self-assembly process. Consecutive adsorption of anionic and cationic bipolar amphiphiles on charged surfaces. *Macromolecular Symposia*, 1991; 46:321–327.

Dhruv H. Controlling Nonspecific adsorption of proteins at bio-interfaces for biosensor and biomedical applications. All Graduate Theses and Dissertations, 2009, Paper 276. <http://digitalcommons.usu.edu/etd/276>

Feng Q, Wu J, Chen G, Cui F, Kim T, and Kim J. A mechanistic study of the antibacterial effect of silver ions on *Escherichia coli* and *Staphylococcus aureus*. *Journal of Biomedical Materials Research*, 2008; 52:662–668.

Fernandez A, Paras L, Vidaltamayo R, Sampedro R, Martinez A, Signoret V, Estilla A, and Riojas P. Synthesis, characterization, and in vitro evaluation of cytotoxicity of biomaterials based on halloysite nanotubes. *Materials*, 2014; 7:7770–7780.

Franci G, Falanga A, Galdiero S, Palomba L, Rai M, Morelli G, and Galdiero M. Silver nanoparticles as potential antibacterial agents. *Molecules*, 2015; 20:8856–8874.

Gaetke L and Chow C. Copper toxicity, oxidative stress, and antioxidant nutrients. *Toxicology*, 2003; 189:147–163.

Gaynes R and Edwards J. Overview of nosocomial infections caused by gram-negative bacilli. *Clinical Infectious Diseases*, 2005; 41:848–854.

Gianluigi F, Falanga A, Galdiero S, Palomba L, Rai M, Morelli G, and Galdiero M. Silver Nanoparticles as Potential Antibacterial Agents. *Molecules*, 2015; 20: 8856–8874.

Guo B, Chen F, Lei Y, Liu X, Wan J, and Jia D. Styrene-butadiene rubber/halloysite nanotubes nanocomposites modified by sorbic acid. *Applied Surface Science*, 2009; 255:7329–7336.

- Hickok N and Shapiro I. Immobilized antibiotics to prevent orthopaedic implant infections. *Advanced Drug Delivery Reviews*, 2012; 64:1165–1176.
- Iller R. Multilayers of colloidal particles. *Journal of Colloid and Interface Science*, 1966; 21:569–594.
- Kesner S and Howe R. Design principles for rapid prototyping forces sensors using 3D printing. *Transactions on Mechatronics*, 2011; 99:1–5.
- Kim J, Kuk E, Yu K, Kim J, Park S, Lee H., Kim S, Park YK, Park YH, Hwang C, Kim Y, Lee Y, Jeong D, and Cho M. Antimicrobial effects of silver nanoparticles. *Nanomedicine: Nanotechnology, Biology, and Medicine*, 2007; 3:95–101.
- Kolakovic R, Genina N, Nyman J, and Vuorela P. Towards fabrication of 3D printed medical devices to prevent biofilm. *Science*, 1997; 277:1232–1237.
- Kramer A, Schwebke I, and Kampf G. How long do nosocomial pathogens persist on inanimate surfaces? A systematic review. *Infectious Diseases*, 2006; 6:130.
- Kumar K, Ray S, Nagaraja V, and Raichur A. Encapsulation and release of rifampicin using poly(vinyl pyrrolidone)-poly(methacrylic acid) polyelectrolyte capsules. *Materials Science and Engineering C*, 2009; 29:2508–2513.
- Lee I, Han S, and Kim K. Simultaneous preparation of SERS-active metal colloids and plates by laser ablation. *Journal of Raman Spectroscopy*, 2001; 32:947–952.
- Lemire J, Harrison J, and Turner R. Antimicrobial activity of metals: Mechanisms, molecular targets and applications. *Nature Reviews Microbiology*, 2013; 11:371–384.
- Liu P and Zhao M. Silver nanoparticle supported on halloysite nanotubes catalyzed reduction of 4-nitrophenol (4-NP). *Applied Surface Science*, 2009; 255:3989–3993.
- Long D, Wu G, and Chen S. Preparation of oligochitosan stabilized silver nanoparticles by gamma irradiation. *Radiation Physics and Chemistry*, 2007; 8:1126–1131.
- Lvov Y, Ichinose I, and Kunitake T. "Assembly of multicomponent protein films by means of electrostatic layer-by-layer adsorption. *Journal of the American Chemical Society*, 1995; 117:6117–6122.
- Lvov Y, Shchukin D, Möhwald H, and Price R. Halloysite clay nanotubes for controlled release of protective agents. *American Chemical Society Nano*, 2008; 2:814–820.
- Lvov Y, Wang W, Zhang L, and Fakhrullin R. Halloysite clay nanotubes for loading and sustained release of functional compounds. *Advanced Materials*, 2016; 28:1227–1250.

Mallick K, Witcomb M, and Scurrill M. Polymer stabilized silver nanoparticles: a photochemical synthesis route. *Journal of Materials Science*, 2004; 39:4459–4463.

Mamidwar S, Hodge S, Deshmukh V, and Vishal B. Hot-melt extrusion. *International Journal of Pharmaceutical Sciences Review and Research*, 2012; 15:105–112.

Mazzola L. Commercializing nanotechnology. *Nature Biotechnology*, 2003; 21:1137–1143.

Meddings J, Krein S, Fakhri M, Fakhri M, Olmsted R, and Saint S. Reducing unnecessary urinary catheter use and other strategies to prevent catheter-associated urinary tract infections: Brief update review. *Evidence Reports/Technology Assessments*, 2013; 9:211.

Mills D. Biocompatibility of halloysite clay nanotubes in a rat dermal model. *Journal of the Federation of American Societies for Experimental Biology*, 2014; 28:87.4.

Navaladian S, Viswanathan B, Viswanath R, and Varadarajan T. Thermal decomposition as route for silver nanoparticles. *Nanoscale Research Letters*, 2007; 2:44–48.

Niklas S, Salmela I, Fallarero A, Rosling A, Khajehheian M, Parsek M, and Singh P. Bacterial biofilms: an emerging link to disease pathogenesis. *Annual Review of Microbiology*, 2003; 57:677–701.

Parsek M and Singh P. Bacterial biofilms: an emerging link to disease pathogenesis. *Annual Review of Microbiology*, 2003; 57:677–701.

Piozzi A. Antimicrobial polymers with metal nanoparticles. *International Journal of Molecular Sciences*, 2015; 16:2099–2116.

Prabhu S and Poulouse E. Silver nanoparticles: Mechanism of antimicrobial action, synthesis, medical applications, and toxicity effects. *International Nano Letters*, 2012; 32:2–10.

Ramirez J, Winkler J, Spina C, and Collins J. Silver enhances antibiotic activity against gram-negative bacteria. *Science Translational Medicine*, 2013; 5:190ra81.

Rawtani D, and Agrawal Y. Halloysite as support matrices: A review. *Emerging Materials Research*, 2012; 1:212–220.

Rawtani D, Agrawal Y, and Prajapati P. Interaction of DNA with halloysite nanotube-silver nanoparticle-based composite. *BioNanoScience*, 2013; 3:73-78.

Reetz M and Helbig W. Size-selective synthesis of nanostructured transition metal clusters. *Journal of the American Chemical Society*, 1994; 116:7401–7402.

- Sandler N, Salmela I, Fallarero A, Rosling A, Khajeheian M, Kolakovic R, Genina N, Nyman J, and Vuorela P. Towards fabrication of 3D printed medical devices to prevent biofilm formation. *International Journal of Pharmaceuticals*, 2014; 459:62–64.
- Shin Y, Hohman M, Benner M, and Rutledge G. Electrospinning: a whipping fluid jet generates submicron polymer fibers. *Applied Physics Letters*, 2001; 78:1149–1151.
- Shleeva S, Tkac J, Christenson A, Ruzgas T, Yaropolov A, Whittaker J, and Gorton L. Direct electron transfer between copper-containing proteins and electrodes. *Biosensors and Bioelectronics*, 2005; 20:2517–2554.
- Stewart P and Costerton J. Antibiotic resistance of bacteria in biofilms. *Lancet*, 2001; 358:135–138.
- Stoodley P, Sauer K, Davies D, Costerton J. Biofilms as complex differentiated communities. *Annual Review of Microbiology*, 2002; 56:187–209.
- Tang X, Li L, Shen B, and Wang C. Halloysite-nanotubes supported FeNi alloy nanoparticles for catalytic decomposition of toxic phosphine gas into yellow phosphorous and hydrogen. *Chemosphere*, 2013; 91:1368–1373.
- Tutak W, Sarkar W, Lin-Gibson S, Farooque T, Jyotsnendu G, Wang D, Kohn J, Bolikal D, and Simon C. The support of bone marrow stromal cell differentiation by airbrushed nanofiber scaffolds. *Biomaterials*, 2013; 34:2389–2398.
- Vasiliev K, Cook J, Griesser H. Antibacterial surfaces for biomedical devices. *Expert Review of Medical Devices*, 2009; 6:553–567.
- Vasita R and Katti D. Nanofibers and their applications in tissue engineering. *International Journal of Nanomedicine*, 2006; 1:15–30.
- Veerabadran, G, Mongayt D, Torchilin V, Price R, and Lvov Y. Organized shells on clay nanotubes for controlled release of macromolecules. *Macromolecular Rapid Communications*, 2009; 30:99–103.
- Venkata K, Venkata R, Karthik P, and Singh S. Copper conductive inks: synthesis and utilization in flexible electronics. *Royal Society of Chemistry Advances*, 2015; 5:63985–64030.
- Vergaro V, Abdullayev E, Lvov Y, Zeitoun A, Cingolani R, Rinaldi R, and Leporatti S. Cytocompatibility and uptake of halloysite clay nanotubes. *Biomacromolecules*, 2010; 11:820–826.
- Vlamakis H, Chai Y, Beauregard P, Losick R, and Kolter R. Sticking together: building a biofilm the *Bacillus subtilis* way. *Nature Reviews Microbiology*, 2013; 11:157–168.

Weisman J, Nicholson J, Tappa K, Jammalamadaka U, Wilson C, and Mills D. Antibiotic and chemotherapeutic enhanced three-dimensional printer filaments and constructs for biomedical applications. *International Journal of Nanomedicine*, 2015; 10:357–370.

Windler L, Height M, and Nowack B. Comparative evaluation of antimicrobials for textile applications. *Environment International*, 2013; 53:62–73.

Xue J, Niu Y, Gong M, Shi R, Chen D, Zhang L, and Lvov Y. Electrospun microfiber membranes embedded with drug-loaded clay nanotubes for sustained antimicrobial protection. *American Chemical Society Nano*, 2015; 9:1600–1612.

Yapjakis C. Hippocrates of Kos, the father of clinical medicine, and Asclepiades of Bithynia, the father of molecular medicine: A review. *In Vivo*, 2009; 23:507–514.

Yin H, Yamamoto T, Wada Y, and Yanagida S. Large-scale and size controlled synthesis of silver nanoparticles under microwave irradiation. *Materials Chemistry and Physics*, 2004; 83:66–70.

Zhang Y, He X, Ouyang J, and Yang H. Palladium nanoparticles deposited on silanized halloysite nanotubes: synthesis, characterization and enhanced catalytic property. *Nature Scientific Reports*, 2013; 3:2948.

Zhao L, Chu P, Zhang Y, and Wu Z. Antibacterial coatings on titanium implants. *Journal of Biomedical Material Research B*, 2009; 91:470–480.

Zhou Y, Guo B, Liu M, Liao R, Bakr A, Rabie M, and Jia D. Poly(vinyl alcohol)/halloysite nanotubes bionanocomposite films: Properties and in vitro osteoblasts and fibroblasts response. *Journal of Biomedical Materials Research*, 2010; 93A:1574–1587.

Zhen C, Zhu M, Dai H, Liu Y, Mao J, Chen X, and He C. Halloysite nanotubes supported gold catalyst for cyclohexane oxidation with molecular oxygen. *Advances in Chemical Engineering and Science*, 2011; 1:15–19.

Zuo W, Zhu M, Yang W, Yu H, Chen Y, and Zhang Y. Experimental study on relationship between jet instability and formation of beaded fibers during electrospinning. *Polymer Engineering and Science*, 2005; 45:704–709.